THERMAL PERFORMANCE OF PRECAST CONCRETE CONNECTIONS EXPOSED TO FIRE

by

Jonathan Blackstone

A thesis submitted to the faculty of
The University of North Carolina at Charlotte
in partial fulfillment of the requirements
for the degree of Master of Science in
Civil Engineering

Charlotte

2019

Approved by:

____
Dr. Nicole Braxtan

____
Dr. Brett Tempest

____
Dr. Matthew Whelan

ABSTRACT

JONATHAN BLACKSTONE. Thermal performance of precast concrete connections exposed to fire. (Under the direction of DR. NICOLE BRAXTAN).

Today, most structural design for fire is governed by the International Building Code. Prescriptive code has proven to be efficient and simple to employ for structural design purposes. However, critical connecting elements in structures can be left unprotected. In addition, it is not safe to assume that the material properties of concrete are sufficient in providing prescribed fire ratings. Steel elements can be left exposed to the fire and increase in temperature quickly, experiencing significant reductions in strength that affect the overall connection.

This thesis details the experimental testing of a typical precast connection utilized in large precast parking garage structures vulnerable to elevated temperatures from accidental fires. Configurations of various precast corbel and wall designs are exposed to radiant heating and internal temperatures are measured over time. Numerical simulations are performed in the Abaqus finite element analysis software to provide a parametric study. Through the parametric study, normal weight and lightweight concrete specimens were investigated numerically with various design parameters.

The results showed maximum temperature reductions of 45 °C for the headed bars within the lightweight models compared to the normal weight models. By increasing the wall thickness from 8” to 10”, the interior reinforcement temperatures reduced by 153 °C. Increasing the wall thickness further to 12” provided a 43 °C reduction in maximum temperature. Finally, reducing the rear mesh embedment depth to 1” resulted in 133 °C higher temperatures for the normal weight specimens.

ACKNOWLEDGEMENTS

This research was funded through the Daniel P. Jenny Fellowship of the Precast Concrete Institute. Additional consultation, materials, and fabrication were provided by Tindall Cooperation and Metromont Cooperation. In addition, this research was facilitated by the University of North Carolina at Charlotte where the experimental tests were completed. The support provided by all parties involved is greatly appreciated and respected. The findings, conclusions, and opinions are those of the author and do not immediately reflect the view of any of the supporters.

TABLE OF CONTENTS

LIST OF TABLES

LIST OF FIGURES

CHAPTER 1: INTRODUCTION

1.1 Introduction

Precast concrete provides economic and efficient solutions to building construction while offering inherent protection against fire. Precast concrete members generally perform well under elevated temperatures; however, vulnerabilities may exist in unprotected steel connector elements that are used within primarily precast structures. The types of common precast concrete connections that are vulnerable in fires include plates, brackets, or other relatively thin steel components. Current prescriptive International Building Code (2018) requirements often do not require additional fire protection materials to be applied to these connectors in several situations, such as in precast parking garages that meet the height and area limitations of Type II-B construction.

This thesis focuses on the thermal performance of precast concrete connections exposed to fire. Connections are critical features of a structure as they are integral to the overall stability and level of safety of the structure. Structural fire design is typically provided through prescriptive design standards that requires components be built to a certain specification. In contrast, performance based design requires certain standards to be met, without providing the specifications.

Prescriptive fire protection has proven to be advantageous as it provides simplistic and extensive coverage of a large selection of structures under various conditions. Despite the benefits of prescriptive standards, there are some concerns inherent to the methodology of prescribing simplified fire protection across various structures. The first concern is that the specifications required by prescriptive codes are based on standardized fires. For example, ASTM International E119 provides a standardized temperature curve that does not accurately reflect a realistic fire scenario affected by environmental conditions. Site-specific environmental conditions can change the characteristics of the fire and may limit the effectiveness of the prescribed fire protection. Most fire resistance tests apply thermal loads adhering to the standardized temperature curve when assessing the performance of structural assemblies and therefore fail to account for realistic fire scenarios subject to environmental factors.

In addition to the limitations of standardized fire tests, there are protection gaps that can occur when following prescriptive codes. For example, it is possible to leave certain connecting elements of a structural system unprotected simply due to the determining factors that dictate construction classification and occupancy categories. There is further cause for concern when considering the material properties of most connecting elements, such as precast concrete and steel. Concrete possesses innate fire protection due to its low thermal conductivity and high specific heat and density. However, the connecting steel elements can be left unprotected because the supporting elements, typically precast concrete, do not require fire protection or already possess an inherent fire rating. For example, the Precast Concrete Institute (PCI) Design Handbook, 7th Edition recommends that connections weakened by fire match the rating of the supporting components. However, little guidance is given on which connections are considered susceptible. Even in the circumstances when fire protection is used for precast concrete or connecting steel elements, the protection will result in sufficient reduction of internal temperatures but leave crucial external surfaces subject to the full temperature of the fire.

Most fire protection is prescribed by the International Building Code (IBC), which also works in tandem with the International Fire Code (IFC). In addition, the PCI Design

Handbook and the PCI manual for the Design for Fire Resistance of Precast/Prestressed Concrete provide guidance on fire protection. The function of the IBC, IFC, and PCI provisions with respect to structural protection in fire is to prescribe a required fire rating (i.e., 1 hour, 1 hour and 30 minutes, 2 hours, etc.). Fire protection is provided through the fire resistance rating, which is based on the actual fire resistance of the building element. Fire resistance ratings ensure that building elements or assemblies prevent fire spread and continue to perform their structural function. The required fire resistance rating should be less than or equal to the provided fire resistance rating. In other words, the fire severity or demand should be less than the prescribed capacity.

Fire ratings are prescribed based on factors such as construction classification, occupancy categories, and building elements and materials. Fire ratings are also defined and prescribed based on standardized fire tests according to ASTM E119 and other comparable methods. Standardized fire tests such as ASTM E119 are guided by the following three principles: stability, integrity, and insulation. Stability demands that the structural element continues to perform its load-bearing function throughout the duration of the fire. The structural element must also maintain its integrity, meaning that it must not crack or begin to fail. Finally, testing for adequate insulation ensures that the side of the structural element not exposed to the fire does not exceed a specified temperature.

In the past, most standards have been largely prescriptive in nature. However, emerging standards today are trending towards performance based design. Additionally, it has been shown that it is necessary to develop a more fundamental understanding of fire effects on structural connections and to utilize the increasing capability of computers to make quantitative fire theory more efficient (Emmons, 2007). Therefore, this thesis will attempt to aid in the advancement, recognition, and implementation of performance based design of precast concrete connections for fire by evaluating the thermal performance of connections.

1.2 Goal

The work described in this thesis seeks to contribute to the understanding of the effect of fire on structures and the performance of structural materials. Despite the availability of prescriptive guidelines for fire protection in structures, including large precast concrete garages, specific guidance based on realistic performance of precast concrete and steel construction materials and typical connections are lacking. The goal of this thesis is to evaluate the thermal performance of precast concrete connections exposed to fire.

1.3 Scope of Work

The work described in this thesis includes three tasks: (1) experimental heat transfer testing of a typical precast concrete and steel connection; (2) replication of the specimen through finite element modeling and validation of the model through comparison to the experimental results; and (3) parametric study to evaluate the influence of parameters and design constraints.

A connection typical of current and practical connections utilized in large precast concrete structures, such as precast parking garages, offices, schools, and warehouses, was selected for the experimental fire testing. The specimens were designed with given variables within the connection to gain a more comprehensive understanding of the thermal performance of the connection. Radiant heating was used to experimentally simulate increased temperature from a fire event, allowing for a controlled application of heat with thermocouples and infrared sensors. A thermal finite element model was developed and validated against the experimental results. Extended finite element analyses were performed to complete a parametric study. The parametric study provided the ability to consider many parameters including but not limited to: component geometry and size, material composition, size and geometry of adjacent concrete elements, concrete topping applied over connection, fire intensity and duration, and number and location of connections.

1.4 Organization of Thesis

The following content of this thesis will be divided into six chapters. Chapter 2 will provide a background on behavior of structural materials under fire loads. Chapter 3 presents a literature review on specific parameters and topics within fire behavior of precast concrete components. For example, it is crucial to understand the variations experienced in the emissivity or thermal conductivity of concrete and steel in order to correctly model a given fire scenario. Chapter 4 details the setup, results, analysis, and discussion of the experimental tests completed. Chapter 5 discusses the validation process for the heat transfer model, provides a convergence study, and a concluding discussion. Chapter 6 details the parametric study completed to gain understanding of the connection performance considering various configurations and design parameters. Chapter 7 discusses the conclusions of the thermal performance of the connection and suggests directions for future studies.

CHAPTER 2: BACKGROUND

2.1 Introduction

This chapter will provide a basic background on topics within structural fire analysis that pertain to understanding the thermal performance of precast concrete connections exposed to fire. It is crucial to understand the mechanics of fire development, the interaction of fire and structural elements, and the effect of heat on mechanical properties of materials.

2.2 Fire Development

2.2.1 Fuel and Ventilation Factors

Figure 2.1 displays the time-temperature fire development curve for a typical compartment fire, assuming no fire suppression. In the incipient stage, ignition has not yet occurred because the potential fuel source is in the process of heating. Ignition marks the start of combustion and the beginning of the growth stage of the fire. This stage initially generates heat slowly as it is controlled by the fuel source but is proceeded by a rapid acceleration of heat generation. This rapid acceleration is marked by flashover, typically occurring around 600 °C, which is the transition into the burning stage of the fire and subsequently a fully developed fire. Considerations for structural design in fire typically start at flashover temperatures. During the burning stage the fire is no longer controlled by the fuel source but is now controlled by ventilation until the fuel is consumed and temperatures decrease. The decrease of temperature marks the decay stage. Most structural damage occurs during the burning stage of the fire where temperatures are greater than 600 °C (Buchanan, 2006).

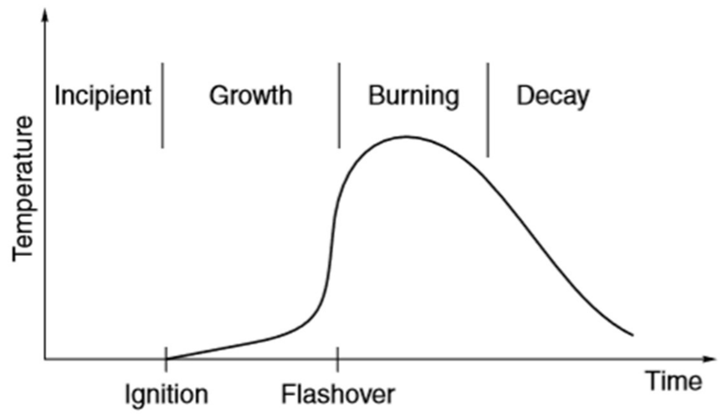

FIGURE 2.1: Time-temperature development curve (Buchanan, 2006)

Fuel load and ventilation are two critical factors in fire development. Potential fuel sources can include organic materials, chemicals, and combustible structural materials. The fuel of concern in precast concrete structures typically resides in the content of the building. Precast concrete is widely used in structural design, but is most commonly present in large parking garages. These garages may house hundreds of parked vehicles, each with a significant amount of gasoline. Parking garage fires become even more problematic with respect to ventilation. As depicted within Figure 2.1, the increase in temperature of a fire in the burning stage is controlled by the ventilation of the affected area. With respect to large parking garages, there is typically more ventilation within the affected area then compared to a compartment. The ventilation factor, or opening factor, can be calculated using Equation 2.1. This equation can be adapted to facilitate multiple window openings in a structure (refer to Figure 2.2 and Equation 2.2).

$$F_v = \frac{A_v\sqrt{H_v}}{A_t} \qquad Eqn. 2.1$$

$where$:

F_v = the ventilation factor (opening factor) $(m^{\frac{1}{2}})$

A_v = area of the window opening (m^2)

H_v = height of the window opening (m)

A_t = total internal area of bounding surfaces (including openings) (m^2)

$$H_v = (A_1H_1 + A_2H_2 + \cdots)/A_v \qquad Eqn. 2.2$$

$$A_v = A_1 + A_2 + \cdots = B_1H_1 + B_2H_2 + \cdots$$

$$A_t = 2(l_1l_2 + l_1H_r + l_2H_r)$$

$where$:

B_i = the breadth of the window (m)

H_i = the height of the window (m)

l_1 = the floor plan depth (m)

l_2 = the floor plan width (m)

H_r = the overall room height (m)

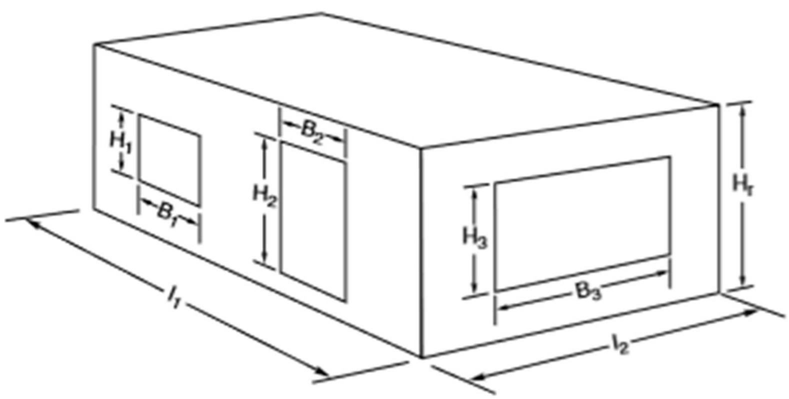

FIGURE 2.2: Structure with multiple openings (Buchanan, 2006).

Depending on the structural design of the parking garage, it is likely that the fuel load will play a large role in the progression of the fire as ventilation in these largely open structures is abundant. When considering the naturally open design of a large parking garage, there is potential for localized fires of individual vehicles, as well as travelling fires when adjacent vehicles sequentially ignite. The large amount of gasoline present as a fuel source for the fire leads to greater concern for fire development and structural damage within large precast garages.

2.2.2 Fire Temperature Histories

In addition to ventilation factors, fuel sources, material properties, and the location of structures, there are several other factors that provide numerous variations to fire design curves. In order to accommodate fire temperature histories for design purposes and produce typical temperature histories, the International Organization for Standardization (ISO) 834 and ASTM E119 provide two prevailing, standardized time-temperature curves. In addition, both ASTM E1529 and ISO sources provide standardized hydrocarbon time-temperature histories for pool and critical vehicle fires, respectively, shown in Figure 2.3. Standardized curves cover a small range of conditions, reduce innovation, and prevent engineering systems of fire analysis that result in lower engineered levels of safety. ASTM E119 and ISO 834 are similar in temperature amplitude throughout their development. ASTM E1529 is a simplified piecewise function that is plotted in Figure 2.3. Both curves start with a rapid increase in temperature in the first 20 minutes and are both followed with a nearly linear increase in temperature until the end of the fire. The fires are also assumed to have no decay stage, but instead continue to nearly linearly increase in temperature. The following equations detail the time-temperature relationships for the predominant standardized fire temperature curves.

<u>ISO 834</u>

$$\theta_g = 20 + 345\log(8t + 1) \qquad Eqn.\ 2.3$$

$where$:

θ_g = the gas temperature in the fire $(°C)$

t = duration of fire $(minutes)$

ASTM E119

$$T_g = 20 + 750\left(1 - e^{-3.79553\sqrt{t_h}}\right) + 170.41\sqrt{t_h} \qquad Eqn. 2.4$$

$where:$

T_g = the gas temperature of the fire $(°C)$

t_h = duration of fire $(hours)$

Eurocode Hydrocarbon

$$\theta_g = 20 + 1080(1 - 0.325e^{-0.167t} - 0.675e^{-2.5t}) \qquad Eqn. 2.5$$

$where:$

θ_g = the gas temperature of the fire $(°C)$

t = duration of fire $(minutes)$

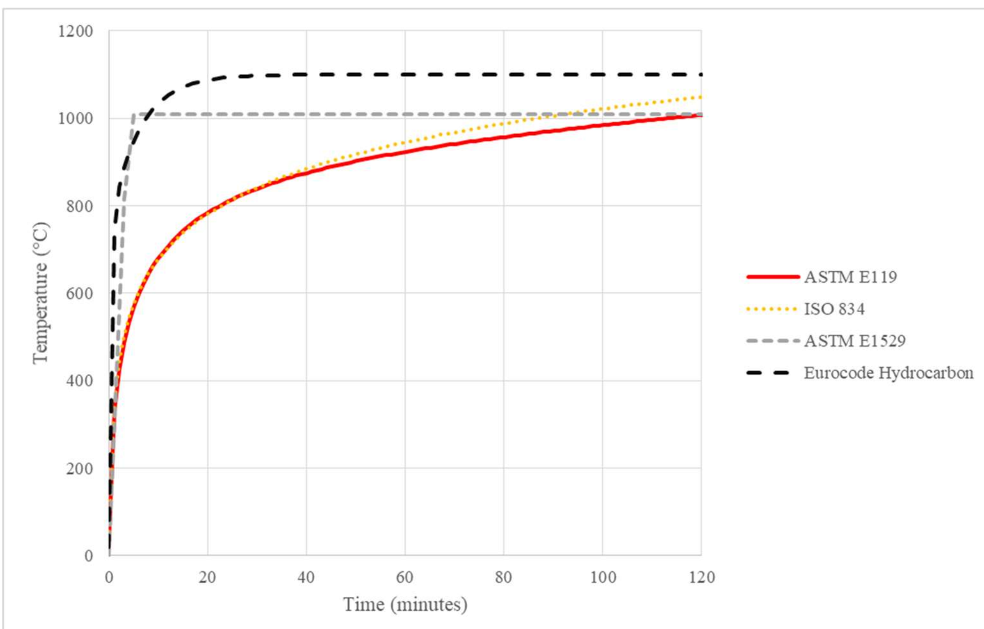

FIGURE 2.3: Standard time-temperature comparison of ISO 834, ASTM E119, ASTM E1529, and Eurocode Hydrocarbon.

2.3 Heat Transfer Mechanisms

It is essential to understand the basic heat transfer mechanisms that guide fire behavior - convection, radiation, and conduction. Heat transfers from the fire to the structural member by convection and radiation, then through the member by conduction.

2.3.1 Convection

Convection facilitates heat transfer by the movement of either gases or liquids between either solid or fluid interfaces (Buchanan, 2006). Convection is directly proportional to the temperature difference between the materials or interfaces. Convection provides the heat flux density (W/m^2) and can be predicted using Equation 2.6. The convective heat transfer coefficient, h_c, varies based on the geometry of the surface, nature of the flow, and thickness of the boundary interface. For simplification, Eurocode recommends 25 W/m^2-K for exposure to a standard fire and a coefficient of 50 W/m^2-K for exposure to a hydrocarbon fire.

$$q = h_c \Delta T \qquad Eqn. 2.6$$

$where$:

q	= heat flux density	$(\frac{W}{m^2})$
h_c	= the convective heat transfer coefficient	$(\frac{W}{m^2 K})$
ΔT	= the temperature between material interfaces	$(°C\ or\ K)$

2.3.2 Radiation

Radiation is defined as energy that is emitted by matter and then transported by electromagnetic waves. Radiation is extremely important in fires as it is the main mechanism for heat transfer from hot flames to fuel surfaces, from hot smoke to building objects, and from a burning building to an adjacent building (Buchanan, 2006). This process also produces a heat flux density (W/m^2) which can be calculated using Equation

2.7. Radiation is a function of emissivity, which represents the percentage of energy radiated from a black body or fire source. Black bodies absorb all of the radiant energy and have a corresponding value of 1.0. When considering structural fires, the resultant emissivity considers the fire as one surface and the structural material exposed as the other surface.

$$q = \varphi\varepsilon\sigma(T_e^4 - T_r^4) \qquad Eqn. 2.7$$

$where$:

q	= heat flux density	$(\frac{W}{m^2})$
φ	= the configuration factor	$(1.0\ in\ fire)$
σ	= the Stefan-Boltzmann constant	$(5.67 \times 10^{-8}\ \frac{W}{m^2K^4})$
ε	= the resulting emissivity defined by	$(\frac{1}{\frac{1}{\varepsilon_e}+\frac{1}{\varepsilon_r}-1})$
ε_e	= the emissivity of the emitting surface	
ε_r	= the emissivity of the receiving surface	
T_e	= the absolute temperature of the emitting surface	(K)
T_r	= the absolute temperature of the receiving surface	(K)

2.3.3 Conduction

Conduction occurs mostly in solid elements and facilitates heat transfer by the molecular vibration or movement of free electrons (Buchanan, 2006). It is dependent on multiple material properties including density, specific heat, and thermal conductivity. Density is the ratio of the mass to unit volume of a material. Specific heat is the amount of heat required to raise a unit mass of the material by a degree of temperature. In addition, the specific heat of materials can experience localized increases due to energy input during phase changes of materials at certain moisture percentages. These affects will be discussed in more detail in Chapter 3. Thermal conductivity is the amount of heat transferred through a unit thickness of a material by a unit of temperature difference. For normal weight (NW) concrete at ambient temperature, density ranges from 1900 to 2300 kg/m^3, specific heat is 900 J/kg-K, and thermal conductivity ranges from 0.8 to 1.4 W/m-K. For lightweight (LW) concrete at ambient temperature, density ranges from 1440 to 1840 kg/m^3, specific heat is 920 J/kg-K, and thermal conductivity is about 0.9 W/m-K. In comparison, steel has a density of approximately 7850 kg/m^3, a specific heat of 460 J/kg-K, and a thermal conductivity of 45.8 W/m-K. Steel is greatly affected by an increase of applied temperature as it has a lower specific heat and greater conductivity.

Steady state conduction represents the heat flow per unit of area, or heat flux density (W/m^2), and is represented by Fourier's Law as shown in Equation 2.8. In addition, transient conduction is shown in Equation 2.9.

$$q = -k\Delta T \qquad Eqn. 2.8$$

$where$:

q	= heat flux density	$(\frac{W}{m^2})$
k	= the thermal conductivity	$(\frac{W}{mK})$
ΔT	= temperature gradient along heat flow direction	$(\frac{°C\ or\ K}{m})$

$$q = \rho V c \frac{dT}{dt} \qquad Eqn. 2.9$$

$where$:

q	= heat flux density	$(\frac{W}{m^2})$
$\frac{dT}{dt}$	= change in temperature with respect to time	$(\frac{K}{sec})$
ρ	= the density of the solid	$(\frac{kg}{m^3})$
V	= the volume of the solid	(m^3)
c	= the specific heat of the solid	$(\frac{J}{kgK})$

2.4 Performance of Materials at Elevated Temperatures

2.4.1 Steel

The temperature rise in unprotected and protected steel members during fire can be approximated through several methods, which provide equivalent uniform temperature distributions throughout the steel cross section. The prediction model for unprotected steel (Equation 2.10) assumes that the steel member acts as a single lumped-mass. The prediction model for protected steel members (Equation 2.11) assumes that the external surface of fire protection is at the same temperature as the fire. Similar equations are available in other structural design specifications such as the American Institute of Steel Construction (AISC) 360-16 Specifications for the Design of Structural Steel Buildings. It is recommended to use a time interval of 5 seconds when calculating the temperature rise in steel members. Assuming that the fire temperatures follow the temperature history of ASTM E119, an approximate fire design analysis may be performed for unprotected and protected steel members using the prediction models. Prediction models defined by Equations 2.10 and 2.11 were obtained from the European Union Eurocode 3 1993-1-2 (2005).

$$\Delta\theta_{a,t} = k_{sh} \frac{A_m/V}{c_a \rho_a} \dot{h}_{net.d} \Delta t \qquad Eqn. 2.10$$

$where$:

k_{sh}	= the correction factor for the shadow effect	
A_m/V	= the section factor for unprotected members	$(\frac{1}{m})$
A_m	= the surface area of the member per unit length	$(\frac{m^2}{m})$
V	= the volume of the member per unit length	$(\frac{m^3}{m})$
c_a	= the specific heat of steel	$(\frac{J}{kgK})$

ρ_a = the unit mass of steel $\left(\frac{kg}{m^3}\right)$

$\dot{h}_{net.d}$ = the net heat flux per unit area $\left(\frac{W}{m^2}\right)$

Δt = the time interval (sec)

$$\Delta\theta_{a,t} = \frac{\lambda_p A_p/V}{d_p c_a \rho_a}\frac{(\theta_{g,t}-\theta_{a,t})}{(1+\frac{\varphi}{3})}\Delta t - (e^{\varphi/10}-1)\Delta\theta_{g,t} \qquad Eqn. 2.11$$

$$\varphi = \frac{c_p \rho_p}{c_a \rho_a} d_p A_p/V$$

$where$:

A_p/V = the section factor for insulated steel members

A_p = the area of fire protection per unit length $\left(\frac{m^2}{m}\right)$

V = the volume of the member per unit length $\left(\frac{m^3}{m}\right)$

c_a = temperature dependent specific heat of steel $\left(\frac{J}{kgK}\right)$

c_p = temperature dependent specific heat of protection $\left(\frac{J}{kgK}\right)$

d_p = the thickness of fire protection material (m)

Δt = the time interval (sec)

$\theta_{a,t}$ = the steel temperature at time t $(°C)$

$\theta_{g,t}$ = the ambient gas temperature at time t $(°C)$

$\Delta\theta_{g,t}$ = the change of ambient gas temperature during Δt $(°C\ or\ K)$

λ_p = the thermal conductivity of the fire protection $\left(\frac{W}{mK}\right)$

ρ_a = the mass density of steel $\left(\frac{kg}{m^3}\right)$

ρ_p = the unit mass of the fire protection material $\left(\frac{kg}{m^3}\right)$

2.4.2 Concrete

Stress-strain relationships of NW concrete with various aggregate types at elevated temperatures can be approximated through parametric models that incorporate reductions in compressive strength and thermal elongation, or thermal strain. Equations 2.12 through

2.16 replicate empirical models for determining the stress-strain relationships of concrete at elevated temperatures, provided by the European Union Eurocode 2 1992-1-2 (2004). Equations 2.12 and 2.13 are for siliceous aggregates and Equations 2.14 and 2.15 are for calcareous aggregates. Equation 2.16 is used to determine the temperature dependent stress as a function of the temperature dependent strain and compressive strength. When the thermal stress is evaluated beyond the elastic region, for numerical purposes a descending linear or non-linear plot should be adopted to complete the curve.

$$\varepsilon_c(\theta) = -1.8 \times 10^{-4} + 9 \times 10^{-6}\theta + 2.3 \times 10^{-11}\theta^3 \qquad Eqn.\,2.12$$
$$for\ \theta < 700\ °C$$
$$\varepsilon_c(\theta) = 14 \times 10^{-3} \qquad Eqn.\,2.13$$
$$for\ \theta > 700\ °C$$

$$\varepsilon_c(\theta) = -1.2 \times 10^{-4} + 6 \times 10^{-6}\theta + 1.4 \times 10^{-11}\theta^3 \qquad Eqn.\,2.14$$
$$for\ \theta > 805\ °C$$
$$\varepsilon_c(\theta) = 12 \times 10^{-3} \qquad Eqn.\,2.15$$
$$for\ \theta > 805\ °C$$

$$\sigma(\theta) = \frac{3\varepsilon_a f_{c,\theta}}{\varepsilon_{c1,\theta}(2+(\frac{\varepsilon_a}{\varepsilon_{c1,\theta}})^3}\ when\ \varepsilon_a \le \varepsilon_{c1,\theta} \qquad Eqn.\,2.16$$

$where$:

ε_a = the strain at ambient temperature $(\frac{m}{m})$

$f_{c,\theta}$ = the compressive strength at temperature θ $(\frac{N}{m^2})$

$\varepsilon_{c1,\theta}$ = the strain at temperature θ $(\frac{m}{m})$

2.5 Mechanical Properties of Materials at Elevated Temperatures

AISC and Eurocode suggest empirical reduction factors across a range of elevated temperatures that modify the elastic modulus, yield strength, proportional limit, and ultimate strength for steel and the compressive strength, elastic modulus, and creep and shrinkage (deformation) for concrete. Subsets of these reduction factors are replicated in Tables 2.1 and 2.2.

TABLE 2.1: Reduction factors for steel (Eurocode 3, 2005).

Steel Temperature θ_a	Reduction factors at temperature θ_a relative to the value of f_y or E_a at 20°C		
	Reduction factor (relative to f_y) for effective yield strength $k_{y,\theta} = f_{y,\theta}/f_y$	Reduction factor (relative to f_y) for proportional limit $k_{p,\theta} = f_{p,\theta}/f_y$	Reduction factor (relative to E_a) for the slope of the linear elastic range $k_{E,\theta} = E_{a,\theta}/E_a$
20°C	1	1	1
100°C	1	1	1
200°C	1	0.807	0.9
300°C	1	0.613	0.8
400°C	1	0.42	0.7
500°C	0.78	0.36	0.6
600°C	0.47	0.18	0.31
700°C	0.23	0.075	0.13
800°C	0.11	0.05	0.09
900°C	0.06	0.0375	0.0675
1000°C	0.04	0.025	0.045
1100°C	0.02	0.0125	0.0225
1200°C	0	0	0
NOTE: For intermediate values of the steel temperature, linear interpolation may be used.			

TABLE 2.2: Reduction factors for concrete (Eurocode 2, 2004).

Concrete Temperature θ_c	$k_{c,\theta} = f_{c,\theta}/f_c$		$\varepsilon_{cu,\theta} \cdot 10^3$
	NC	LC	NC
20°C	1	1	2.5
100°C	1	1	4
200°C	0.95	1	5.5
300°C	0.85	1	7
400°C	0.75	0.88	10
500°C	0.6	0.76	15
600°C	0.45	0.64	25
700°C	0.3	0.52	25
800°C	0.15	0.4	25
900°C	0.08	0.28	25
1000°C	0.04	0.16	25
1100°C	0.01	0.04	25
1200°C	0	0	-

CHAPTER 3: LITERATURE REVIEW

3.1 Introduction

This chapter details relevant literature and discusses the most pertinent topics within the scope of this thesis. The first topic is the process and development of prescriptive design guidance for fire protection of structures. A more thorough understanding of the protection gaps that occur in structural fire protection will help elaborate the significance of the experimental work completed in this thesis. The first topic will also briefly conclude by summarizing the overall benefits and hindrances of performance based design. Additional topics include expected fire loads for concrete parking structures, the effect of elevated temperature on the thermal properties of steel and concrete, and the concerns of spalling and subsequent surface temperatures.

3.2 Analysis of Prescriptive Code

Since the IBC is the most used and referenced code regarding fire protection of structures and generic construction requirements, this discussion will begin by detailing how protection gaps can and do occur within the current standard. The structure of concern for this thesis is a generic multi-storied precast parking garage. In accordance with IBC (2018), either open or enclosed parking garages fall under the classification of either moderate-hazard storage, Group S-1, or low-hazard storage, Group S-2. The structure is then classified based on the allowable building height and ranges from Type I to Type V, each with available sub categories A or B. For example, a precast garage, under group S, which has an allowable building height of 55 feet would be classified as Type IIB. Alternatively, a parking garage, also under group S, with an allowable building height of 40 feet would be classified as Type VB. These classifications are important because certain construction classifications and types have the potential to fall under various exemptions within the code. Considering the examples given previously, there are specific exemptions regarding construction that eliminate the requirement for a fire-resistance rating.

Before detailing the specific exemptions, it is important to understand several provided definitions by the IBC (2018). The IBC defines a fire barrier as a "fire-resistance wall assembly of materials designed to restrict the spread of fire in which continuity is maintained". The purpose of a fire barrier is to place something between the primary structure and a potential source of heat that is more fire resistant than the structure itself. The following exemption is detailed within Chapter 5, General Building Heights and Areas. Specifically, in the case of Incidental Uses (Section 509) there can exist a required fire barrier or similar horizontal assembly, as detailed in other sections of the IBC. This means that concerning secondary needs, a fire barrier could be required to provide a form of fire protection to the primary use of the structure. However, considering Incidental Uses (Section 509.4.1), construction supporting 1-hour fire barriers or horizontal assemblies used for incidental use separations in buildings of Type IIB, IIIB, or VB construction is not required to be fire-resistance rated unless required by other sections of the code (IBC, 2018). In short, the construction supporting the fire barrier, or similar horizontal assembly, does not require fire protection.

This exemption is also detailed under Chapter 7, Fire and Smoke Protection Features. Specifically, under Supporting Construction (Section 707.5.1) it is stated that supporting construction for a fire barrier shall be protected to afford the required fire-resistance rating of the fire barrier supported (IBC, 2018). In this provision, the code is recognizing the need to not only provide a fire barrier, but to protect the surrounding structural components that support the fire barrier itself. However, under exemptions it states that supporting construction for 1-hour fire barriers required by Table 509 in buildings of Type IIB, IIB, and VB construction is not required to be fire-resistance rated unless required by other sections of the code (IBC, 2018). In general, parking garages that meet certain height limitations and warrant a 1-hour fire barrier, can lack fire protection and even fire-resistance ratings for structural components and supporting construction. It is evident that there are cases where fire protection and fire-resistance ratings are not required. Furthermore, further recommendations, guidance, or direction to other sources are not provided by the IBC alongside the exemptions.

There are other prescriptive based design codes that discuss and detail fire protection. In the PCI Design Handbook Section 9.3 is dedicated to fire resistance and covers a wide range of standard fire tests including but not limited to: flexural elements, walls and columns, and precast concrete column covers. In addition, there is a brief discussion regarding the methodology of standardized fire testing. Supporting the idea that standardized fire tests are constrained and limited in design, the handbook states that standard fire tests involve regulations concerning the size of the assemblies, the amount of externally applied load, the region of the assembly to be exposed to fire, and the end point criteria on which fire resistance is based (PCI Design Handbook, 2004). Furthermore, because of the limited size of test furnaces, the result derived from members tested in laboratory furnaces cannot accurately reflect the behavior in a real building (PCI Design Handbook, 2004). While it is claimed that standardized fire tests, specifically ASTM E119, are suitable for assessing fire ratings in structural applications, standardized fire tests require further development and correspondence with realistic fires. Finally, the PCI

Design Handbook also makes note that The International Conference of Building Officials document Fire Resistive Workbook states the following:

"Although [Uniform Building Code] (UBC) Standard 7-1 [ASTM E119] is frequently described as a large-scale test, it clearly is not a full-scale test. Most floor slabs and roof decks are continuous over supports. Beams, girders, and trusses are framed into columns and other structural members in a variety of ways. As a result, testing laboratories are faced with the difficult problem of providing both end support and restraint for test assemblies representative of actual field conditions."

When considering the protection of connections, which includes supporting construction as detailed through the IBC, the PCI Design Handbook (Section 9.3.8) states that many types of connections in precast concrete construction are not vulnerable to the effects of fire, and consequently, require no special treatment (PCI Design Handbook, 2004). The only guidance provided is that connections that can be weakened by fire and thereby jeopardize the load carrying capacity of the structure should be protected to the same degree as that required for the supported member (PCI Design Handbook, 2004). However, the identification of connections that should be protected and the guidance for suitable protection is not provided or referenced.

3.3 Performance Based Design

Performance based design is provided by the International Code Council Performance Code (ICCPC). ICCPC provides a framework to achieve defined objectives in terms of tolerable damage and design events. ICCPC differs from other prescriptive codes by allowing the user to achieve various solutions systematically as a whole rather than directing the user to a single solution to address safety concerns for a structure. The benefits of performance based codes, such as ICCPC, is that it focuses on the outcomes rather than the solutions required to achieve certain outcomes. The performance based design process follows a three phase process to define the boundaries of performance based design or analysis (phase 1), use analytical methods to develop a design and evaluation procedure (phase 2), and then document and report the final performance based design (phase 3). Figures 3.1, 3.2, and 3.3 show flowcharts describing the performance based design process by each phase.

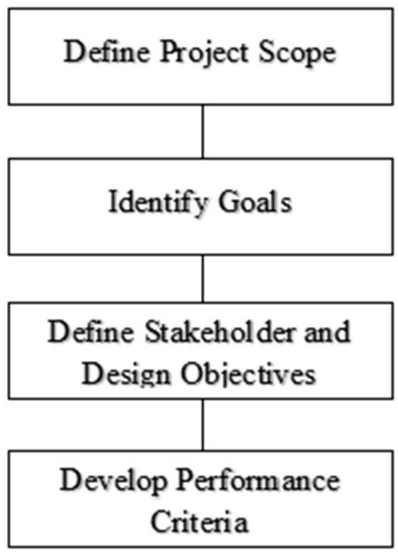

FIGURE 3.1: Performance based design phase 1 flowchart.

FIGURE 3.2: Performance based design phase 2 flowchart.

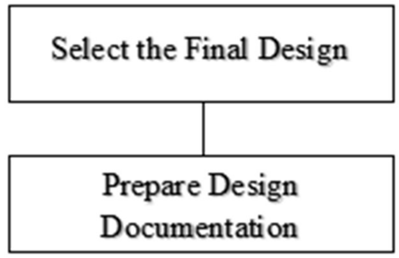

FIGURE 3.3: Performance based design phase 3 flowchart.

American Society of Civil Engineers (ASCE) Minimum Design Loads and Associated Criteria for Buildings and Other Structures (ASCE 7-16) provides provisions and commentary on the subject of structures in fire. Appendix E is dedicated to performance based design procedures for fire effects on structures and therefore does not provide standard fire resistance design by prescriptive methods. However, only general requirements are given for performance based structural design, such as identification of the performance objectives, quantification of the fuel load, identification and evaluation of structural design fires, determination of temperature histories for structural members and connections, and determination of the response of the structure. While the above requirements are critical steps in performance based design, it not a mandatory part of the overall standard and therefore not required. In addition, no further specific guidance is given pertaining to performance based design. Instead, buildings and other structures shall be designed to meet project-specific performance objectives required by the owner (ASCE, 2016). Comparable to the PCI Design Handbook, ASCE 7-16 only provides suggestions and initial guidance for performance based design procedures.

The AISC 360-16 specification provides criteria for the design and evaluation of structural steel components, systems, and frames for fire conditions in Appendix 4. The specifications provides guidance on how to effectively determine the heat input, thermal expansion, and degradation in mechanical properties of materials at elevated temperatures that cause progressive decreases in strength and stiffness of structural components at elevated temperatures (AISC, 2016). In addition, the appendix provides a performance based guideline that structural components, members, and building frame systems should be designed so as to maintain their load-bearing function during the design-basis fire (AISC, 2016). However, these performance based objectives are based on determining factors such as building occupancy, height of the building, the presence of active fire mitigation measures, and the effectiveness of fire-fighting. The appendix goes on to describe three existing limit states for elements serving as fire barriers. The three limit states are as follows: heat transmission leading to unacceptable rise of temperature on the unexposed surface, breach of barrier due to cracking or loss of integrity, and loss of load bearing capacity (AISC, 2016). These limit states closely resemble the guidelines followed by ASTM E119: stability, integrity, and insulation. On the surface, the objectives listed read as performance based design objectives, however they are more prescriptive in nature and are concluded in the appendix to be determined by the stakeholders in the building process, within the context of the general performance objective and limit states.

This review shows that relevant structural design codes recognize the benefits to performance based design over prescriptive design guidance but lack the realistic provision and implementation of performance based design for structures in fire. Since prescriptive codes can cover a broad range of conditions and are simple to use, their practical function has taken precedence. However, if steps can be made to exemplify how performance based design can promote innovation, be integrated into the overall design, provide engineered levels of safety, and increase safety throughout structures, performance based design will be favored over prescriptive design. The purpose of this thesis is to aid in the advancement, recognition, and implementation of performance based design for fire, with a specific emphasis on connections in precast concrete parking garages.

3.4 Expected Fire Loads for Concrete Parking Garages

Since the practice of design is moving towards performance based design, it is important to obtain more information regarding the methods of determining expected fire loads. Expected fire loads are used by structural code to provide fire resistance ratings. In addition, these ratings are based on occupancy, type of construction, and other factors. However, standardized tests are used to obtain the expected fire load for a structure. The methods for implementing fire protection and the methods for determining the expected loads used to determine the necessary protection should both be investigated further to provide realistic performance objectives.

Bayreuther and Pessiki (2006) performed an analytical investigation of fire loads for precast concrete garages where they investigated the influence of structural geometry and fire characteristics on the resulting fire loading. Research was completed on simplified parking garage models through the Fire Dynamics Simulator (FDS) on single vehicle fires. Figure 3.4 shows the FDS sample temperatures in the parking garage as compared to the temperature history of ASTM E119. The top opening temperatures represent the gas temperatures at the openings between the center walls of the modeled parking garage. Bayreuther and Pessiki also suggest that full implementation of performance based design for structures for fire requires more information about fire loading.

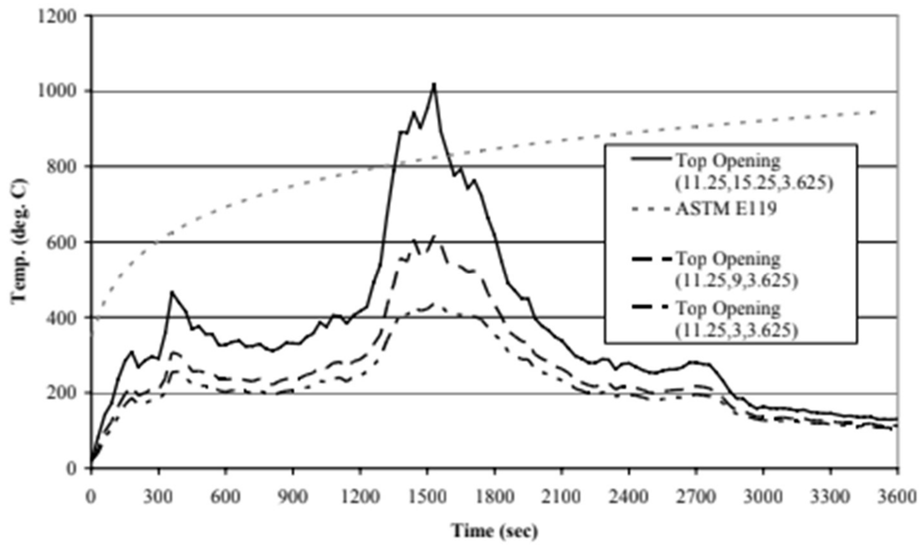

FIGURE 3.4: FDS and ASTM E119 time temperature curve comparison (Bayreuther and Pessiki (2006).

This figure shows that the ASTM E119 temperature history does not accurately predict the temperature history simulated by FDS for single vehicle fires. The peak temperature of E119 was surpassed in the simulation at about 25 minutes by one of the top opening temperature plots. Figure 3.1 also shows that at the time of the peak FDS results the temperatures exceed the temperatures of E119 by as much as 250 °C. However, the remaining top opening temperatures do not exceed the temperatures of E119.

Bayreuther and Pessiki (2006) concluded that the geometric effects such as openings between walls have a significant impact on the heat transfer through the structure. Simulation results indicated that either heat was trapped on one side of the garage or allowed to flow to another location based on the geometric effects. In addition, the research noted that fires on lower floors can generate a preheating effect on the upper floors if efficient heat transfer is developed between floors. This can result in increased temperatures of the concrete over the duration of the fire. Finally, Bayreuther and Pessiki

(2006) concluded that the standard time-temperature curve of ASTM E119 was not representative of either single or multiple vehicle fires within a concrete parking garage.

3.5 Thermal Properties of Materials

This section will be divided into subsections that each feature important physical and thermal properties for this thesis. As detailed in Section 2.3, there are several critical properties to take into consideration when performing any experiment or calculation including heat transfer. However, use of ambient material properties is only justified for simplified calculations and analyses. Since this thesis develops time-temperature histories and discusses temperature response over time, it is important to understand the effects of increasing temperature on material properties. These subsections will reference relevant design code and detail the methods used in Chapter 5, for validation of the numerical model developed in this thesis.

3.5.1 Density

Density is a function of the mass and volume of a material and it is important to consider the effect of elevated temperature on the density of a material. This is a necessary consideration since as the temperature of a material changes the volume changes accordingly. From the increase in volume, relative thermal expansion of the materials and thermal expansion of the restrained members leads to the development of significant thermally induced stresses. The effects of increasing temperature with respect to the density of concrete are provided by the European Union Eurocode 2 1992-1-2 (2004) under Section 3.3.2 and are detailed in the following equations. They represent the density as a function of time between different peak intervals and are based on free water loss. It is important to remember that the density of concrete at ambient temperature (20 °C) is between 1900 and

2300 kg/m^3. With respect to steel, Eurocode 3 1993-1-2 (2005) under Section 3.2.2 identifies that the unit mass of steel may be considered to be independent of the steel temperature and taken as 7850 kg/m^3. In addition, Buchanan (2006) also confirms that the density of steel, 7850 kg/m^3, remains constant with increasing temperature.

$$\rho(\theta) = \rho(20°C) \qquad Eqn. 3.1$$

$$for\ 20\,°C \leq \theta \leq 115\,°C$$

$$\rho(\theta) = \rho(20°C) \times (1 - 0.02\left(\frac{\theta-115}{85}\right))$$

$$for\ 115\,°C < \theta \leq 200\,°C$$

$$\rho(\theta) = \rho(20°C) \times (0.98 - 0.03\left(\frac{\theta-200}{200}\right))$$

$$for\ 200\,°C < \theta \leq 400\,°C$$

$$\rho(\theta) = \rho(20°C) \times (0.95 - 0.07\left(\frac{\theta-400}{800}\right))$$

$$for\ 400\,°C < \theta \leq 1200\,°C$$

$where$:

$\rho(\theta)$	= density of concrete	$(\frac{kg}{m^3})$
θ	= the temperature of the concrete	$(°C)$

3.5.2 Specific Heat

Similar to density, it is important to consider the effects of increasing temperature on specific heat. Specific heat is the amount of heat required to raise a unit mass of material by one degree of temperature. The specific heat of steel at ambient temperature is approximately half of the specific heat of concrete at ambient temperature, meaning that steel requires significantly less initial energy to increase in temperature and even less total energy required throughout the heating process. One complication when considering the effects of elevated temperature on the specific heat of materials is the estimation or assumption of moisture content. With respect to concrete, specific heat considerations assume the concrete to be 0% moisture by weight. Of course, this is not always the case with concrete as it requires a significant curing time to ensure adequate moisture levels. To reconcile excess moisture content in concrete, specific heat spikes can be inserted between certain temperature ranges. Figure 3.5 shows the temperature dependent values for specific heat including moisture content spikes. As provided by Eurocode 2 1992-1-2 (2004) and 3 1993-1-2 (2005).

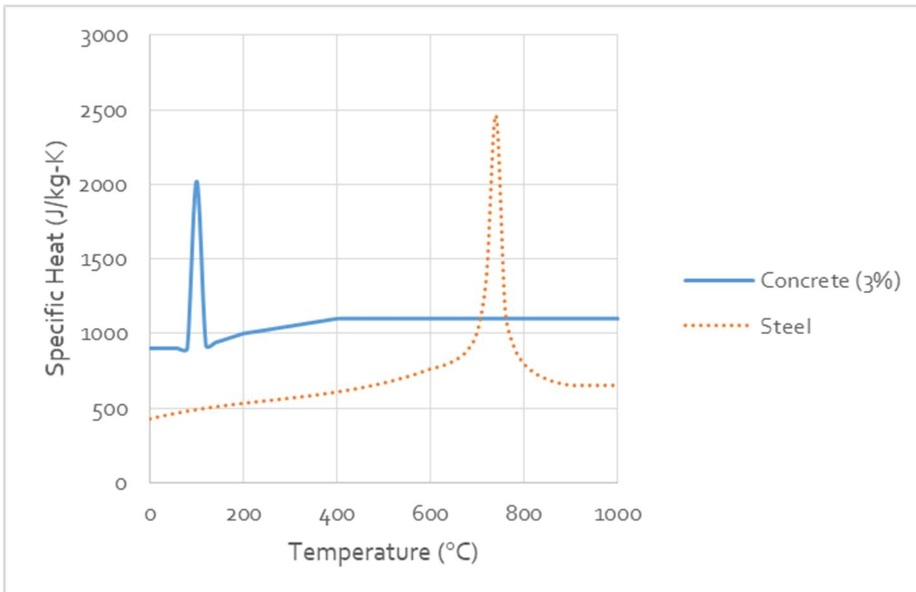

FIGURE 3.5: Temperature dependent specific heat of materials.

Steel undergoes a metallurgical phase change at approximately 735 °C. In order to accommodate the change in specific heat through the phase change, two additional temperature ranges and equations are inserted between 600 °C and 900 °C. As with density, Eurocode structural guidelines provide the functions of specific heat for concrete and steel with respect to time. In addition, Buchanan (2006) sites the same varying steel properties and adjustments. It should be noted that Eurocode 2 (2004) provides three adjusted values for specific heat spikes to accommodate moisture content: 900 J/kg-K (0%), 1470 J/kg-K (1.5%), and 2020 J/kg-K (3%). The specific heat may be modelled by these constant values situated between 100 °C and 115 °C with a linear decrease between 115 °C and 120 °C.

For simplified calculations the specific heat of concrete and steel are 880 and 460 J/kg-K, respectively. Refer to equations 3.2 and 3.3 for temperature dependent specific heat of concrete and steel, respectively.

$$c_p(\theta) = 900 \qquad Eqn. 3.2$$
$$for\ 20\ °C \leq \theta \leq 100\ °C$$
$$c_p(\theta) = 900 + (\theta - 100)$$
$$for\ 100\ °C < \theta \leq 200\ °C$$
$$c_p(\theta) = 1000 + \frac{(\theta - 200)}{2}$$
$$for\ 200\ °C < \theta \leq 400\ °C$$
$$c_p(\theta) = 1100$$
$$for\ 400\ °C < \theta \leq 1200\ °C$$

$where$:

$c_p(\theta)$ = the specific heat of concrete $(\frac{J}{kgK})$

θ = the temperature of the concrete $(°C)$

$$c_a = 425 + 0.773\theta_a - 0.00169\theta_a^2 + 2.22 \times 10^{-6}\theta_a^3 \qquad Eqn. 3.3$$
$$for\ 20\ °C \leq \theta \leq 600\ °C$$
$$c_a = 666 + \frac{13002}{738 - \theta_a}$$
$$for\ 600\ °C \leq \theta \leq 735\ °C$$
$$c_a = 545 + \frac{17280}{\theta_a - 731}$$
$$for\ 735\ °C \leq \theta \leq 900\ °C$$
$$c_a = 650$$
$$for\ 900\ °C \leq \theta \leq 1200\ °C$$

$where$:

$c_a(\theta)$ = the specific heat of steel $(\frac{J}{kgK})$

θ_a = the temperature of the steel $(°C)$

3.5.3 Thermal Conductivity

In addition to density and specific heat, thermal conductivity is another critical thermal property with respect to heat transfer analysis, specifically conduction. Therefore, it is necessary to similarly consider the effects of elevated temperature on the thermal conductivity of concrete and steel materials. For reference, thermal conductivity is the amount of heat transferred through a unit of thickness of material. For simplified calculations, the thermal conductivity of concrete is assumed between 0.8 and 1.4 W/m-K for concrete and 45.8 W/m-K for steel. Again, this shows that steel is significantly more efficient at conducting energy. However, it is necessary to consider the effects of elevated temperature. As the temperature increases, the process of transferring heat through a material requires more energy than at ambient temperature. This results in a reduction in the efficiency of conduction through a material. Structural codes Eurocode 2 (2004) and 3 (2005) provide the thermal conductivity of concrete and steel with varying temperature. With respect to concrete, instead of providing incremental temperature ranges as before, a global upper and lower limit are provided for high strength NW concrete. However, the thermal conductivity of steel simply reduces linearly with increasing temperature between two temperature intervals. For simplified calculations, the thermal conductivity of concrete and steel could be taken as 1.6 W/m-K and 45 W/m-K, respectively. Refer to Equations 3.4 and 3.5 for the thermal conductivity of concrete and steel with varying temperature. Equation 3.4 is for the upper and lower limit thermal conductivity of concrete, respectively.

$$\lambda_c = 2 - 0.2451\left(\frac{\theta}{100}\right) + 0.0107\left(\frac{\theta}{100}\right)^2 \qquad Eqn.\,3.4$$

$$\lambda_c = 1.36 - 0.136\left(\frac{\theta}{100}\right) + 0.0057\left(\frac{\theta}{100}\right)^2$$

$where$:

λ_c = the thermal conductivity of concrete $(\frac{W}{mK})$

θ = the temperature of the concrete $(°C)$

$$\lambda_a = 54 - 0.333\theta_a \qquad Eqn. 3.5$$

$$for\ 20\ °C \leq \theta \leq 800\ °C$$

$$\lambda_a = 27.3$$

$$for\ 800\ °C \leq \theta \leq 1200\ °C$$

$where$:

λ_a = the thermal conductivity of steel $(\frac{W}{m\ K})$

θ_a = the temperature of the steel $(°C)$

3.5.4 Convective Heat Transfer Coefficient

The need for more empirical data and experimentation on convective heat transfer coefficients is evidenced by the lack of explanation and methodology within the Eurocode fire provisions and other comparable structural documentation. Eurocode 1991-1-2 (2002), under section 3.2, recommends convective heat transfer coefficients of 25 and 50 W/m^2-K for standard external and hydrocarbon fires, respectively. Eurocode also recommends a convective heat transfer coefficient of 35 W/m^2-K under Eurocode 1 (2002) Section 3.3.1.1. In addition, Eurocode 1 (2002) Section 3.1 recommends a convective heat transfer coefficient of 9 W/m^2-K for the unexposed side of separating members if the effects of heat transfer by radiation are already accounted for and 4 W/m^2-K when radiation is not accounted for. Similar to Eurocode, AISC (2016) provides a recommendation of 25 W/m^2-K for standard exposure in Appendix 4.

According to a study done at the University of Maryland by Qunitiere and Veloo in 2011, convective heat transfer is usually insignificant in fire applications, as radiation dominates the burning rate for fires above 1 m in scale. Qunitiere and Veloo also state that in consideration of the effect of fire on structures (e.g. beams and columns), the convective heat transfer coefficient is usually taken as some extrapolation of normal heat transfer. In 2015, Zhang and Usmani studied the heat transfer principles in thermal calculation of structures in fire and noted that convection dominates [burning rates] at low temperatures, but above 400 °C radiation becomes increasingly dominant. Their report noted and considered the typical range of convective heat transfer coefficients, 5 – 50 W/m^2-K, similarly provided by Eurocode and AISC specifications. Both reports have valuable conclusions that pertain to this thesis.

First, through compartment fire tests utilizing a heated plate heat flux gauge and a water-cooled gauge, Qunitiere and Veloo (2011) found heat flux levels of 100 to 200 W/m^2-K with convection accounting for up to 25% of the total heat flux. That percentage correlates to a convective heat transfer coefficient of approximately 25 – 50 W/m^2-K, a similar range as provided by Eurocode and AISC specifications. However, Qunitiere and Veloo conclude that their results could be applied to improve empirical estimates of the rate of cooling in compartment fires, and its impact on structural integrity.

Zhang and Usmani (2015) concluded that the current models used in design codes to predict the temperature of steel members in a fire compartment ignore the heat sink effect from the mass, even though this effect is important as demonstrated by a modified one zone model which considers the heat sink effect. From this, Zhang and Usmani found that, for the conditions considered in their study, not considering the effect of heat sink within components yields a design of fire protection about 16% thicker than permissible when considering it. In general, when heat sink effects of single components through heat transfer are not considered the temperature of single components can be overestimated.

As observed from the previous studies, there is more research needed in the area of heat transfer in fire, specifically in the importance of convection and convective heat transfer coefficients. Again, due to the nature of convective heat transfer coefficients and considering that the coefficient changes over the course of a fire event, more empirical and situational data should be obtained in order to target an appropriate convective heat transfer coefficient for a given model.

3.5.5 Resultant Emissivity

As mentioned in the previous section, radiation dominates the magnitude of burning rates for most of a fire event. Therefore, radiation and subsequently emissivity should be considered in more depth. Emissivity is a measure of the efficiency of the emitting surface as a radiator (Buchanan, 2006). Most radiating surfaces or fire surfaces are "black-bodies" and typically have an emissivity of 1.0 or as low as 0.7. For example, an emissivity of 1.0 correlates to 100% efficiency in radiation of heat, where there are no losses to heat dissipation. It follows then that resultant emissivity represents the efficiency of radiation, net heat flux, between two surfaces. The Eurocode provides recommendations for emissivity values for both steel and concrete. Eurocode 1991-1-2 (2002), under Section 3.1, recommends an emissivity of 0.8 (80% efficiency) for a given structural member. However, Eurocode 1992-1-2 (2002) Section 2.2 recommends that the emissivity related to concrete surfaces be taken as 0.7. Similarly, Eurocode 1993-1-2 (2005) Section 2.2 recommends that emissivity related to steel surfaces be taken as 0.7 for carbon steel and 0.4 stainless steels. There are significant variations amongst the Eurocode, AISC, and Buchanan (2006) related to determination of the emissivity and resultant emissivity. As detailed previously, Eurocode provides constant emissivity values for steel and concrete.

While AISC provides basic guidelines for estimating the emissivity of the fire and view coefficient dependent on the type of assembly, as detailed in Table C-A-4.1 from AISC Appendix 4. Finally, Buchanan (2006) details the calculation of the resultant emissivity (Equation 3.6) between two surfaces and provides the above emissivity values above for “black-bodies”.

$$\varepsilon = \frac{1}{\frac{1}{\varepsilon_e}+\frac{1}{\varepsilon_r}-1} \qquad Eqn. 3.6$$

$where$:

ε	= the resultant emissivity between two surfaces
ε_e	= the emissivity of the emitting surface
ε_r	= the emissivity of the receiving surface

As with convective heat transfer coefficients, for most structural fire design applications, simplified properties and heat transfer mechanics are not adequate in providing accurate results replicating realistic fire scenarios. According to Buchanan (2006), emissivity can change during a fire; for example, zinc-coated steel (galvanized steel) has a very low emissivity until the temperature reaches about 400°C when the zinc melts and the bare steel is exposed to fire. As with the properties discussed above, constant emissivity values are not adequate and the effects of elevated temperature on emissivity should be considered.

In order to determine the relationship between the emissivity of steel and fire temperature, Sadiq et al. (2013) completed experimental furnace tests utilizing steel rods. They found that there are two temperature ranges where the emissivity of steel remains nearly constant, between 50 and 400°C and 500 to 600°C. Between 400 and 500°C there is a rapid increase in emissivity as the specimen surface starts to oxidize and changes surface roughness, causing a change of the total emissivity from approximately 0.28 at

50°C to approximately 0.7 at 600°C (Sadiq et al., 2013). These observations show that steel initially possesses a relatively low emissivity, or efficiency of radiation, but increases to about 70% efficiency as a fire approaches and experiences temperatures comparable to flashover. Therefore, the values provided for concrete and steel by Eurocode are reasonably conservative as they do not account for the initial low levels in efficiency of radiation during a fire event.

3.6 Explosive Spalling and Exposure to Severe Fire

Increased temperatures of concrete not only reduce the physical strength of concrete but also cause explosive spalling. The understanding of how moisture content and elevated temperatures affect concrete and therefore spalling are still under development. Ali et al. (2007) completed an experimental investigation on the explosive spalling and fracture-induced deformation of full-scale simply supported reinforced concrete slabs subjected to conventional fires and severe hydrocarbon fires. The research reported that all samples exhibited explosive spalling of different extents of severity regardless of moisture content. The samples tested had moisture content ranges of as low as 3.5% to 6%. The research found that slabs exposed to severe hydrocarbon fires experienced explosive spalling after two minutes of testing. Although the slabs subjected to the hydrocarbon curve exhibited the greater amount of spalling, the actual depth of the spalling was quite similar for all slabs, measuring between 15mm and 25mm, regardless of the fire severity (Ali et al., 2007). Finally, the study also found that the moisture front within the concrete slabs appears to move away from the heated surface during fire exposure and the rate it moves is increased by fire severity (Ali et al., 2007).

CHAPTER 4: EXPERIMENTAL TESTS

4.1 Introduction

This chapter will cover the conceptualization and actualization of the experimental tests completed for this research. Tests were developed that utilized a practical and common connection typically seen in large, multi-leveled structures. This connection was then replicated into numerous specimens each featuring one or multiple varying design parameters. A testing apparatus, instrumentation plan, and data collection method was developed to consistently test each specimen. After discussing the experimental setup and considerations of the work done, this chapter will detail the results from each test obtained from the recorded data and captured images. This chapter will conclude with an analysis of the results and a discussion of the experimental conclusions, including potential sources of error.

4.2 Connection Selection and Design

Before detailing the connection selected for the experimental tests, it is important to understand the background and thought process behind the selection. On March 16th, 2017 one of the largest fires in Raleigh, NC in nearly a century destroyed a timber framed apartment building under construction. The temperatures were so severe that a construction crane remaining over the site buckled and collapsed due to the rising heat. Thankfully, no one was critically injured or killed as a result of this event. This fire event uniquely pertains to this research project and specifically to the experimental setup and tests completed because connected to the apartment building was a precast concrete parking garage. This one fire event did not begin the inquiry suggested in this project, rather this is one of many examples of how fires affect structures, regardless of whether the fire is internal to the structure or external. The concrete parking deck was set to be demolished and replaced to ensure structural integrity given that there was significant visible damage in the form of spalling and cracks. However, the damage from the fire was not significant enough to cause complete collapse of the structure. In other words, the structural systems in place would have generally maintained their stability, integrity, and insulation. It is important to note that the garage and apartment building were still under construction when the fire occurred. This explains why the apartment building became a singular inferno as there were little to no active or passive fire protective systems in place since the sprinkler system was not installed yet. Refer to Figure 4.1 through Figure 4.4 for the photographs of the building, fire event, and demolition.

FIGURE 4.1: Pre fire apartment building Raleigh, NC (Wtvd, 2017).

FIGURE 4.2: Fire event, March 6th, 2017 Raleigh, NC (Wtvd, 2017).

FIGURE 4.3: Post fire, remaining stairwells and parking deck (Wtvd, 2017).

FIGURE 4.4: Demolition of adjacent parking deck (Wtvd, 2017).

Even though the structural damage was not significant enough to cause collapse, it should be noted that the parking garage was unloaded at the time of the fire and experiencing only normal dead loads and construction live loads. Additionally, even though the fire was external to the parking deck the resulting internal temperatures of structural components throughout the deck should be considered. Those internal temperatures are critical to the overall strength and stability of the structure when considering the parking deck as fully loaded with the prescribed live load active throughout the structure. As discussed in Chapter 2, the resulting internal temperatures of structural components could lead to drastic reductions in the yield strength of steel and concrete. This raises some critical concerns when considering fully loaded parking garages experiencing adjacent building fires. Figures 4.5 and 4.6 show corbels exhibiting some of the concerns detailed in Chapter 1 regarding connecting steel elements being exposed and unprotected.

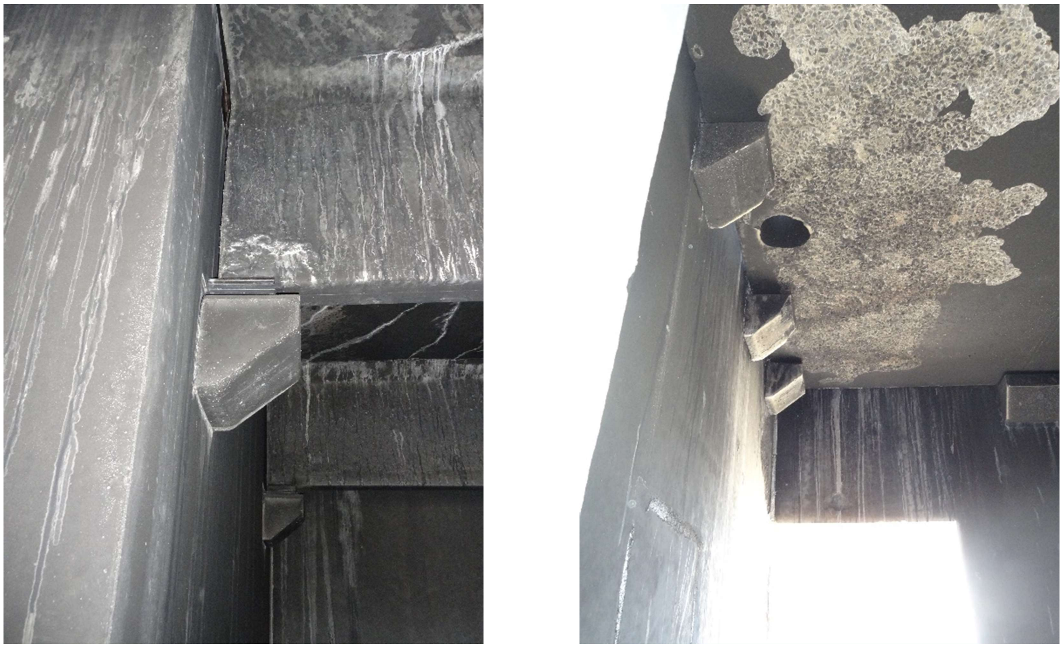

FIGURE 4.5: (a) Corbel and exposed bearing plates. (b) Ceiling spalling.

FIGURE 4.6: (a) Exposed reinforcement. (b) Corbel supporting double T joist.

From this background and short discussion, a design was made to facilitate testing of a precast concrete connection under conditions simulating a fire internal to a parking garage and a fire adjacent or external to the structure. In addition, a common structural connection was selected that is present in most multi-leveled parking structures. The connection chosen for testing in this thesis is a precast concrete corbel.

The corbel is critical to the structural integrity and stability of the parking garage as it supports significant floor and beam weight from above. Corbels are typically attached to either structural walls or columns and are attached by embedded steel plates and anchoring rebar. Figure 4.7 shows the finalized corbel designs featuring a 32" (0.8128 m) wide, 36" (0.9144 m) tall, and 8" (0.2032 m) thick small-scale precast wall with embedded vertical and top steel plates, varying corbel anchoring reinforcement, and two layers of mesh reinforcement within the wall. Refer to the Appendix for the complete drawings and details of the specimens. The corbel has a total depth of 16" (0.4064 m), a projection of 8" (0.2032 m), and a bearing length of 12" (0.3048 m). Each specimen weighs approximately 900 lbs. (4000 N). The overall width and height of the specimens were chosen to accommodate the testing apparatus.

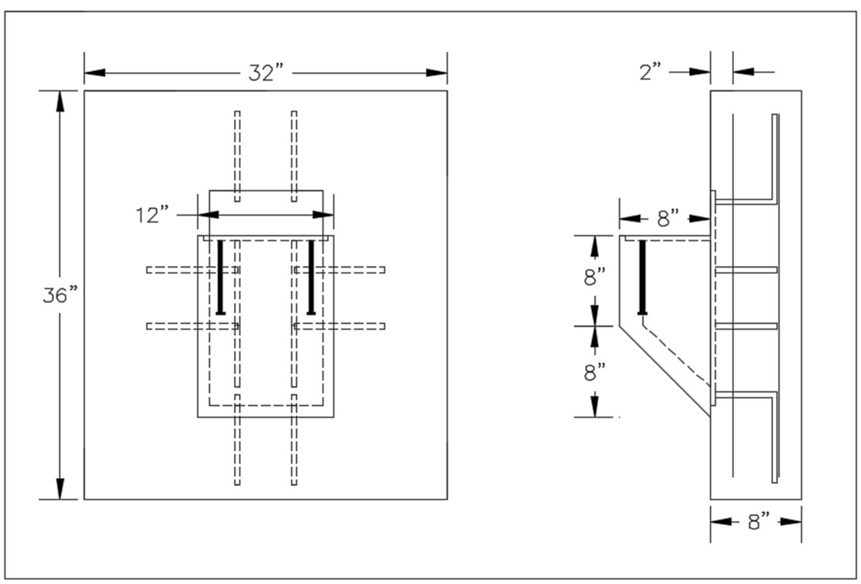

FIGURE 4.7: Example corbel specimen design, N1.

Table 4.1 shows the experimental test matrix. Six specimens of NW concrete and six specimens of LW concrete were created each with a 28-day compressive test design strength of 5,000 psi (34.5 MPa). Half of the specimens feature bent reinforcing bars from the corbel into the wall and the other half feature headed rebar studs. Two specimens, N1 and N4, were selected for testing simulating a fire internal to the structure, referred to subsequently as front face heating exposure. The remaining ten specimens were selected for testing simulating a fire external to the structure, referred to subsequently as rear face heating exposure.

TABLE 4.1: Test matrix for experimental testing.

Sample Number	Weight	Anchoring System	Heat Side	Label
1	NW	Bent Bars	Front	N1
2	NW	Bent Bars	Back	N2
3	NW	Bent Bars	Back	N3
4	NW	Headed Bars	Front	N4
5	NW	Headed Bars	Back	N5
6	NW	Headed Bars	Back	N6
7	LW	Bent Bars	Back	L7
8	LW	Bent Bars	Back	L8
9	LW	Bent Bars	Back	L9
10	LW	Headed Bars	Back	L10
11	LW	Headed Bars	Back	L11
12	LW	Headed Bars	Back	L12

4.3 Specimen Fabrication

Figures 4.8 through 4.10 document the casting process of the experimental test specimens. The NW specimens were cast on the rear face and the LW specimens were cast on the front face. For the LW specimens, the corbel was added to the specimen after casting the main wall section. It was desired to utilize three specimens for front face heating exposure. However due to different casting arrangements, it was not possible set up the required instrumentation within the corbel prior to casting for specimens L7 – L12. Therefore, the remaining specimens were utilized for testing in the rear face heating exposure configuration analogous to a fire external to the structure.

FIGURE 4.8: (a) Top down view of specimen prior to cast. (b) Interior view of corbel reinforcement.

FIGURE 4.9: (a) Interior view, bent bars. (b) Pouring and vibration of specimens.

FIGURE 4.10: (a) Top down view. (b) Pouring and vibration of specimens.

4.4 Heating Panel Design

In order to heat the specimens during testing, two Raymax 2030 panels were used as the heat source. Radiating panels have multiple benefits as opposed to open flame heating or other various methods. The low thermal inertia of infrared radiation heating systems eliminates the need for long pre-heat cycles, enabling the heaters to reach maximum operating temperature within a few minutes. Maximizing the time to reach operating temperatures also increases energy efficiency and savings during testing. Each panel is 36” (0.9144 m) high and 16” (0.4064 m) wide, with 576 in^2 (0.3716 m^2) of heated surface area and generates 20 W/in^2. Figure 4.11 shows the theoretical temperature curve of the heaters and the peak temperature of approximately 593 °C (1100 °F) reported by the manufacturer. In order to determine the actual temperature of the panels throughout each test, i.e. a representative fire curve, a different temperature monitoring device was used for calibration and will be discussed in subsection 4.5.3.

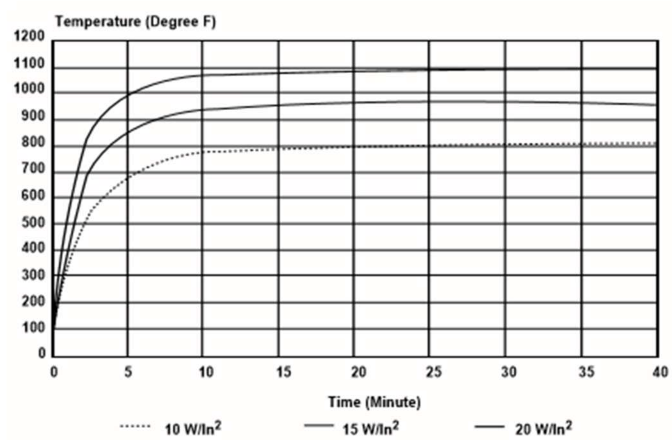

FIGURE 4.11: Raymax 2030 specifications (Watlow, 1997).

The concrete wall was 32” (0.8128 m) wide and 36” (0.9144 m) tall to match the width and height of two Raymax 2030 panels positioned side by side. From this, a steel frame was constructed in order to position the panels for testing. Figures 4.12 through 4.14 illustrate the frame construction process. The frame features two diagonal cross-bar connections to provide the lateral bracing. In addition, sand bags were placed on the legs to prevent overturning. Finally, the frame features multiple slots by which the elevation of the panels can be adjusted. The first slot places the panels at the height of a concrete masonry unit (CMU), for each test the specimens rested on 2 CMU blocks in order to elevate the specimen above the ground. Three holes are available above the CMU height position at 6” (0.1524 m) increments. Finally, the panels were connected to a main breaker and toggled either on or off for testing. Figure 4.14 presents photographs of the testing frame with the radiating panels installed. The panels were labeled as Panel A on the right side and Panel B on the left side.

FIGURE 4.12: (a) Frame construction progress. (b) Welding of cross bars.

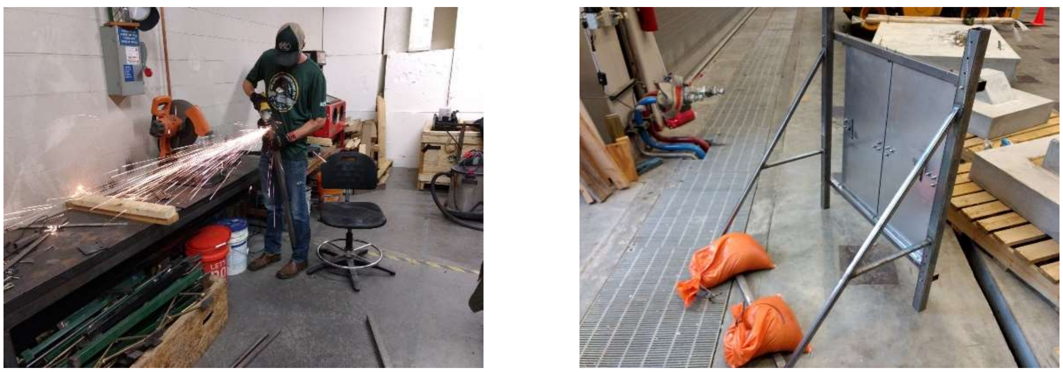

FIGURE 4.13: (a) Hand grinding for smooth edges. (b) Weighted down frame.

FIGURE 4.14: (a) Front view of testing frame. (b) Rear view of panels with protective connection plates.

4.5 Instrumentation

4.5.1 Thermistors

Two HTM2500LF temperature and relative humidity modules were each placed in two out of the 12 specimens. The four modules were used to track the moisture content from the cast date to the experiment test. The ideal target for moisture content with concrete when considering experimental fire testing is 75% based on ASTM E119. Due to the nature of concrete casting, vibrating, and curing, the modules needed to be durable enough to survive the casting process as well as remain functional after several months of curing. The chosen modules were designed for high reliability, long term stability, and resistance to damage. A power source and standard volt meter were used to determine the temperature and relative humidity based on resistance of the thermistor and conditioned voltage output from the relative humidity sensor. Figure 4.15 shows the setup and preparation of the modules. The modules were placed in specimens N5 and L11, each with two distinct modules, as shown in Figure 4.16 and 4.17.

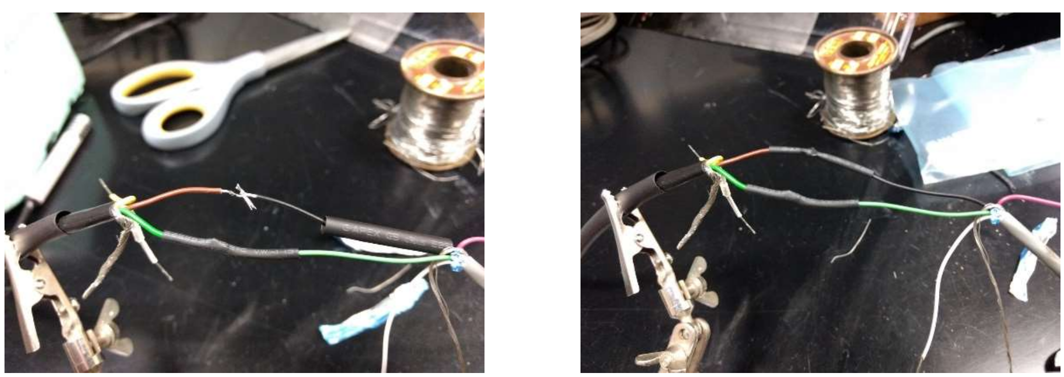

FIGURE 4.15: Module preparation with heat wrap and soldering wire.

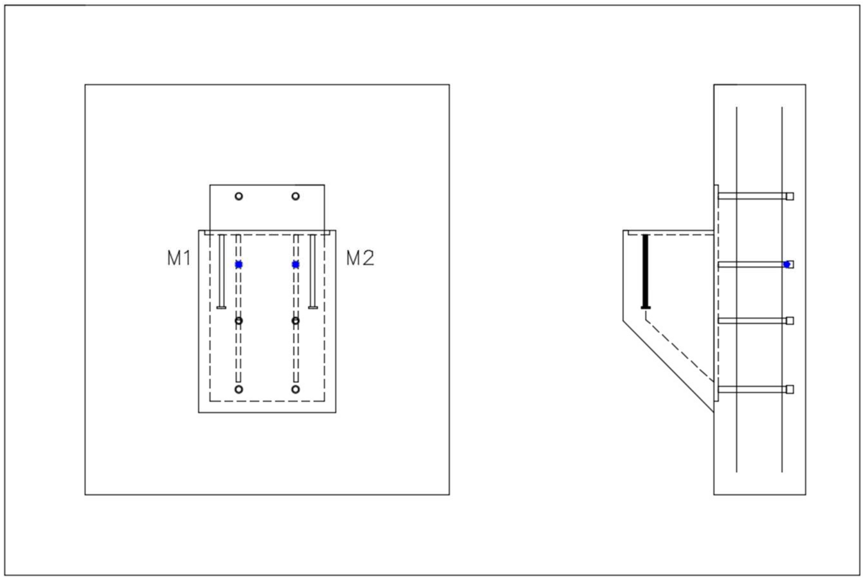

FIGURE 4.16: Specimen N5, moisture module locations of M1 and M2 (faulty).

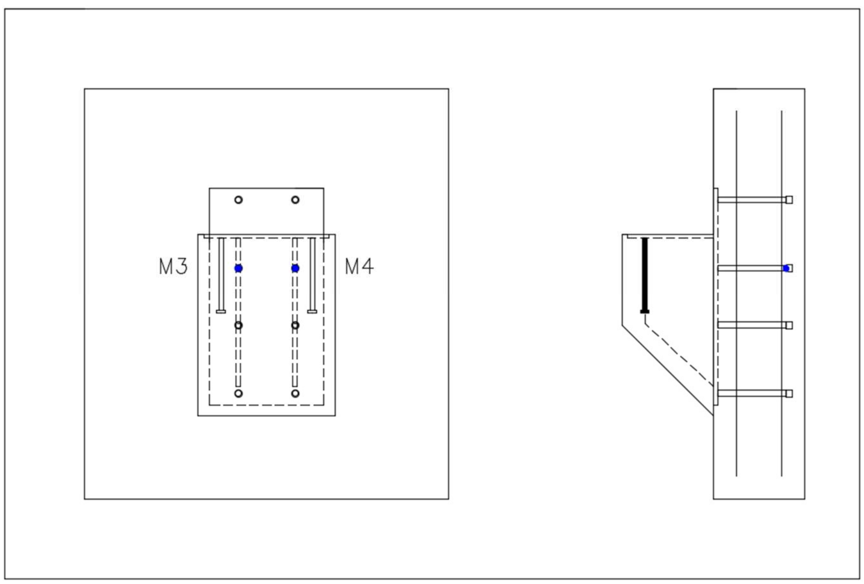

FIGURE 4.17: Specimen L11, moisture module locations of M3 and M4 (faulty).

4.5.2 Thermocouples

Thermocouples were installed prior to casting to measure the internal temperatures of the concrete and embedded steel elements during testing. Thermocouples are the standard instrument used for recording temperatures, whether embedded in objects or on the surface. The major concern in using thermocouples is selection of the appropriate thermocouple type and its applicable temperature range. The Raymax 2030 panels reach a maximum operating temperature of about 593 °C. Therefore, type K thermocouples were selected for use with 24-gauge, fiberglass wire that is rated to 482 °C. The thermocouple wire also features special limits of error (SLE). The SLE wire maintains accuracy within 4% across a temperature range from 0 °C to 1250 °C. Similar to the moisture modules, the instrumentation used needed to be durable enough to function after undergoing the casting, vibrating, and curing of the concrete.

It was determined that eight thermocouples would be installed in each specimen. For the specimens that were selected to be tested on the front face, four thermocouple locations were determined within the corbel and four thermocouple locations were distributed throughout the front reinforcing mesh. Figure 4.18 through Figure 4.29 present dimensioned drawings for the locations of all of the embedded thermocouples in each of the 12 specimens. For all other specimens with rear face heating exposure, four thermocouples were attached to the ends of either the bent bars or headed studs and four thermocouples were distributed throughout the rear reinforcing mesh. The thermocouples were labeled between 0 and 7 to match the channels of the data acquisition system. The locations of the thermocouples vary throughout each specimen due to the varying cuts of the reinforcing mesh used.

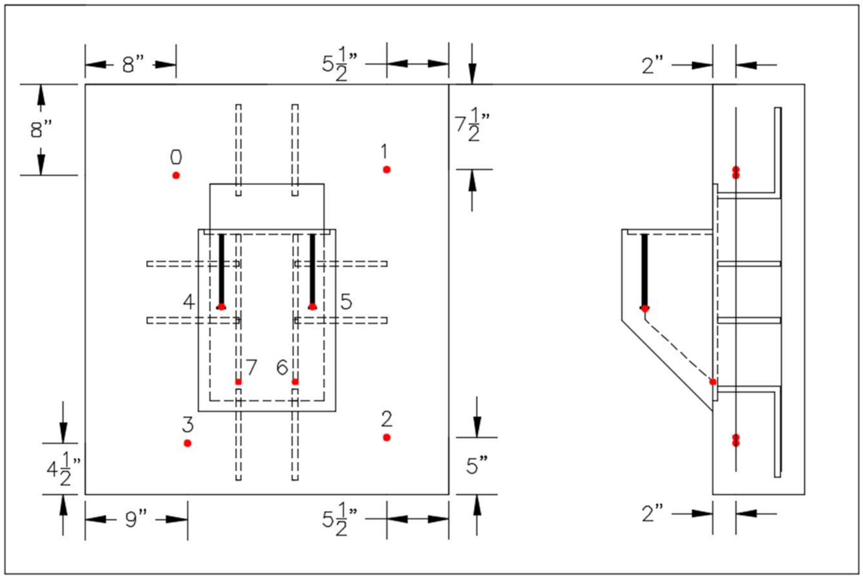

FIGURE 4.18: Thermocouple locations within specimen N1.

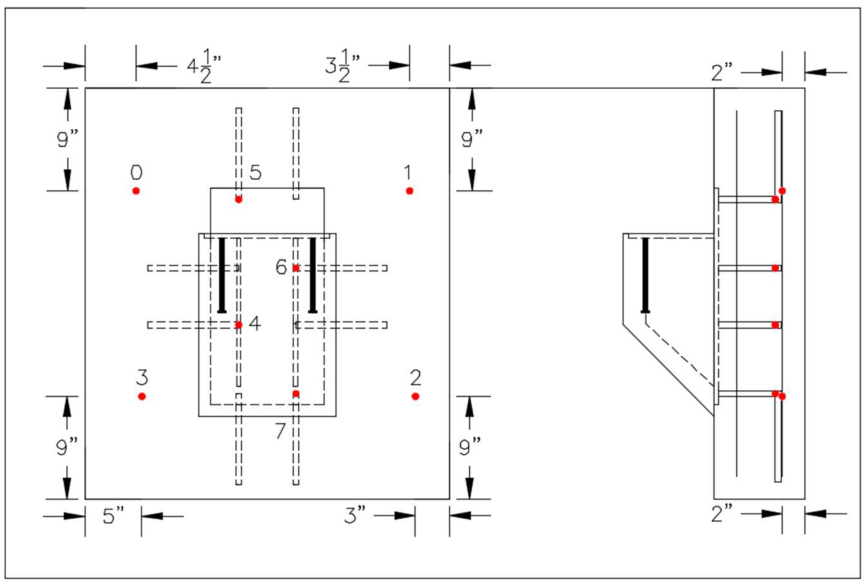

FIGURE 4.19: Thermocouple locations within specimen N2.

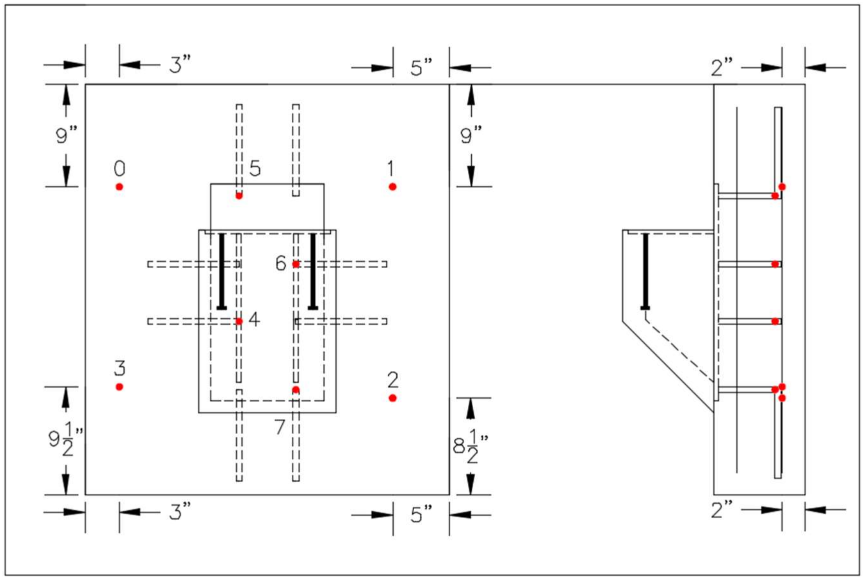

FIGURE 4.20: Thermocouple locations within specimen N3.

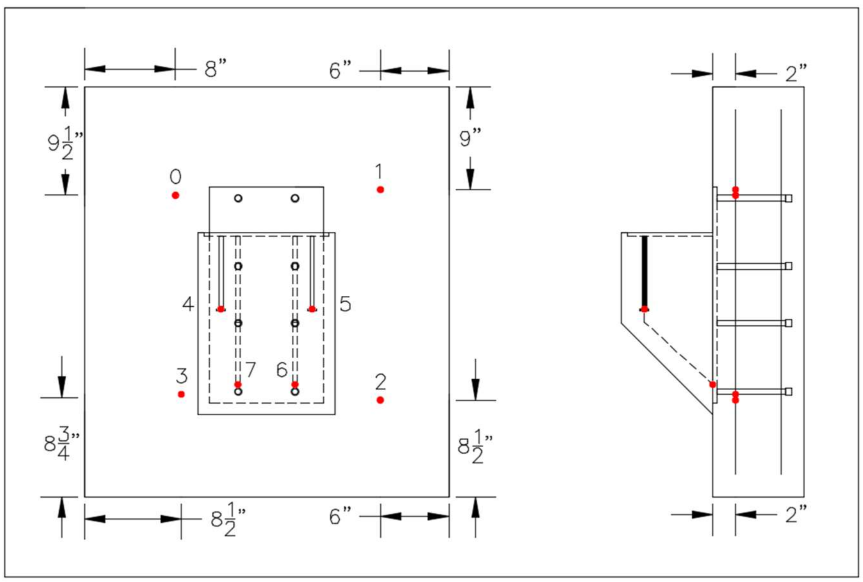

FIGURE 4.21: Thermocouple locations within specimen N4.

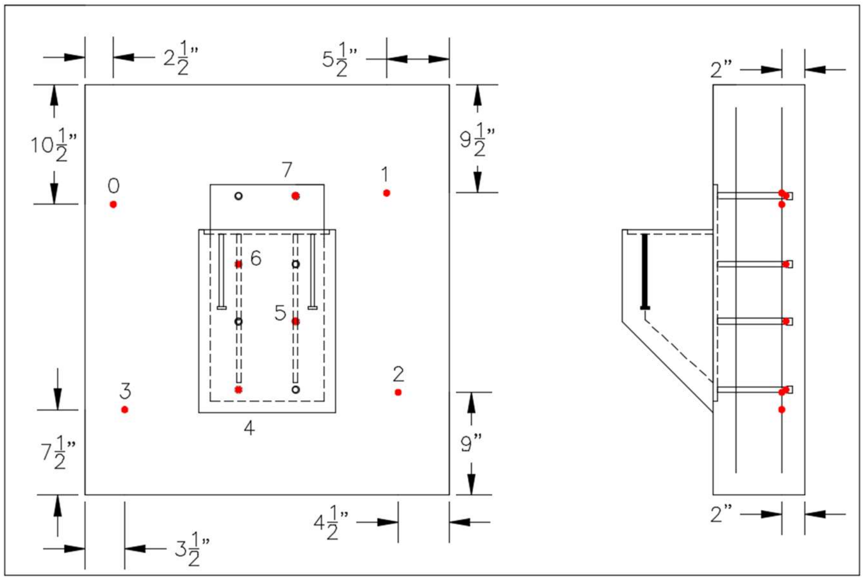

FIGURE 4.22: Thermocouple locations within specimen N5.

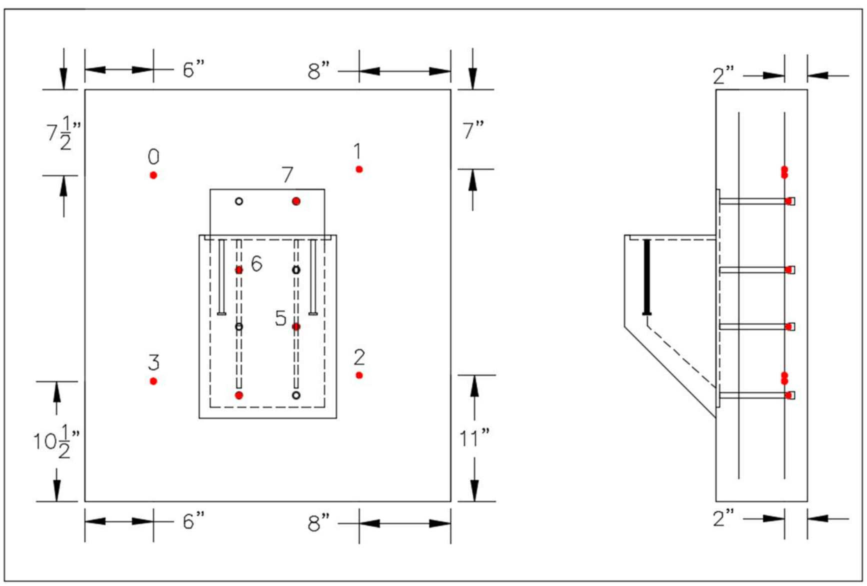

FIGURE 4.23: Thermocouple locations within specimen N6.

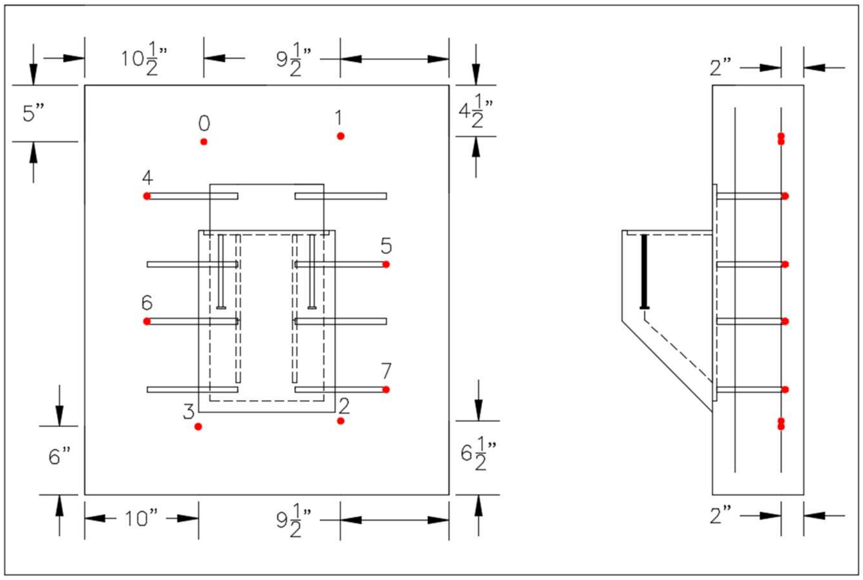

FIGURE 4.24: Thermocouple locations within specimen L7.

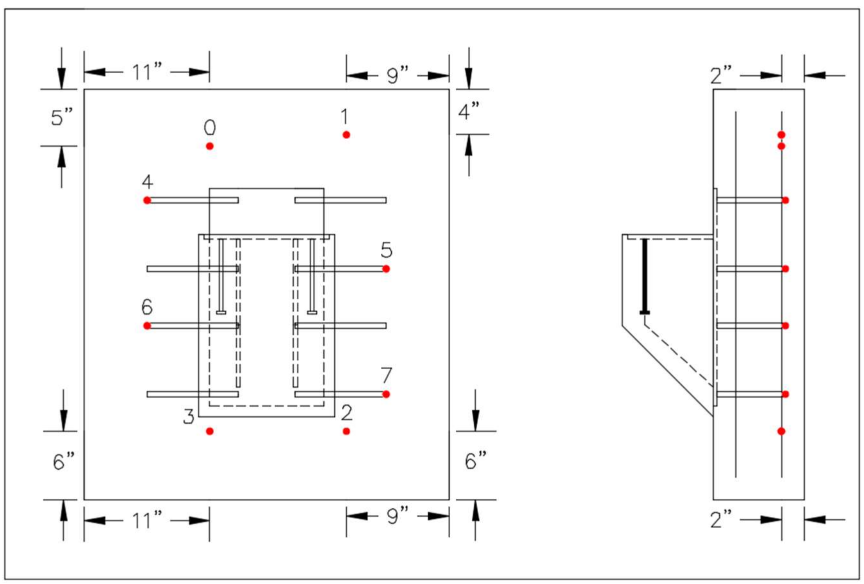

FIGURE 4.25: Thermocouple locations within specimen L8.

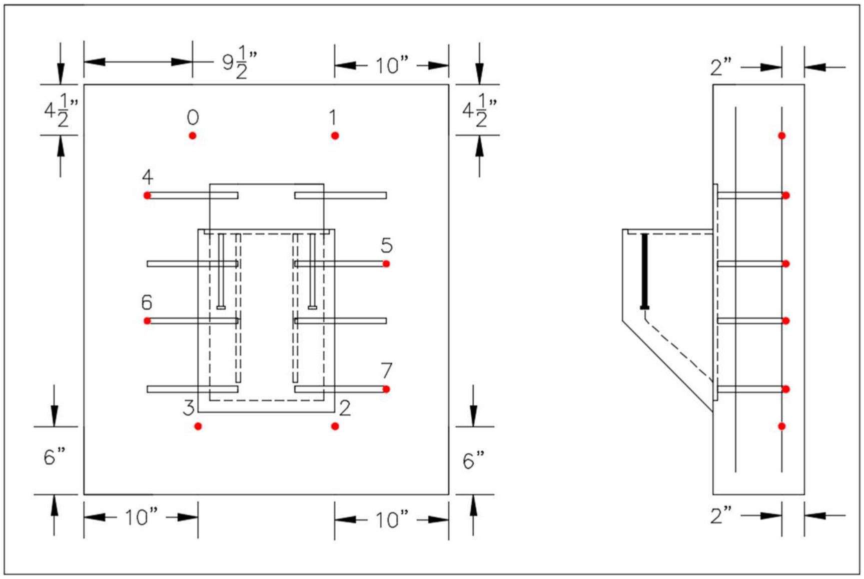

FIGURE 4.26: Thermocouple locations within specimen L9.

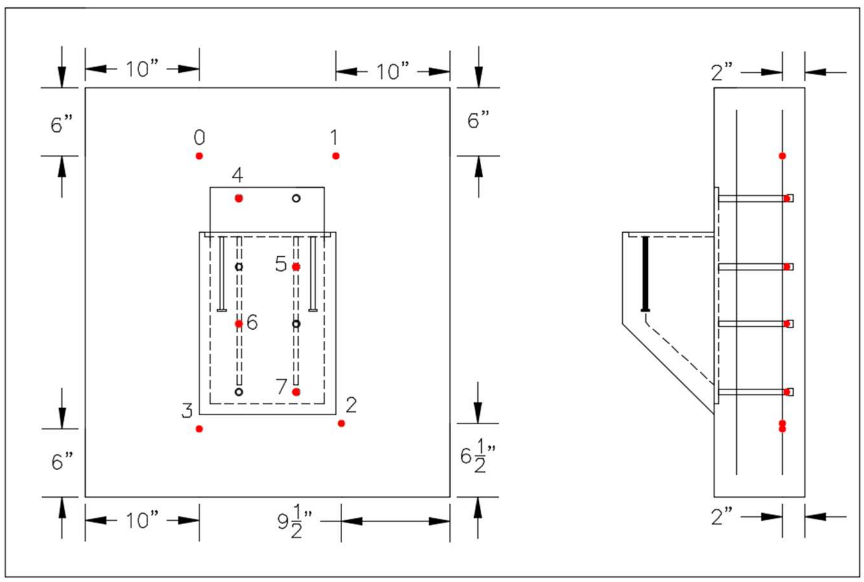

FIGURE 4.27: Thermocouple locations within specimen L10.

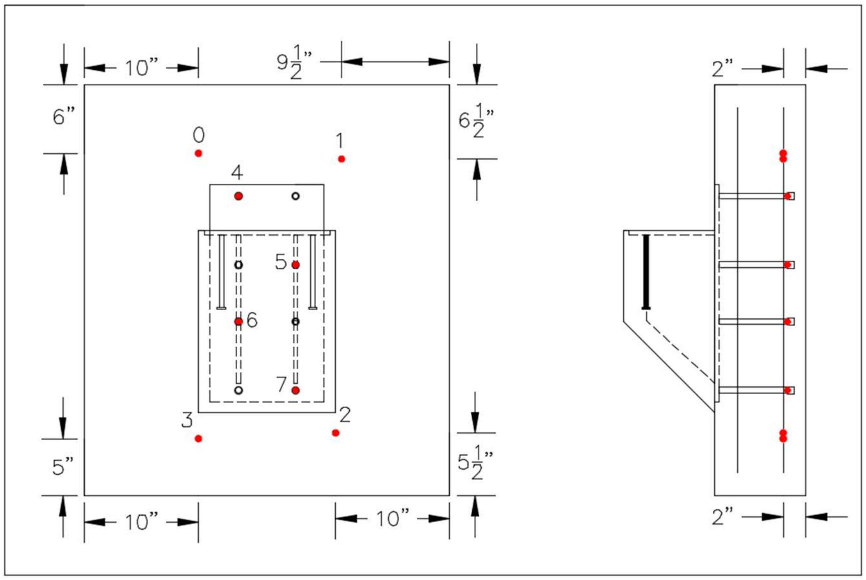

FIGURE 4.28: Thermocouple locations within specimen L11.

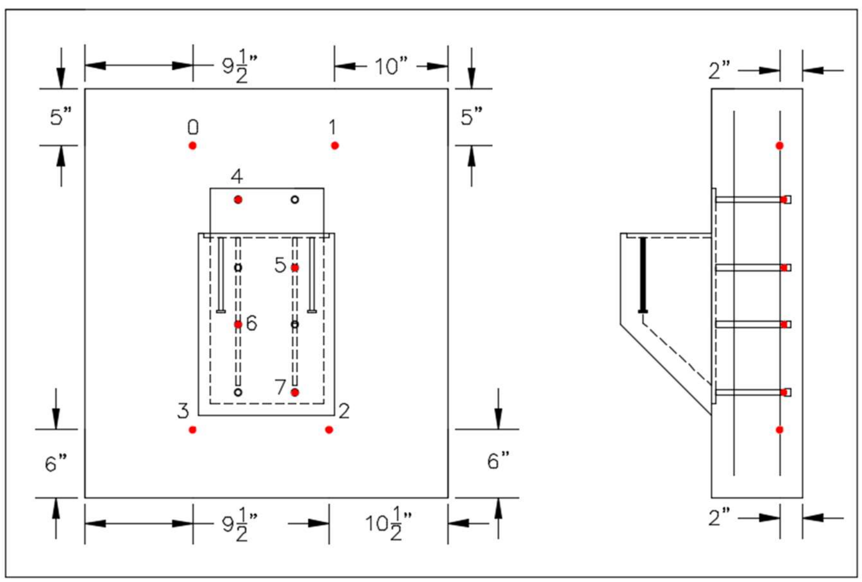

FIGURE 4.29: Thermocouple locations within specimen L12.

4.5.3 Infrared Camera and External Temperature Calibration

Figure 4.30 shows the Extech VIR50 infrared (IR) video thermometer used to measure the temperature output of the heating panel. The camera was used to obtain the temperature history of the face of Panel A, the corbel face, the front wall face, and finally, the rear wall face. The infrared camera recorded the temperature at each second throughout the duration of the test.

FIGURE 4.30: Front and rear face setups for calibration.

The selected Extech VIR50 camera is capable of measuring temperatures up to 2200 °C, capturing images and video, and recording time-temperature data. It utilizes a dual laser IR video thermometer that has an ideal measuring distance of 50 inches (1.27 m); at this distance the dual lasers converge to a 1-inch (0.0254 m) target spot. It should be noted that each test was completed at a 2-inch (0.0508 m) distance from the face of the panels. In the case of the front facing specimens, the front most face of the corbel was 2 inches (0.0508 m) from the panels, meaning that the front wall face was 10 inches (0.254 m) from the panels. Similarly for the rear facing specimens, the rear wall face of each specimen was placed 2 inches (0.0508 m) from the panels. Refer to Figure 4.30 for front and rear face setup examples. Figure 4.31 shows initial testing and connections of the thermocouples to data acquisition hardware.

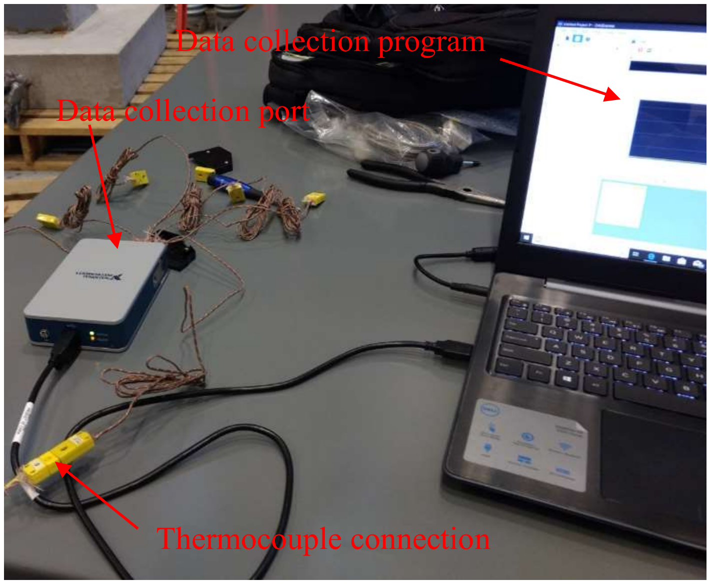

FIGURE 4.31: Thermocouple connections and data acquisition.

4.6 Data Acquisition

In order to collect and process the data obtained by the embedded thermocouples in each specimen, a data acquisition system was used to sample the voltage from each sensor and write the output in the form of time-temperature data into Excel for further processing. For each test, the opposite ends of the eight embedded thermocouples were connected to a National Instrument cDAQ-9171 bus-powered, compact chassis. The chassis then fed the data to a simple and efficient data collection program developed using National Instruments DAQExpress software. Similar to the handheld infrared camera, the thermocouple measurements were taken at every second throughout the duration of the tests. For each test performed, the thermocouple ports were given appropriate names to correspond with the specimen and location of the thermocouples, N5-0, N5-1, etc. In addition, the upper and lower bounds were entered for the thermocouple type; type K ranges from 0 °C to 482 °C. The program also used built in cold junction compensation to adjust for the ambient temperature at the chassis, relative to the temperature changes experienced within the specimen. Figure 4.32 shows the DAQExpress interface and arrangement of hardware.

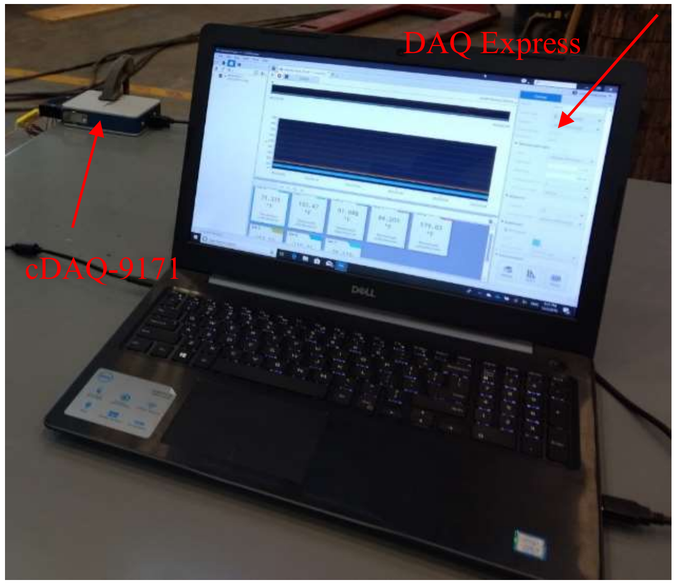

FIGURE 4.32: cDAQ -9171 chassis and DAQExpress program.

4.7 Results

Specimens N1 and N4 are both front facing experiments and N2, N3, N5, and N6 are all rear facing experiments. All LW specimens are rear facing experiments. Complete temperature time histories for NW specimens N1 through N6 and partial temperature time histories for LW specimens L8 and L10 are discussed. Due to high moisture content and severe spalling, specimens L7, L9, L11, and L12 have not yet been tested.

4.7.1 Relative Humidity of Specimens

For specimen N5, the relative humidity was monitored starting from 70 days after the cast date, August 24th, 2018, and then periodically until the experimental tests were completed late January 2019. The relative humidity for specimens 7-12 were monitored for two weeks. On the last day of testing the NW specimens, a relative humidity 85% was measured; the rate of decrease in moisture content had essentially slowed to zero at this time. The relative humidity of the LW specimens was recorded at 95%. The sensors labeled M1 and M3 provided accurate data, while the modules labeled M2 and M4 provided erroneous data with relative humidity percentages higher than 100%. Figures 4.33 and Table 4.2 present the relative humidity of specimen N5 monitored over 5 months.

TABLE 4.2: Module M1 monitoring results.

Days Since Casting	Date cast	Output Resistance (Ohm) Module: M1	Temperature (°C)	Temperature (°F)	Relative Humidity (Voltage)	Relative Humidity (%)
Specimen N5	8/24/2018	/	/	/	/	/
70	11/2/2018	12230	19.72	67.50	3520	94.25
75	11/7/2018	11750	20.76	69.37	3530	94.58
88	11/20/2018	11600	21.09	69.97	3490	93.24
98	11/30/2018	11600	21.09	69.97	3450	91.88
109	12/11/2018	12040	20.13	68.23	3370	89.11
138	1/9/2019	12000	20.21	68.38	3280	85.92
147	1/18/2019	11840	20.56	69.01	3270	85.56
153	1/24/2019	11550	21.21	70.17	3270	85.56
157	1/28/2019	11740	20.78	69.41	3270	85.56
159	1/30/2019	12110	19.98	67.96	3250	84.84

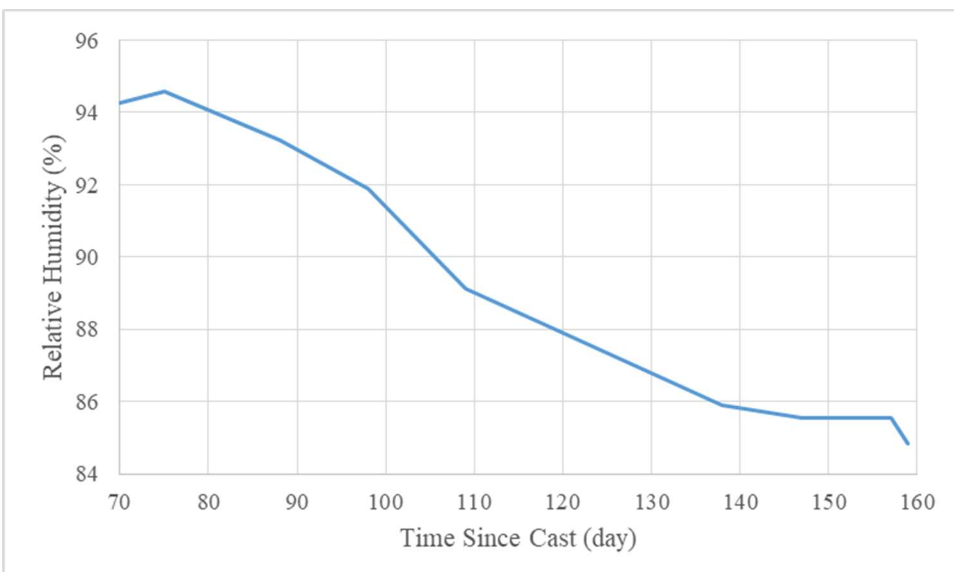

FIGURE 4.33: Relative humidity of module M1 vs. curing timeline.

4.7.2 Heating Panel Load

During the testing of specimen N4, the camera was focused at the middle of Panel A for the duration of the test. Figure 4.34 compares the temperature history of heating Panel A, to the ASTM E119 standard fire curve. Both curves exhibit a rapid increase in temperature within the first 5 minutes of heating. However, the E119 curve continues to increase in temperature for up to 2 hours, as shown in Figure 2.3, while the representative fire curve for the panels reaches 538 °C after 7 minutes and slowly increases to a maximum operating temperature of about 563 °C for the following 53 minutes of the test.

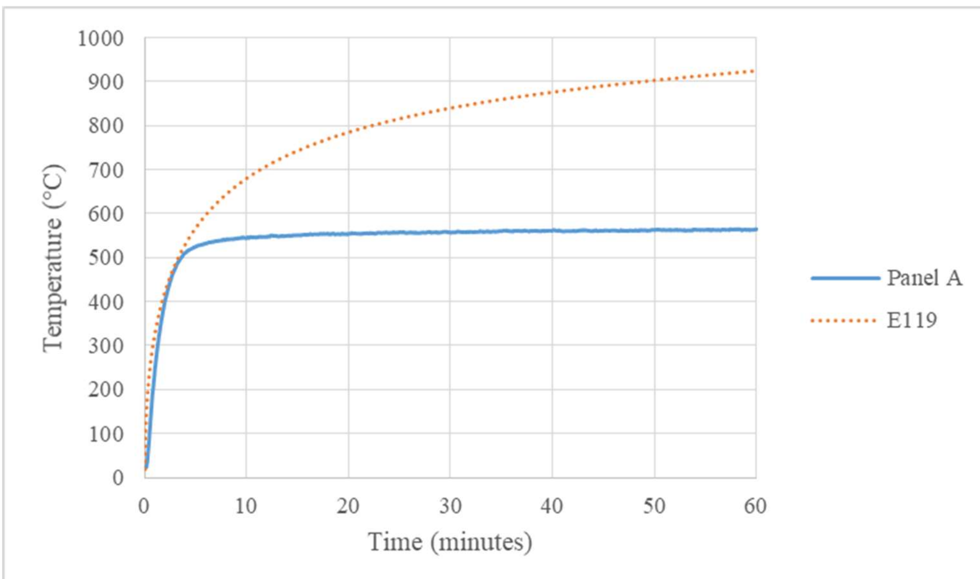

FIGURE 4.34: Panel A vs. ASTM E119 fire curve comparison.

4.7.3 Specimen Surface Temperatures

Similarly, during the testing of specimen N1, the camera was focused at the middle of the front face of the corbel, 2 inches from the source of heat. The corbel face reached a maximum temperature of about 368 °C over the duration of the fire and would reasonably be expected to continue to increase if the test exceeded 60 minutes. In order to obtain the front wall face surface temperatures, specimen N4 was subjected to another complete test.

The behavior of specimen N4 is assumed to behave the same for this second test since there were no visible signs of damage, cracking, or leakage resulting from the first test. The maximum temperature reached at the wall face was 331 °C. The camera was focused at an arbitrary location centered between the corbel and the edge of the wall. Refer to Figure 4.35 for a comparison between the temperature history for the representative fire curve of Panel A and the temperature histories for the surfaces of the corbel and wall face.

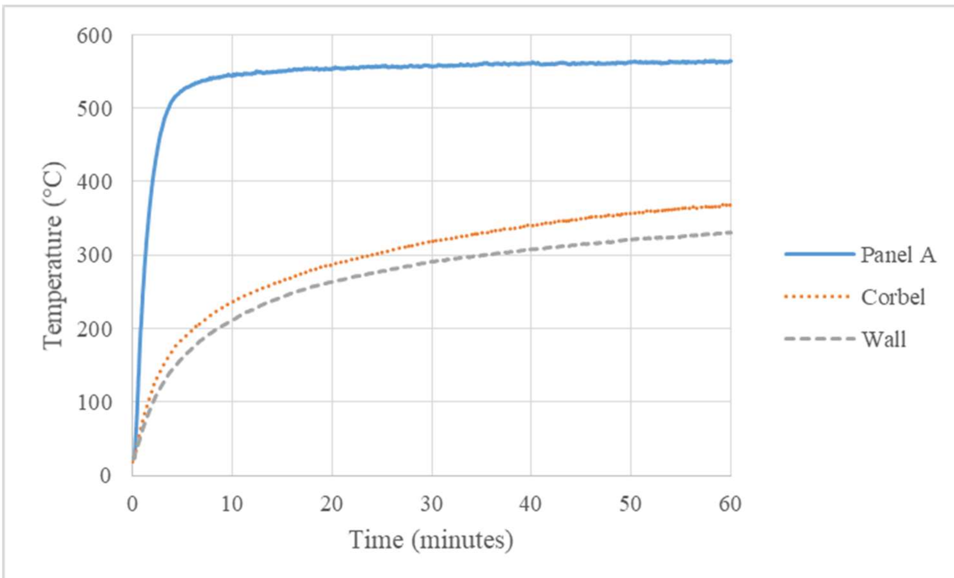

FIGURE 4.35: Front corbel, wall face, and Panel A temperature comparison.

Finally, during testing of specimens N2, N3, and N5 the camera was focused on the back face of wall, also at a 2-inch (0.0508 m) distance from the heat source. Another sample of data from the rear face would have been collected from the testing of specimen N6 had the battery of the camera not died during the test, resulting in an incomplete set of data. Refer to Figure 4.36 for a comparison between the resulting rear face temperatures and the representative fire curve of Panel A. Unfortunately, the rear wall temperatures obtained from specimen N2 provided erroneous data as the camera was not focused correctly on to the surface of the wall. Therefore, only the rear wall temperature obtained from testing specimens N3 and N5 will be considered for comparison.

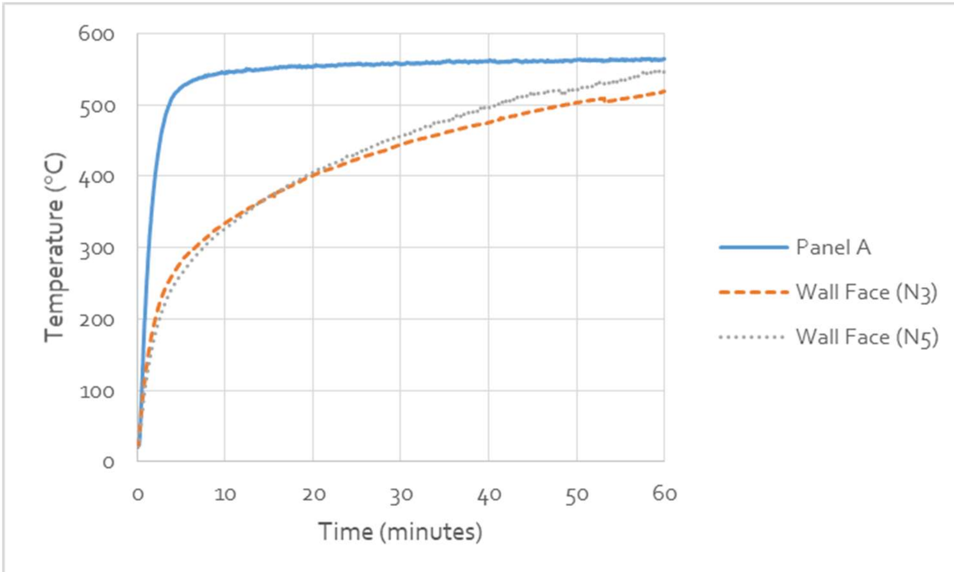

FIGURE 4.36: Rear wall face and Panel A temperature comparison.

4.7.4 Specimen N1 Results

Figure 4.37 shows specimen N1 during testing with front face heating of the corbel and wall system, where the heating panel was positioned 2” (0.0508 m) from the corbel. The specimen was heated for 60 minutes and measurements for all instrumentation were taken each second.

FIGURE 4.37: Testing of specimen N1.

Table 4.3 and Table 4.4 show the critical temperatures obtained from the test. Figures 4.38 and 4.39 show the temperature time histories for specimen N1. Thermocouple N1-7 failed to record accurate temperatures. It is most probable that this thermocouple experienced damage during the testing or curing process of the concrete or during the setup prior to testing. The specimen appeared to have no visible damage, cracking, or leakage during this test.

TABLE 4.3: Critical mesh temperatures for specimen N1.

Critical Mesh Temperatures (°C)					
Time	N1-0	N1-1	N1-2	N1-3	Average
10 min	21	22	23	24	22
20 min	30	32	36	37	34
30 min	43	45	50	52	47
40 min	55	60	62	65	60
50 min	67	71	72	76	72
60 min	78	81	82	87	82

TABLE 4.4: Critical corbel temperatures for specimen N1.

Critical Corbel Temperatures (°C)					
Time	N1-4	N1-5	N1-6	N1-7	Average
10 min	36	32	31	16	33
20 min	76	67	50	2	65
30 min	114	106	67	-13	95
40 min	131	128	80	-27	113
50 min	145	140	94	-41	126
60 min	162	149	105	-54	138

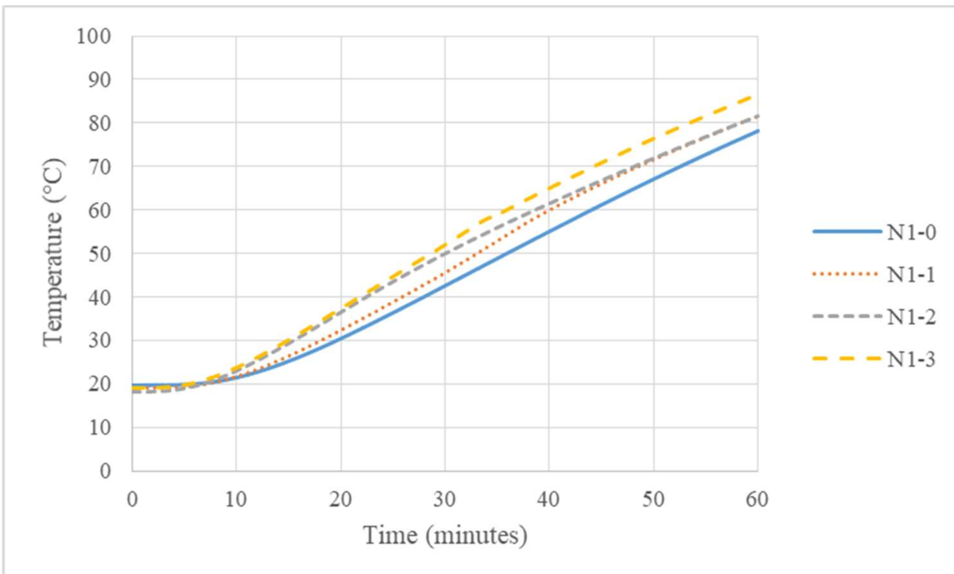

FIGURE 4.38: Specimen N1: Reinforcement mesh temperature histories.

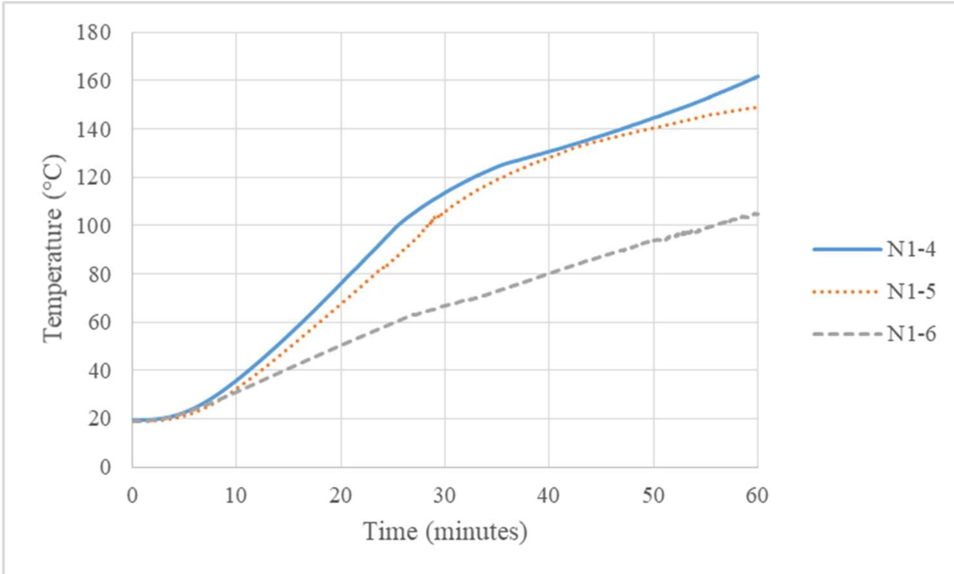

FIGURE 4.39: Specimen N1: Interior corbel temperature histories.

4.7.5 Specimen N2 Results

Figure 4.40 shows specimen N2, tested with back side heating of the rear face of the wall, where the heating panel was 2” (0.0508 m) from the wall.

FIGURE 4.40: Testing of specimen N2.

Table 4.5 and Table 4.6 show the critical temperatures obtained from the test. Figures 4.41 and 4.42 show the temperature time histories for specimen N2. Thermocouple N2-7 failed to record accurate temperatures.

TABLE 4.5: Critical mesh temperatures for specimen N2.

Critical Mesh Temperatures (°C)					
Time	N2-0	N2-1	N2-2	N2-3	Average
10 min	34	38	45	43	40
20 min	71	76	91	89	82
30 min	108	110	123	119	115
40 min	124	123	141	141	132
50 min	141	131	152	156	145
60 min	159	138	160	173	157

TABLE 4.6: Critical bent bar temperatures for specimen N2.

Critical Bent Bar Temperatures (°C)					
Time	N2-4	N2-5	N2-6	N2-7	Average
10 min	38	31	31	23	33
20 min	82	63	61	27	69
30 min	114	98	100	22	104
40 min	135	112	118	20	122
50 min	153	123	130	20	136
60 min	173	134	141	20	150

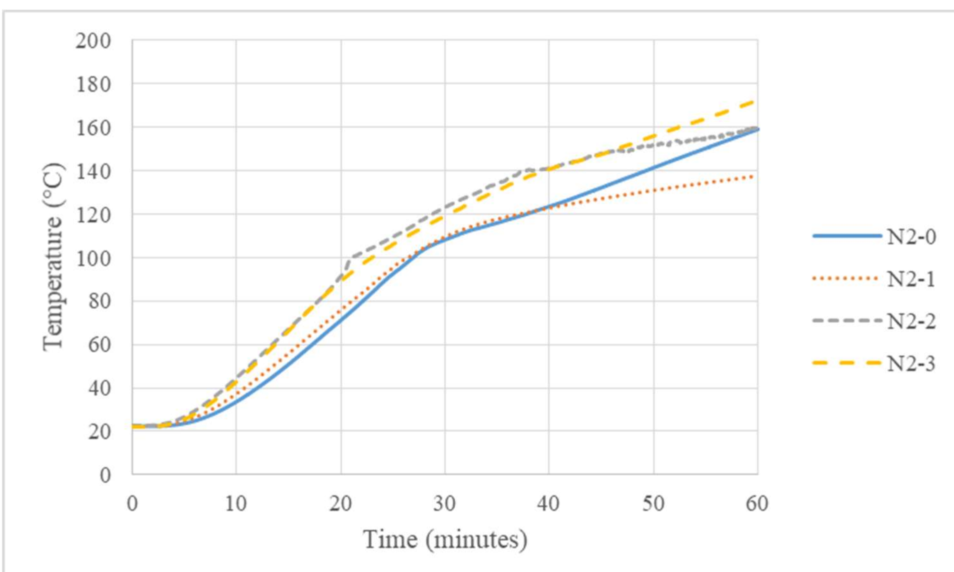

FIGURE 4.41: Specimen N2: Reinforcement mesh temperature histories.

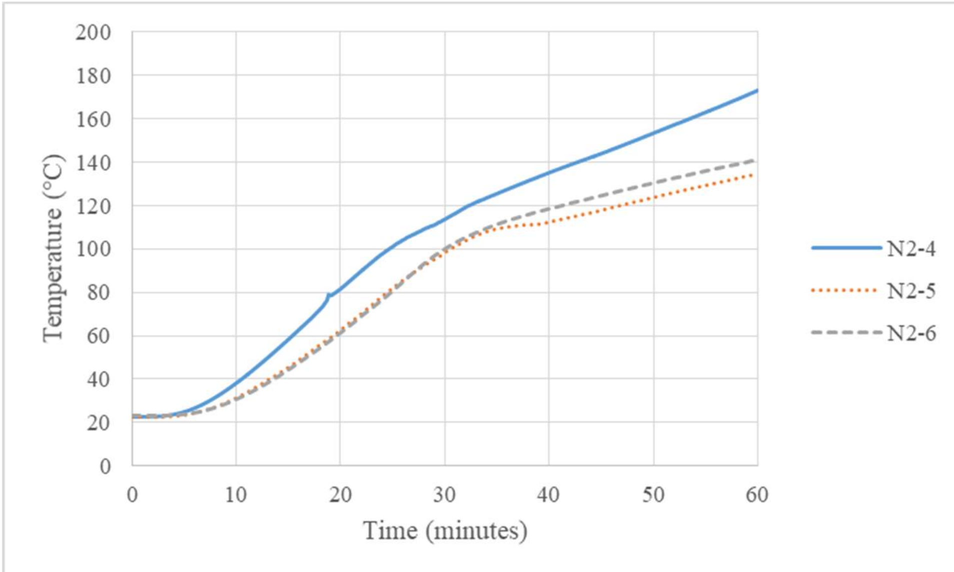

FIGURE 4.42: Specimen N2: Bent bar temperature histories.

During this test, significant leakage throughout the sides and eventually the front face of the wall was observed. In addition, the plastic reinforcing chairs that remained in the specimen melted rapidly as the test began. At approximately 15-minutes into testing the reinforcing chairs melted such that the pressure from the water and plastic caused spalling on the rear face of the wall; this occurred at the location of the plastic chairs as seen in Figure 4.43. Finally, after completing the test and removing the specimen from the testing area, standard map cracking was observed on the front face of the specimen as highlighted in Figure 4.46.

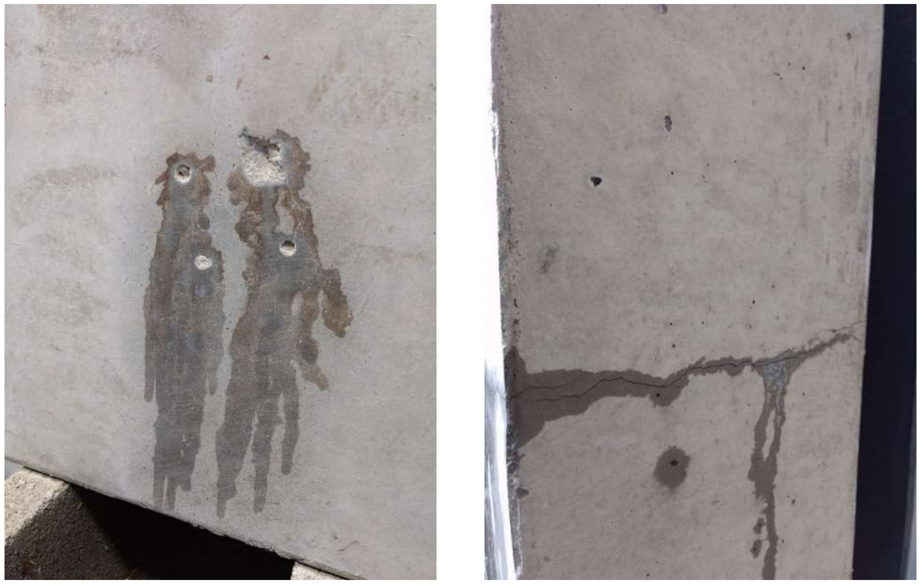

FIGURE 4.43: Leakage in specimen N2: (a) Plastic reinforcement chairs. (b) Horizontal cracking.

FIGURE 4.44: Specimen N2: Initial cracking and leakage, corner to front face.

FIGURE 4.45: Specimen N2: Significant moisture leakage across specimen.

FIGURE 4.46: Specimen N2: Map cracking on corbel face after experimental test.

4.7.6 Specimen N3 Results

Figure 4.47 shows specimen N3, tested with back side heating of the rear face of the wall, where the heating panel was 2” (0.0508 m) from the wall.

FIGURE 4.47: Testing of specimen N3.

Table 4.7 and Table 4.8 show the critical temperatures obtained from the test. Figures 4.48 and 4.49 show the temperature time histories for specimen N3. Thermocouple N3-2 failed to record accurate temperatures.

TABLE 4.7: Critical mesh temperatures for specimen N3.

Critical Mesh Temperatures (°C)					
Time	N3-0	N3-1	N3-2	N3-3	Average
10 min	36	42	19	29	36
20 min	80	89	19	58	76
30 min	113	124	23	92	110
40 min	129	145	22	112	129
50 min	147	161	22	124	144
60 min	165	181	22	138	161

TABLE 4.8: Critical bent bar temperatures for specimen N3.

Critical Bent Bar Temperatures (°C)					
Time	N3-4	N3-5	N3-6	N3-7	Average
10 min	26	22	25	29	25
20 min	53	39	50	50	48
30 min	99	62	81	71	78
40 min	108	101	111	90	102
50 min	121	104	128	105	114
60 min	135	108	135	117	124

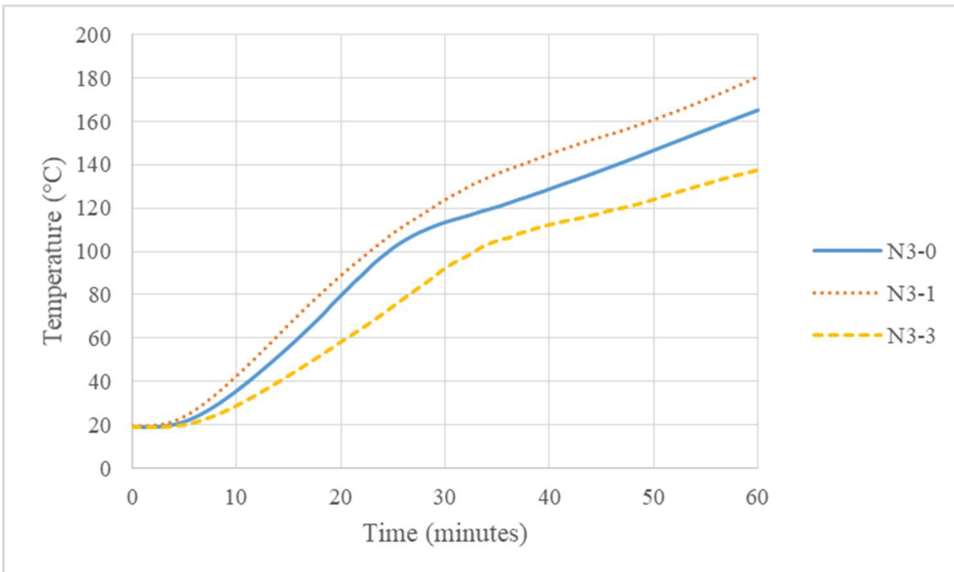

FIGURE 4.48: Specimen N3: Reinforcement mesh temperature histories

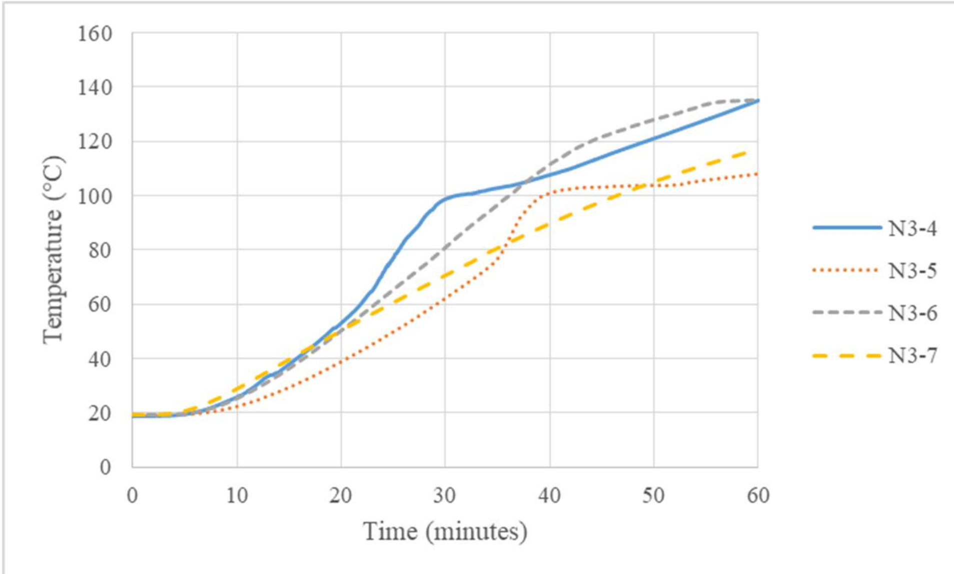

FIGURE 4.49: Specimen N3: Bent bar temperature histories.

This specimen experienced cracking and leakage throughout the test comparable to specimen N2 (Figure 4.50). A discernable pattern was also observed considering the crack formation along the sides of the specimens. The horizontal cracks appear to be spaced by about 6 inches. The horizontal cracks also spread towards the front face of the wall and inwards to the corbel and wall interface (Figure 4.51).

FIGURE 4.50: Specimen N3: (a) Initial cracking, 15 minutes. (b) Moisture leakage.

FIGURE 4.51: Specimen N3: Formation of tiered cracking.

4.7.7 Specimen N4 Results

Figure 4.52 shows specimen N4 during testing with front face heating of the corbel and wall system, where the heating panel was 2” (0.0508 m) from the corbel. The specimen was heated for 60 minutes and measurements for all instrumentation were taken each second.

FIGURE 4.52: Testing of specimen N4.

Table 4.9 and Table 4.10 show the critical temperatures obtained from the test. Figures 4.53 and 4.54 show the temperature time histories for specimen N4. Note that for this test both N4-0 and N4-7 did not record temperatures correctly. Additionally, thermocouple N4-1 possessed an unforeseen faulty connection. It is most probable that there was an instrument connection along the full length of the thermocouple, as indicated by the frequent drops in temperature.

TABLE 4.9: Critical mesh temperatures for specimen N4.

Critical Mesh Temperatures (°C)					
Time	N4-0	N4-1	N4-2	N4-3	Average
10 min	14	23	23	23	23
20 min	-14	34	34	30	32
30 min	-38	52	48	41	47
40 min	-59	54	61	52	56
50 min	-73	84	73	62	73
60 min	-87	98	83	72	84

TABLE 4.10: Critical corbel temperatures for specimen N4.

Critical Corbel Temperatures (°C)					
Time	N4-4	N4-5	N4-6	N4-7	Average
10 min	38	34	29	26	34
20 min	87	76	45	28	69
30 min	133	120	61	29	105
40 min	168	157	76	29	134
50 min	196	186	90	29	157
60 min	219	209	99	30	175

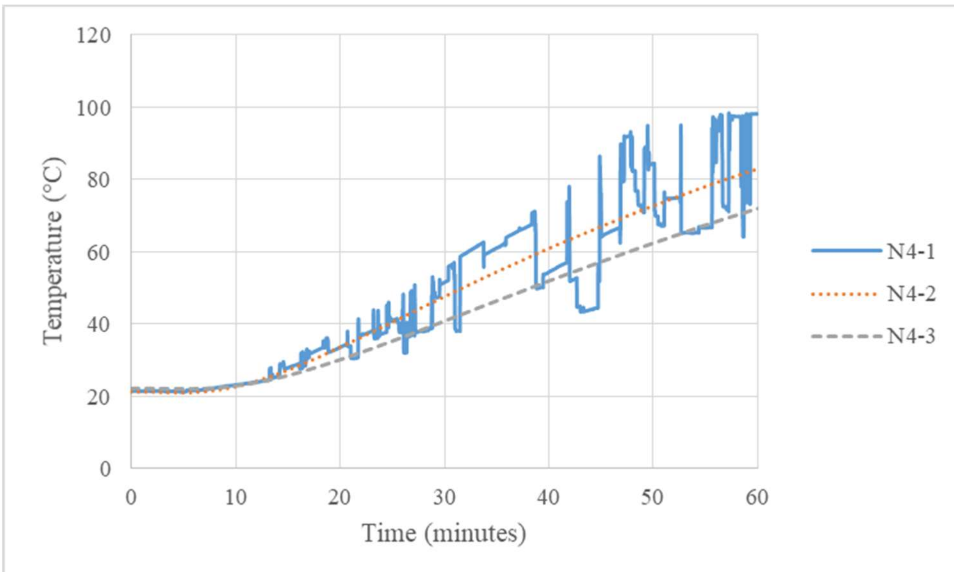

FIGURE 4.53: Specimen N4: Reinforcement mesh temperature histories.

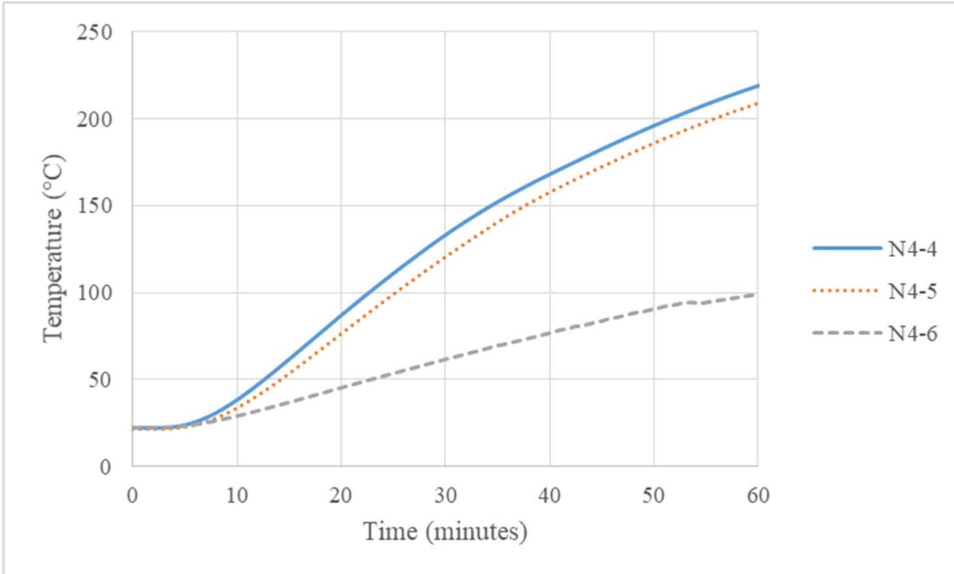

FIGURE 4.54: Specimen N4: Interior corbel temperature histories.

Specimen N4 was tested about the front face of the corbel and wall system. Similar to the results for specimen N1, this test produced no visible cracking or leakage throughout the system.

4.7.8 Specimen N5 Results

Figure 4.55 shows specimen N5, tested with back side heating of the rear face of the wall, where the heating panel was 2” (0.0508 m) from the wall.

FIGURE 4.55: Testing of specimen N5.

Table 4.11 and Table 4.12 show the critical temperatures obtained from the test. Figures 4.56 and 4.57 show the temperature time histories for specimen N5. This specimen exhibited the largest number of faulty thermocouple connections throughout the duration of the test. Thermocouple N5-0 malfunctioned similar to some of the previous thermocouples that display either ambient temperatures or a significantly less temperatures towards the end of the test. In addition, thermocouples N5-5 and N5-7 exhibited faulty connections, as the plots of the data provided inaccurate temperature drops and jagged lines as opposed to smooth curves. Thermocouples N5-0, N5-5, and N5-7 were removed from the temperature histories provided in Figures 4.56 and 4.57.

TABLE 4.11: Critical mesh temperatures for specimen N5.

Critical Mesh Temperatures (°C)					
Time	N5-0	N5-1	N5-2	N5-3	Average
10 min	22	34	21	33	33
20 min	20	68	29	69	68
30 min	20	100	42	104	102
40 min	19	124	59	126	125
50 min	21	140	82	140	140
60 min	20	149	97	154	152

TABLE 4.12: Critical headed bar temperatures for specimen N5.

Critical Headed Bar Temperatures (°C)					
Time	N5-4	N5-5	N5-6	N5-7	Average
10 min	38	45	46	50	45
20 min	79	97	90	98	91
30 min	111	119	121	130	120
40 min	130	139	144	154	142
50 min	151	167	166	175	165
60 min	172	192	189	198	188

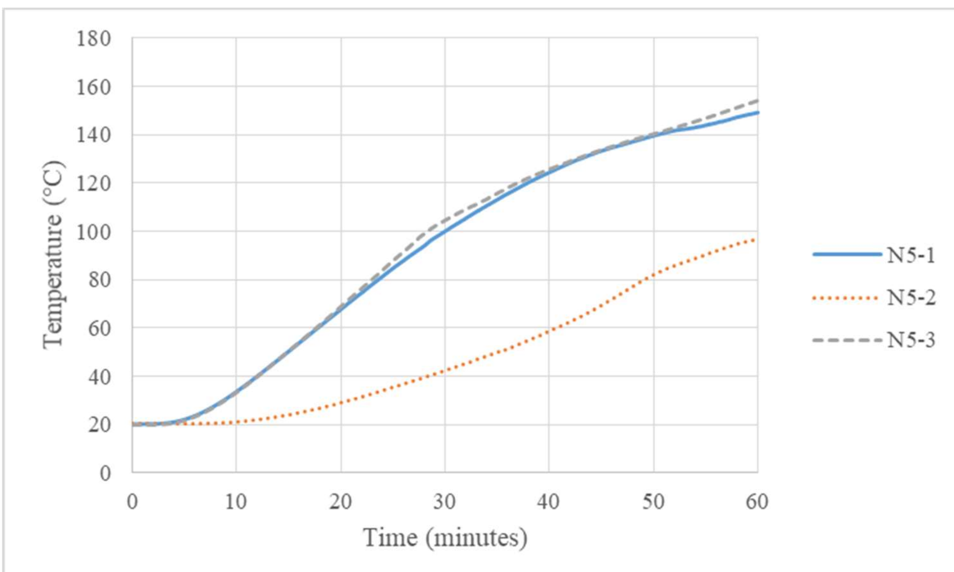

FIGURE 4.56: Specimen N5: Reinforcement mesh temperature histories.

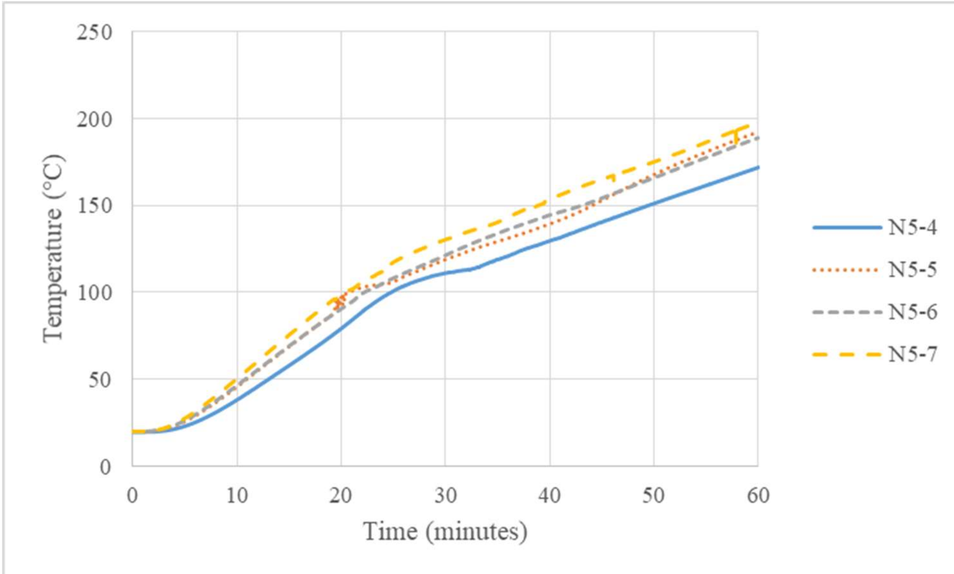

FIGURE 4.57: Specimen N5: Headed bar temperature histories

Specimen N5 was tested about the rear face of the wall. Cracking and moisture leakage occurred roughly 15 minutes into testing. A distinct cracking pattern was also observed in this test consistent with the previous rear facing experiments. The horizontal cracks appear about 6 inches (0.1524 m) above or below the previous crack, resembling a tiered or layered crack formation along both side faces of the specimen. In addition, these cracks sometimes spread to the front face of the wall and inwards towards the corbel interface. Figure 4.58 shows the cracking patterns observed.

FIGURE 4.58: Specimen N5: Formation of tiered cracking.

4.7.9 Specimen N6 Results

Figure 4.59 shows specimen N6, tested with back side heating of the rear face of the wall, where the heating panel was 2” (0.0508 m) from the wall.

FIGURE 4.59: Testing of specimen N6.

Table 4.13 and Table 4.14 show the critical temperatures obtained from the test. Figures 4.60 and 4.61 show the temperature time histories for specimen N6. All eight thermocouples functioned correctly throughout the duration of the test. Overall, specimen N6 produced the most complete data, relative to the rest of the specimens that experienced some extent of difficulty with thermocouple connections.

TABLE 4.13: Critical mesh temperatures for specimen N6.

Critical Mesh Temperatures (°C)					
Time	N6-0	N6-1	N6-2	N6-3	Average
10 min	36	36	35	48	39
20 min	84	81	79	100	86
30 min	122	122	116	134	124
40 min	142	145	134	161	146
50 min	164	160	152	189	166
60 min	189	178	176	214	189

TABLE 4.14: Critical headed bar temperatures for specimen N6.

Critical Headed Bar Temperatures (°C)					
Time	N6-4	N6-5	N6-6	N6-7	Average
10 min	36	38	36	33	36
20 min	77	81	77	69	76
30 min	110	117	113	105	111
40 min	131	140	131	121	131
50 min	154	157	152	138	150
60 min	175	178	174	157	171

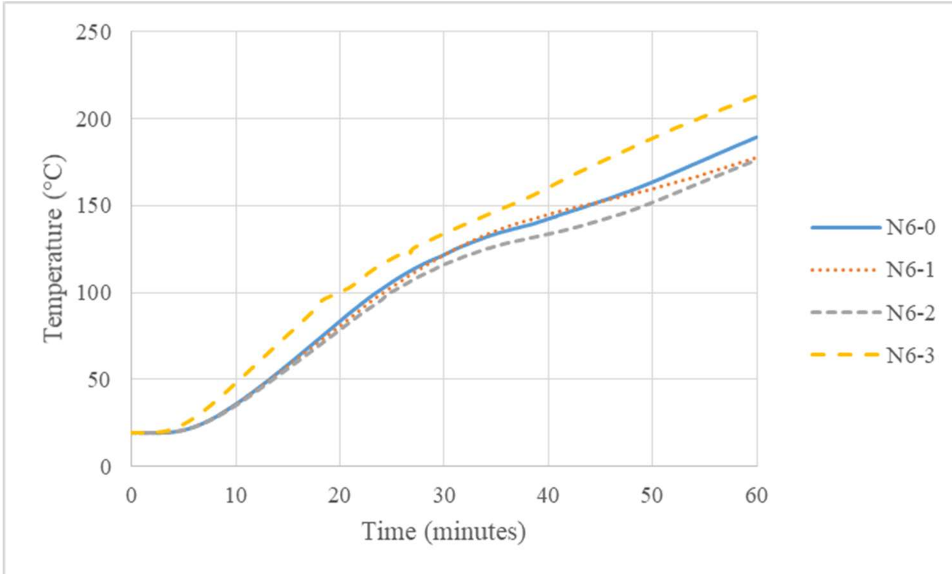

FIGURE 4.60: Specimen N6: Reinforcement mesh temperature histories.

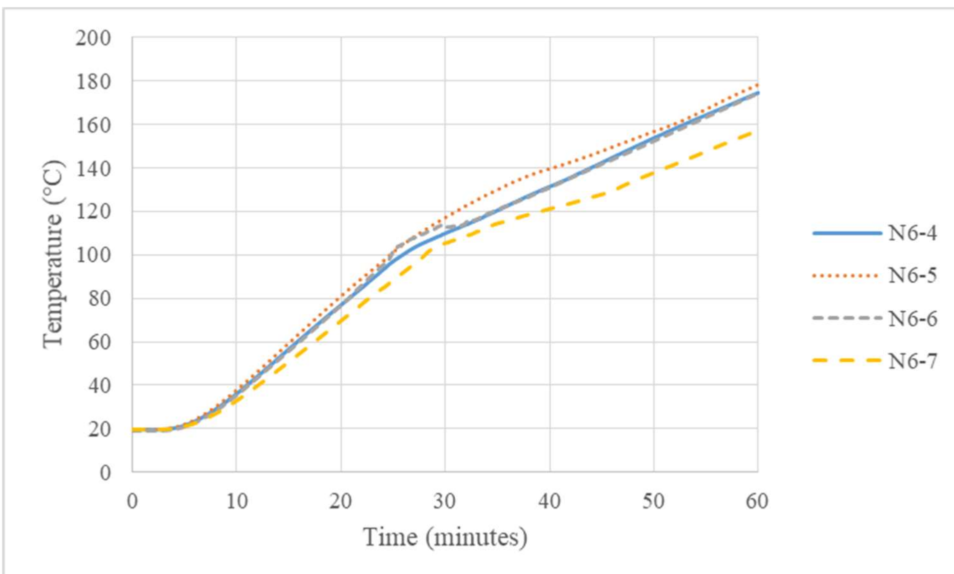

FIGURE 4.61: Specimen N6: Headed bar temperature histories.

Specimen N6 was tested about the rear face of the wall. Similar to all of the previous rear facing tests, cracks developed 15 minutes into the duration of the test, significant cracking and leakage occurred overall, and tiered crack formation was observed on the sides of the panel. In addition, this specimen had plastic reinforcing chairs that melted and caused spalling on the rear face. Figures 4.62 through 4.64 show the crack propagation observed during the testing.

FIGURE 4.62: Specimen N6: Formation of tiered cracking.

FIGURE 4.63: Specimen N6: Cracking and leakage towards corbel and wall interface.

FIGURE 4.64: Specimen N6: Significant moisture leakage across specimen.

4.7.10 Specimen L8 Results

Figure 4.65 shows specimen L8 (LW) tested with back side heating of the rear face of the wall, where the heating panel was 2” (0.0508 m) from the wall.

FIGURE 4.65: Testing of specimen L8.

Table 4.15 and Table 4.16 show the critical temperatures obtained from the test. Figures 4.66 and 4.67 show the temperature time histories for specimen L8.

TABLE 4.15: Critical mesh temperatures for specimen L8.

Critical Mesh Temperatures (°C)					
Time	L8-0	L8-1	L8-2	L8-3	Average
6 min	20	20	20	20	20
13 min	29	31	33	29	31

TABLE 4.16: Critical bent bar temperatures for specimen L8.

Critical Bent Bar Temperatures (°C)					
Time	L8-4	L8-5	L8-6	L8-7	Average
6 min	13	20	20	22	21
13 min	13	33	29	43	35

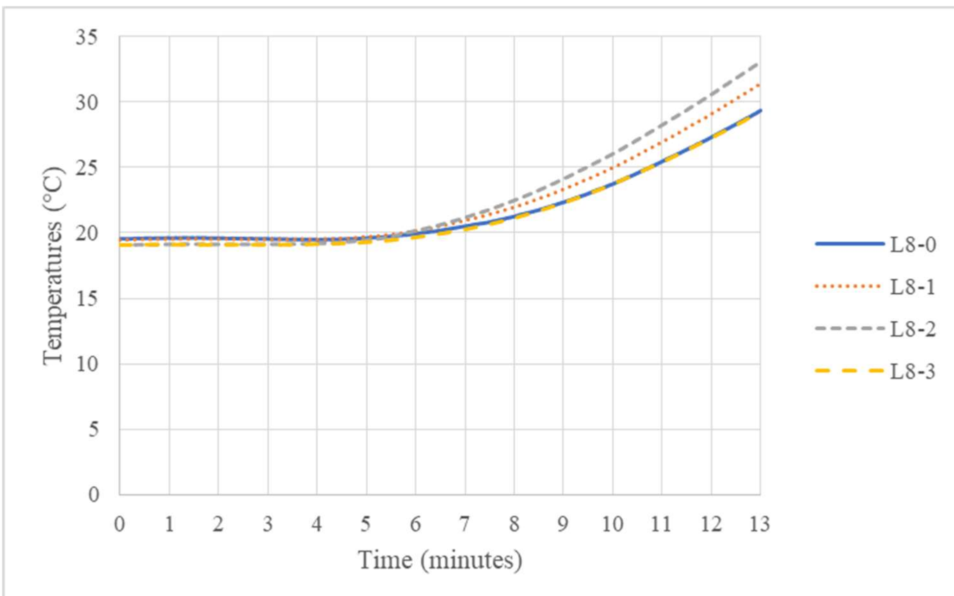

FIGURE 4.66: Specimen L8: Reinforcement mesh temperature histories.

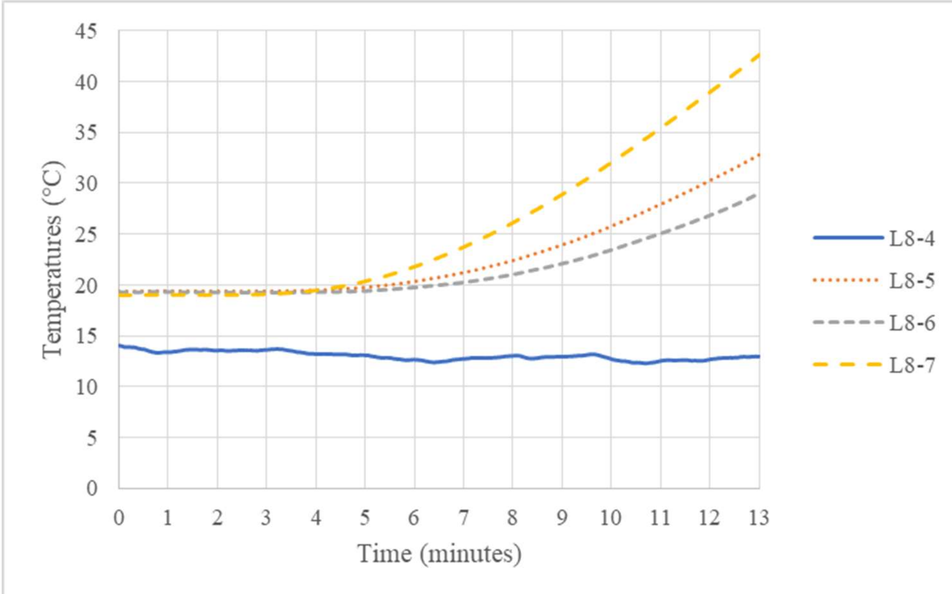

FIGURE 4.67: Specimen L8: Bent bar temperature histories.

As mentioned in Section 4.2.4, the relative humidity of specimens 7-12 was approximately 95%. However, specimen L8 was not tested for the full hour duration similar to the previous 6 NW specimens. Specimen L8 experienced spalling shortly into the duration of the test. The spalling began about 5 minutes into the test and by 13 minutes was too severe, so the test was stopped in order to protect the Raymax 2030 panels from being damaged. Figure 4.68 shows the explosive spalling observed from the test.

FIGURE 4.68: Spalling damage of specimen L8.

4.7.11 Specimen L10 Results

Figure 4.69 shows specimen L10 (LW) tested with back side heating of the rear face of the wall, where the heating panel was 2” (0.0508 m) from the wall.

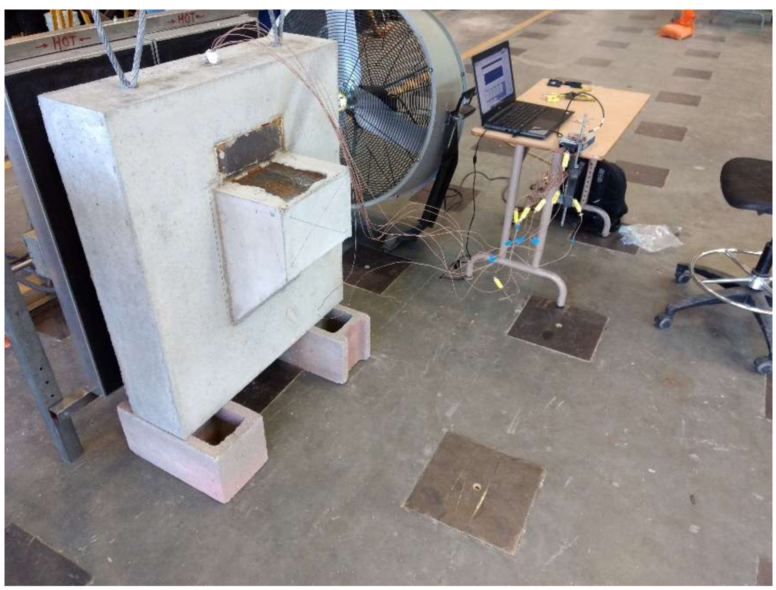

FIGURE 4.69: Testing of specimen L10.

Table 4.17 and Table 4.18 show the critical temperatures obtained from the test. Figures 4.70 and 4.71 show the temperature time histories for specimen L10.

TABLE 4.17: Critical mesh temperatures for specimen L10.

Critical Mesh Temperatures (°C)					
Time	L10-0	L10-1	L10-2	L10-3	Average
10 min	32	35	27	29	31
20 min	69	74	56	59	64

TABLE 4.18: Critical headed bar temperatures for specimen L10.

Critical Headed Bar Temperatures (°C)					
Time	L10-4	L10-5	L10-6	L10-7	Average
10 min	25	24	24	26	25
20 min	47	44	45	49	46

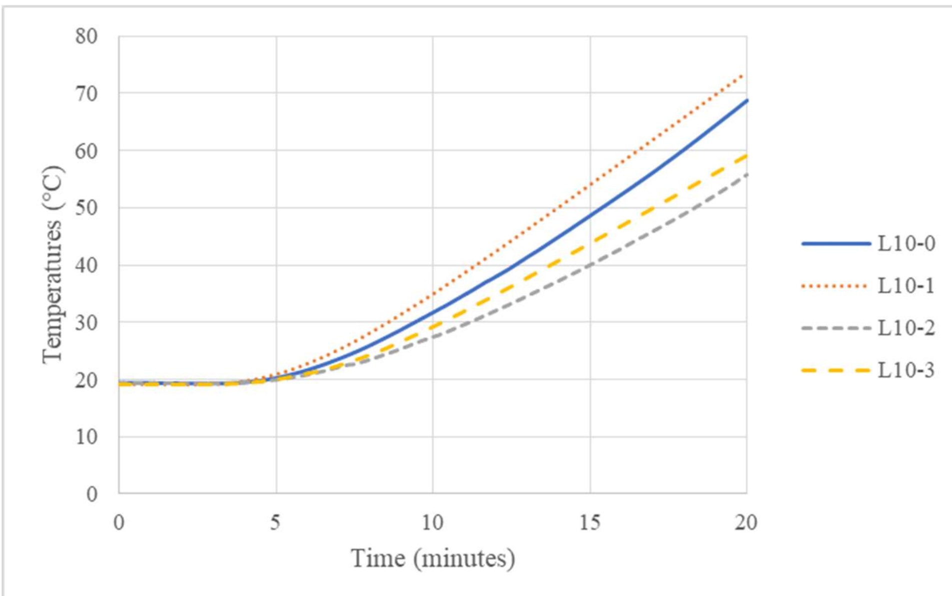

FIGURE 4.70: Specimen L10: Reinforcement mesh temperature histories.

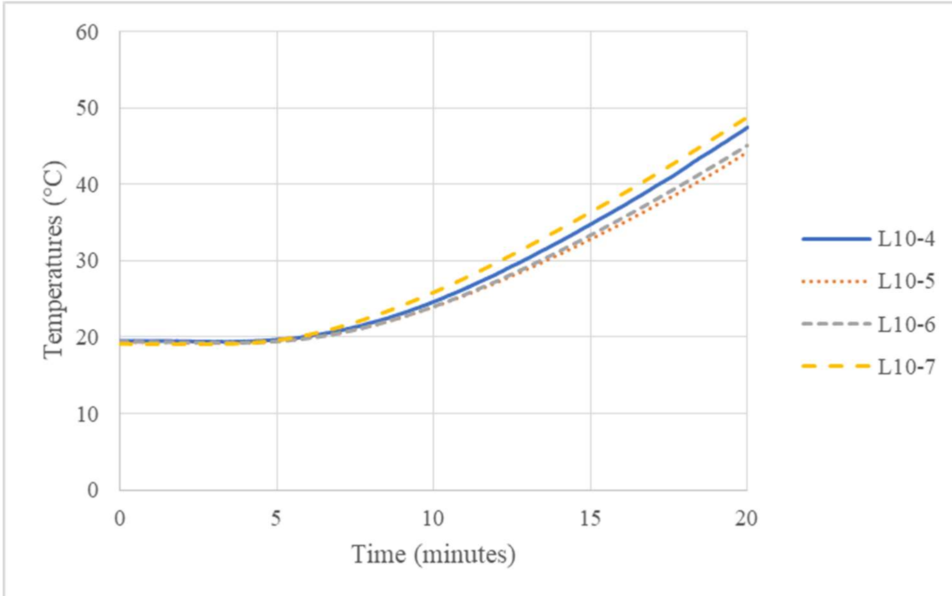

FIGURE 4.71: Specimen L10: Headed bar temperature histories.

Similar to specimen L8, specimen L10 exhibited spalling on the rear face of the wall. The spalling began about 3 to 5 minutes into the testing duration and continued to increase in frequency and magnitude as the test continued. As with the previous test, at about 20 minutes, the panels were turned off and the test was interrupted in order to protect the panels. However, the spalling that occurred from both tests left several holes punctured in the ceramic face of the heating panels. The damage can be seen in the white discolorations in Figure 4.73.

FIGURE 4.72: Spalling damage of specimen L10.

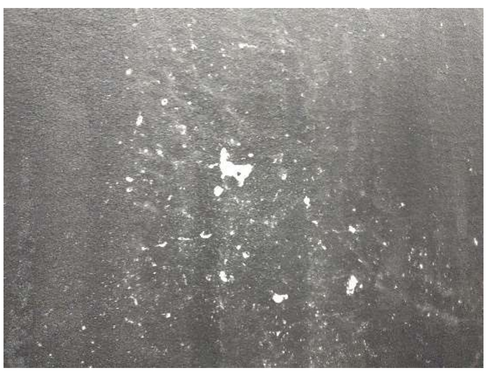

FIGURE 4.73: Raymax 2030 panel damage from spalling.

4.8 Discussion

4.8.1 Front Face Heating

Both specimen N1 and N4 were tested about the front face of the wall and internal corbel temperatures were acquired in both. In each specimen, thermocouples 4 and 5 were located at the base of the headed anchor bar and thermocouples 6 and 7 were located at the bottom of the angled plate (refer to Figures 4.18 and 4.21). However, in both specimens N1 and N4 location 7 had a malfunctioning thermocouple. Similarly, specimens N1 and

N4 both acquired front reinforcing mesh temperatures. Thermocouples 0, 1, 2, and 3 were placed clockwise in each corner of the mesh, refer to Figures 4.19 and 4.22. Within specimen N4, both thermocouples at location 0 and 1 provided erroneous data and will be ignored for the comparisons.

Table 4.19 summarizes the maximum temperatures recorded during testing of specimens N1 and N4. The average maximum temperature at the base of the headed bars was 179 °C. Specimen N4 experienced maximum temperatures about 38 °C higher than specimen N1. This difference in temperature is unclear as both tests proceeded in a similar fashion and the ambient temperature for both tests was the same. The average maximum temperature at the tip of the angled plate was 102 °C. For these temperatures, only two out of four thermocouples at this location were functioning correctly. It is reasonable for the temperatures at the base of the angled plate to be significantly less than the temperatures of the studs due to the location being 6 inches further inwards from the heating panels, even though both are covered by about 2 inches (0.0508 m) of concrete cover.

TABLE 4.19: Maximum temperature of specimens N1 and N4.

Front Sample Summary	Mesh				Headed bars		Base of Plate	
	0	1	2	3	4	5	6	7
N1	78	81	82	87	162	149	105	NA
N4	NA	98	83	72	219	209	99	NA
TC average	78	90	83	80	191	179	102	NA
Location average	83				185		102	

The average maximum temperature within the front reinforcing mesh of the wall was 83 °C. It also understandable for the average front mesh temperatures to be less than the temperatures within the corbel as the mesh locations are 10 inches (0.254 m) from the heating panels and have 2 inches (0.0508 m) of concrete cover.

Tables 4.20 and 4.21 and Figures 4.74 and 4.75 show the average interior corbel temperatures across both specimens N1 and N4 over the entire duration of testing. After 30 minutes the temperatures in N1 and N4 begin to diverge. Figure 4.74 shows an inflection point around 100 °C which indicates that significant energy is contributing to the phase change of the water instead of increasing the temperature of the concrete. This observation is consistently observed throughout the tests where the temperatures reach 100 °C and higher.

TABLE 4.20: Critical corbel temperatures for locations 4 & 5.

Critical Corbel Temperatures: Locations 4 & 5 (°C)					
Time	N1-4	N1-5	N4-4	N4-5	Average
10 min	36	32	38	34	35
20 min	76	67	87	76	77
30 min	114	106	133	120	118
40 min	131	128	168	157	146
50 min	145	140	196	186	167
60 min	162	149	219	209	185

TABLE 4.21: Critical corbel temperatures for location 6.

Critical Corbel Temperatures: Location 6 (°C)			
Time	N1-6	N4-6	Average
10 min	31	29	30
20 min	50	45	48
30 min	67	61	64
40 min	80	76	78
50 min	94	90	92
60 min	105	99	102

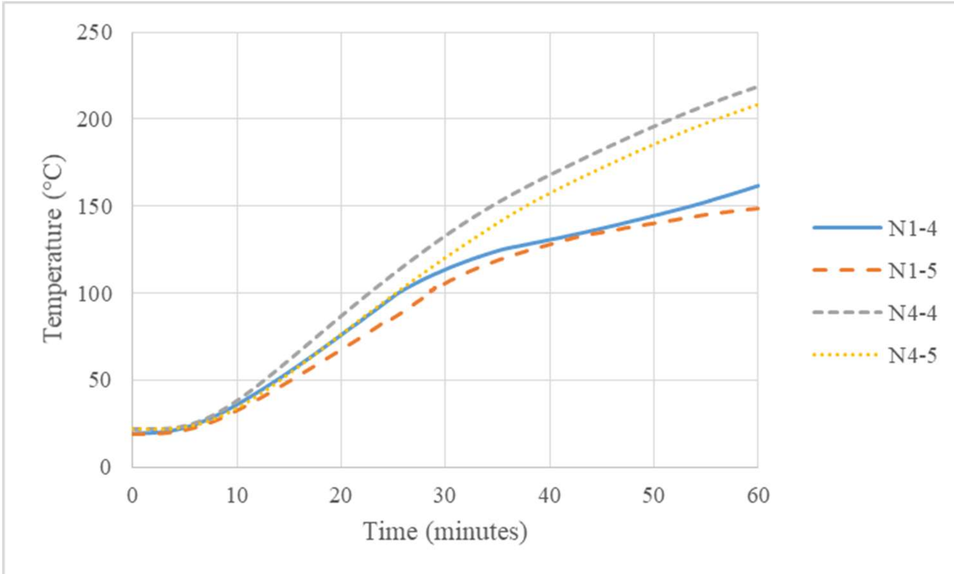

FIGURE 4.74: Time temperatures histories for corbel location 4 & 5, headed anchor.

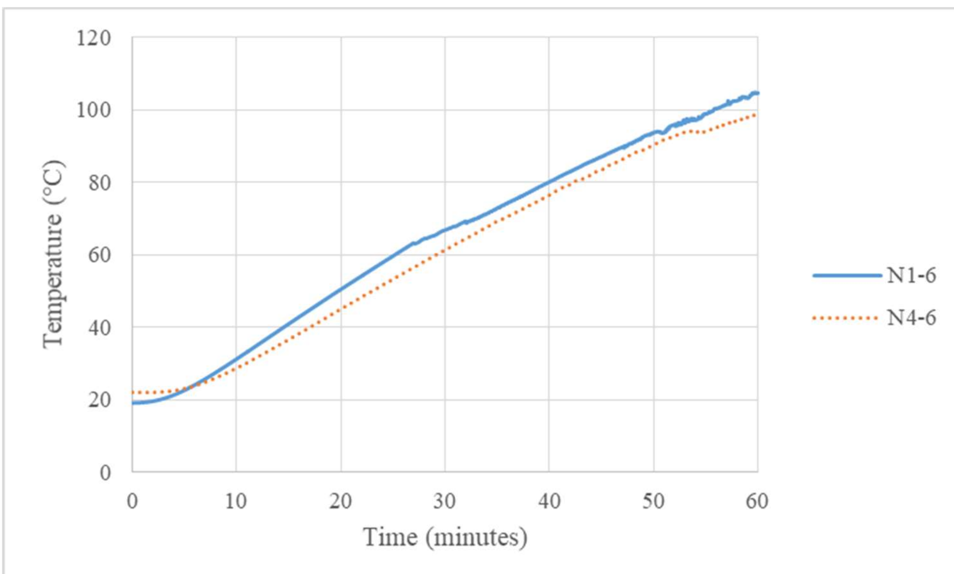

FIGURE 4.75: Time temperatures histories for corbel location 6, angled plate tip.

Similarly, Table 4.22 and Figure 4.76 show the front mesh temperatures across both specimens N1 and N4 over the entire duration of testing. Temperatures remain less than 100 °C throughout the test and each follow a similar profile.

TABLE 4.22: Critical front mesh temperatures for locations 0, 1, 2, & 3.

Critical Front Mesh Temperatures: Locations 0, 1, 2, & 3 (°C)								
Time	N1-0	N1-1	N1-2	N1-3	N4-1	N4-2	N4-3	Average
10 min	21	22	23	24	23	23	23	23
20 min	30	32	36	37	34	34	30	33
30 min	43	45	50	52	52	48	41	47
40 min	55	60	62	65	54	61	52	58
50 min	67	71	72	76	84	73	62	72
60 min	78	81	82	87	98	83	72	83

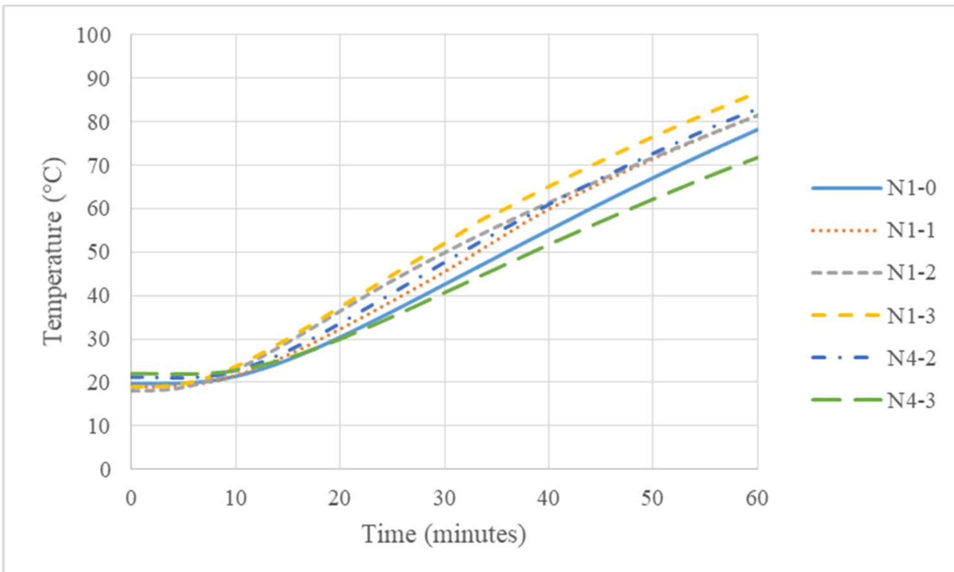

FIGURE 4.76: Time temperatures histories for front reinforcing mesh locations 0 – 3.

4.8.2 Rear Face Heating

Specimens N2, N3, N5, and N6 were headed on the rear face of the wall and temperatures were recorded for the rear reinforcing mesh, bent bars, and headed bars. Since there are 16 locations being considered for the rear reinforcing mesh, only a resulting maximum average temperature is reported. Considering the rear face specimens that provided rear reinforcing mesh temperatures, thermocouples N3-2, N5-0, N5-2, and N5-4 provided erroneous results and will likewise be ignored for the comparison and analysis.

Tables 4.23 and 4.24 summarize the maximum temperatures achieved in the specimens heated on the rear side. The average maximum temperature within the rear reinforcing mesh of the wall for all specimens was 169 °C. The temperature loss through the thickness of the wall is observed by comparing the average temperatures of bent and headed bars and reinforcing mesh. The headed bars provide the highest temperatures as they are the closest location within the specimen to the heating panel.

TABLE 4.23: Maximum temperatures of specimens N2 and N3.

Front Sample Summary	Mesh				Bent Bars			
	0	1	2	3	4	5	6	7
N2	159	138	160	172	173	134	141	NA
N3	165	180	NA	138	135	108	135	117
TC average	162	159	160	155	154	121	138	117
Location average	159				135			

TABLE 4.24: Maximum temperatures of specimens N5 and N6.

Front Sample Summary	Mesh				Headed bars			
	0	1	2	3	4	5	6	7
N5	NA	149	NA	154	172	192	189	198
N6	189	178	176	213	175	178	174	157
TC average	189	164	176	184	174	185	182	178
Location average	178				179			

Table 4.25 and Figure 4.77 show the headed bar temperatures within the rear of the wall. Most of the plots show a similar inflection point around 100 °C and the final temperatures deviate by a maximum of 65 °C.

TABLE 4.25: Critical bent bar temperatures for locations 4, 5, 6, & 7.

Critical Bent Bar Temperatures: Locations 4, 5, 6, & 7 (°C)								
Time	N2-4	N2-5	N2-6	N3-4	N3-5	N3-6	N3-7	Average
10 min	38	31	31	26	22	25	29	29
20 min	82	63	61	53	39	50	50	57
30 min	114	98	100	99	62	81	71	89
40 min	135	112	118	108	101	111	90	111
50 min	153	123	130	121	104	128	105	124
60 min	173	134	141	135	108	135	117	135

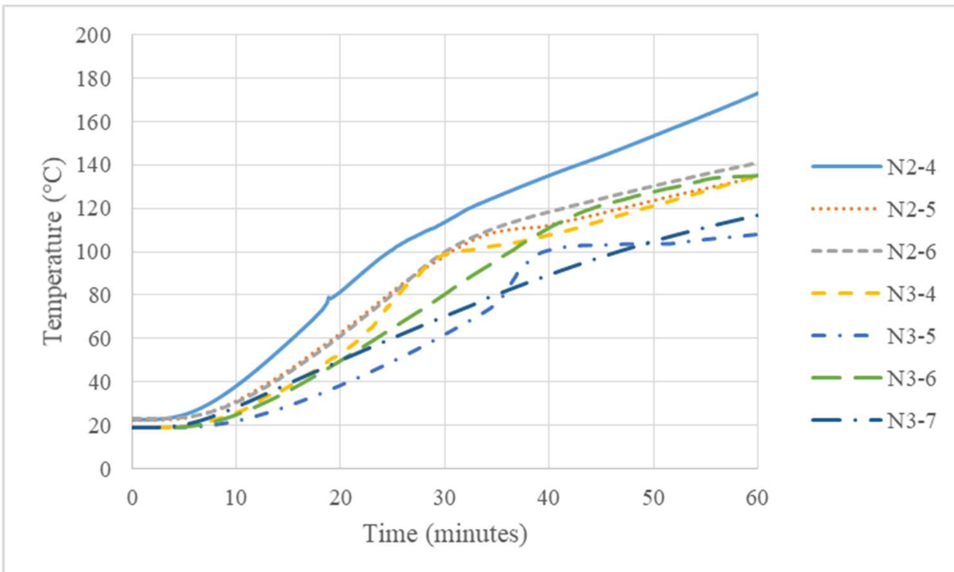

FIGURE 4.77: Time temperatures histories for bent bar locations 4 – 7.

Finally, specimens N5 and N6 provided temperatures for the headed bars. Table 4.26 and Figure 4.78 show the temperature of the headed bars within the rear of the wall. The average maximum temperature of the headed bars was 179 °C. In comparing the temperatures of the rear reinforcing mesh, bent bars, and headed bars it is observed that the bent bars experienced the lowest maximum average temperatures for the duration of the test. In addition, the maximum average temperatures of the headed bars were higher than that of the rear reinforcing mesh, which were also higher than that of the bent bars. This can be reasonably explained by the slight difference in depth between the three locations.

The locations towards the ends of the headed bars are about 1 inch closer to the rear face than the thermocouples located on the bend of the bars, refer to the full specimen designs in the Appendix. As the reinforcing mesh was not exactly set at a uniform 2 inches, the mesh in general lies between the bend of the bars and ends of the headed studs, this confirms the obtained temperature differences.

TABLE 4.26: Critical headed bar temperatures for locations 4, 5, 6, & 7.

Critical Headed Bar Temperatures: Locations 4, 5, 6, & 7 (°C)									
Time	N5-4	N5-5	N5-6	N5-7	N6-4	N6-5	N6-6	N6-7	Average
10 min	38	45	46	50	36	38	36	33	40
20 min	79	97	90	98	77	81	77	69	84
30 min	111	119	121	130	110	117	113	105	116
40 min	130	139	144	154	131	140	131	121	136
50 min	151	167	166	175	154	157	152	138	157
60 min	172	192	189	198	175	178	174	157	179

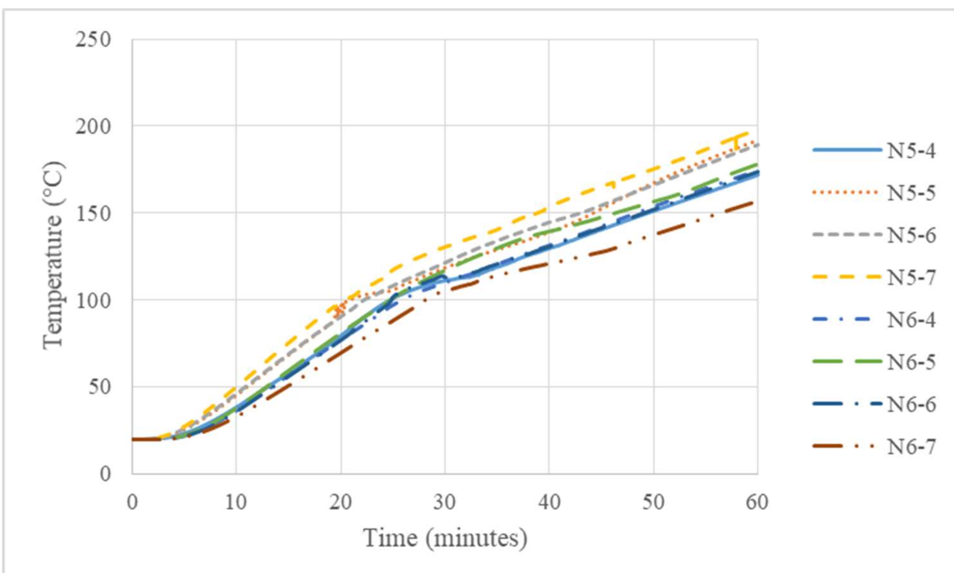

FIGURE 4.78: Time temperatures histories for headed bar locations 4 – 7.

4.8.3 Critical Visual Observations

Since the LW specimens, L8 and L10, experienced explosive spalling the resulting maximum temperatures should not be compared to the maximum temperatures experienced by specimens 1-6. However, the temperature measurements produced by the LW specimens do show similarities to the temperature measurements produced for the NW specimens. For example, all rear reinforcement mesh temperatures reach about 25 °C at 10 minutes into the test. Similarly, around 20 minutes, the rear mesh temperatures were consistently upwards of about 60 °C between both NW and LW. Similar statements can be made regarding the rear bent bar and headed bar temperatures throughout the NW and LW specimens.

The most pertinent visual observations were from the rear face heating that provided consistent tiered crack formation along the sides of the specimens. On both sides of the wall, a small crack was observed within 15 minutes of testing that eventually spread across the side of the wall, on to the front face of the wall, and then towards the wall corbel interface. These observations were seen consistently throughout the rear facing tests. Refer to Figures 4.79 through 4.84 for side by side comparisons of tiered crack formation from different tests. Another consistent observation from the experimental testing was the map crack formation on the front face of the wall. This style of crack formation was observed for specimen N2, refer to Figure 4.46.

FIGURE 4.79: (a) N2 at 30 minutes. (b) N3 at 30 minutes.

FIGURE 4.80: (a) N2 at 45 minutes. (b) N3 at 45 minutes.

FIGURE 4.81: (a) N5 at 30 minutes. (b) N6 at 30 minutes.

FIGURE 4.82: (a) N2 at 45 minutes. (b) N5 at 45 minutes.

FIGURE 4.83: Full test duration cracking and leakage, N5.

It is important to remember that the NW specimens were tested at 85% moisture content. Considering an optimal moisture content for testing, these specimens possess more water than the 50-75% preferred by ASTM E119 under Section 6.2.1. The water within the specimens likely pooled or collected around the locations of the rear reinforcing mesh and either the bent or headed bars. During the duration of the test, the heat radiated from the panel drove the moisture out of the specimen towards the sides, as seen from the previous figures. Eventually those cracks spread towards the front of the wall and ultimately on to the corbel itself. This could raise significant concern for a full-scale adjacent building fire, where corbels on the opposite side of structural columns or walls are exposed to heat from behind. As the following figures display, cracks and moisture will develop between the corbel and wall interface without originating from the tiered cracking observed on the sides of the wall. This experimental fire scenario simulated a relatively low temperature fire, 563 °C, for only a 1-hour duration. Assuming that ASTM E119 represents a comparable fire scenario, strictly concerning maximum temperatures and a full fire duration, the experimental fire scenario completed is of much smaller scale. There should be reasonable concern for concrete corbels that are not directly in a structural fire but are exposed to an external fire and therefore become susceptible to the increase in temperature, which leads to the formation of cracks and escape of moisture.

FIGURE 4.84: (a) Isolated corbel cracking. N2. (b) Isolated corbel cracking, N5.

CHAPTER 5: MODEL DEVELOPMENT AND VALIDATION

5.1 Introduction

The Abaqus finite element software package was used to develop a heat transfer model to numerically simulate the experimental tests completed during this research. This chapter discusses the development and model verification process of the heat transfer finite element model. Details of the model development include assumptions and approach, geometry, boundary conditions, loading, and analysis procedure of the model. Model validation, convergence study, and sensitivity analyses are then presented and concluding discussion of the results are included.

5.2 Model Approach and Assumptions

Abaqus/CAE was chosen for the finite element modeling and analysis based on its user-friendly GUI preprocessing, robust processing, and adaptable visual post processing of output data. Abaqus provides the capability to perform steady-state and transient heat transfer analyses, as well as both sequential and fully-coupled heat transfer-stress analyses. The model used in this research uses a transient heat transfer analysis to predict the temperature distribution in the wall specimen due to thermal loading. Future research could incorporate this transient heat transfer model into a sequential heat transfer-stress analysis to perform a structural analysis at elevated temperature.

Abaqus/CAE is organized through functional units called modules. The Part, Assembly, Property, Interaction, Load, Step, and Mesh modules are used to define the local geometry, global geometry, thermal properties, thermal boundary conditions, thermal loading, analysis procedure, and mesh size and element type, respectively for the model.

The Job module is used to define and initiate the analysis and processing and then the Visualization module is used for post-processing of results.

Abaqus operates without specific dimensions or units, therefore any system of units can be used but must remain consistent throughout all inputs and outputs. Consistent base SI units of Newtons (N), meters (m), kilograms (kg), seconds (s), and degrees Kelvin (K) were used for this model. Additional derived SI units include:

- Density: kg/m^3
- Energy (heat): J (N-m)
- Watt (rate of heat transferred): J/s
- Conductivity: W/m-K
- Specific heat: J/kg-K
- Heat flux: W/m^2
- Convection coefficient: W/m^2-K

5.2.1 Geometry

Creating Parts

Figures 5.1, 5.2, 5.3, and 5.4 show the eight 3-D, deformable, solid parts sketched and extruded in the part module of Abaqus. These parts coincide with the parts required for the given connection design including the headed bars, bent bars, steel plates, corbel haunch, and the wall. Refer to Section 4.2 and the Appendix for the design of the specimens.

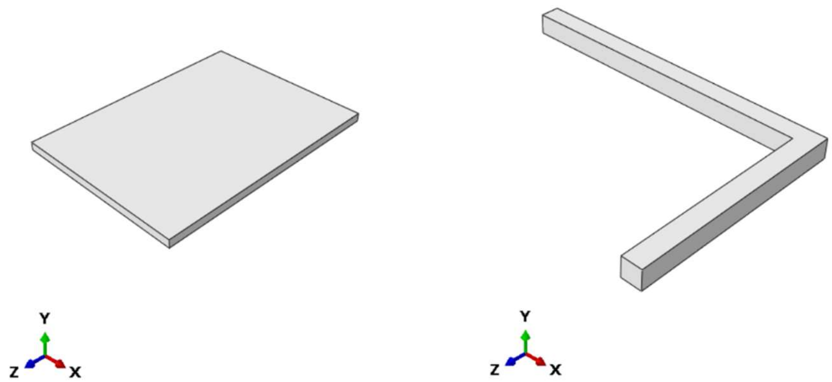

FIGURE 5.1: (a) Steel top plate part. (b) Steel bent bar part.

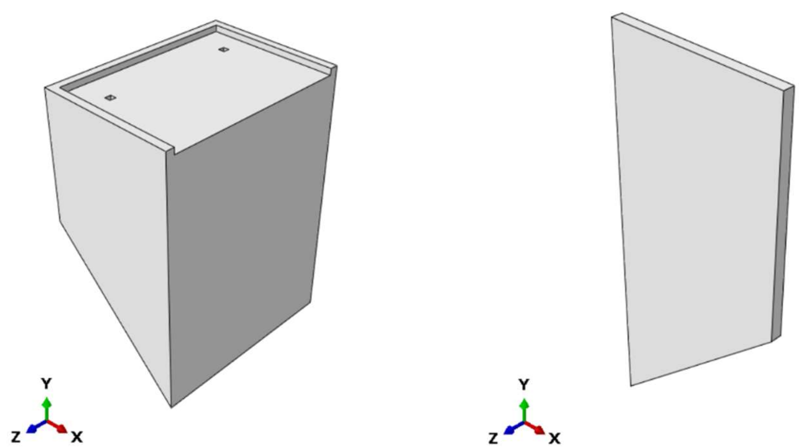

FIGURE 5.2: (a) Concrete corbel haunch part. (b) Steel angled plate part.

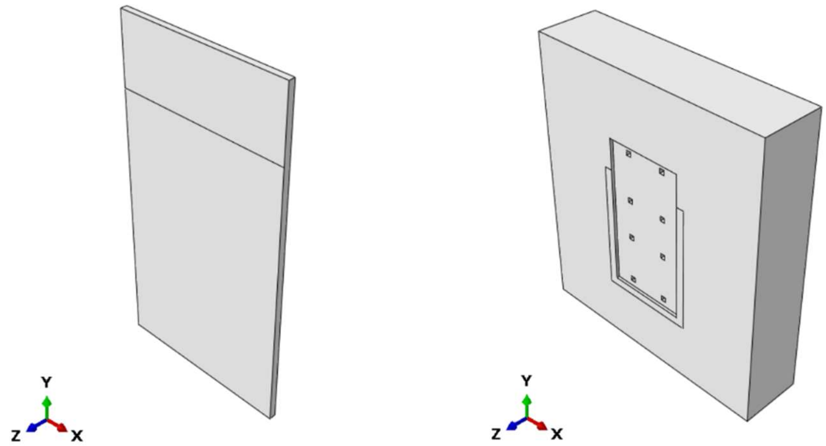

FIGURE 5.3: (a) Steel vertical plate part. (b) Concrete wall part.

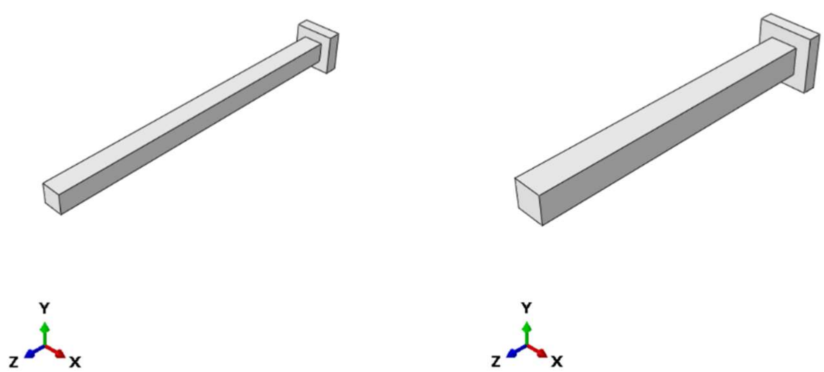

FIGURE 5.4: (a) Steel headed bar part (corbel). (b) Steel headed bar part (wall).

Assembling Parts

In the assembly module, instances of each part were used in the assembly of the entire specimen. The holes cut in the solid parts were drawn to fit the exact shape of the embedded elements to prevent element overlap. Refer to Figures 5.5 and 5.6 for the solid and wire frame assemblies within Abaqus.

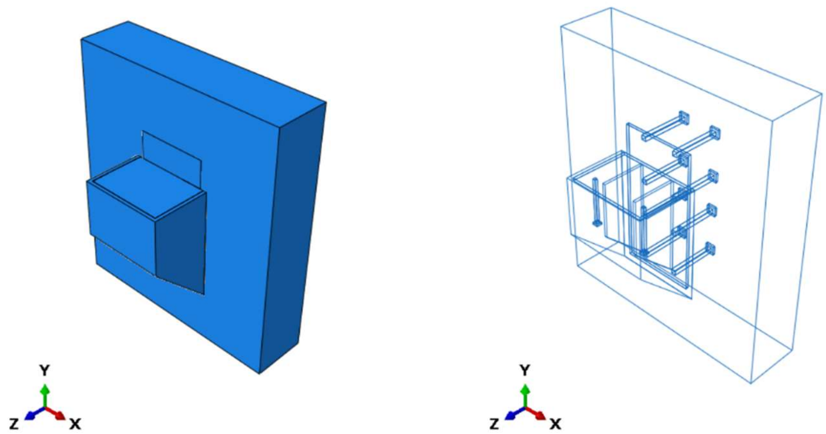

FIGURE 5.5: (a) Solid part assembly. (b) Wireframe assembly with headed bars.

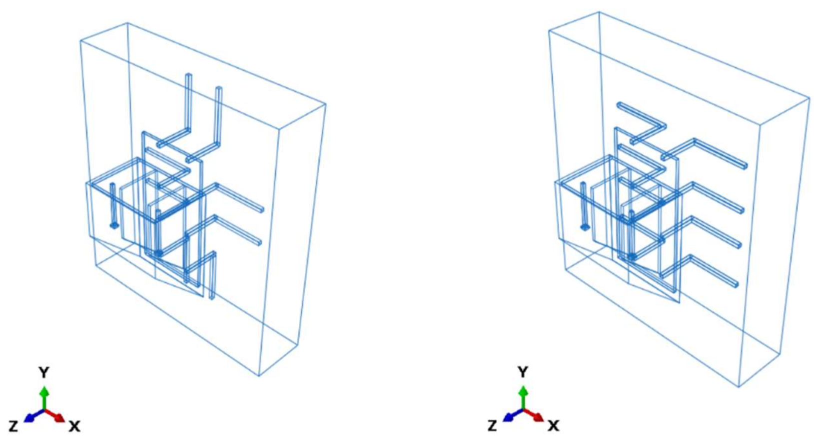

FIGURE 5.6: Wireframe bent bar assemblies: (a) NW concrete (b) LW concrete.

5.2.2 Thermal Properties

The thermal properties for the model were assigned in accordance with Eurocode 2 and 3 temperature dependent properties, as detailed in Subsections 3.5.1, 3.5.2, and 3.5.3, for the density, specific heat, and thermal conductivity of concrete and steel respectively. The equations for temperature dependent density of concrete are based on concrete at ambient temperature, taken as 2300 kg/m^3. The density of steel remains relatively constant through temperature increase and was therefore left static at 7850 kg/m^3. Figures 5.7

through 5.10 present the temperature-dependent density, specific heat, and thermal conductivity defined in the model. Additional discussion of the thermal properties is presented through a sensitivity analysis in Section 5.4.

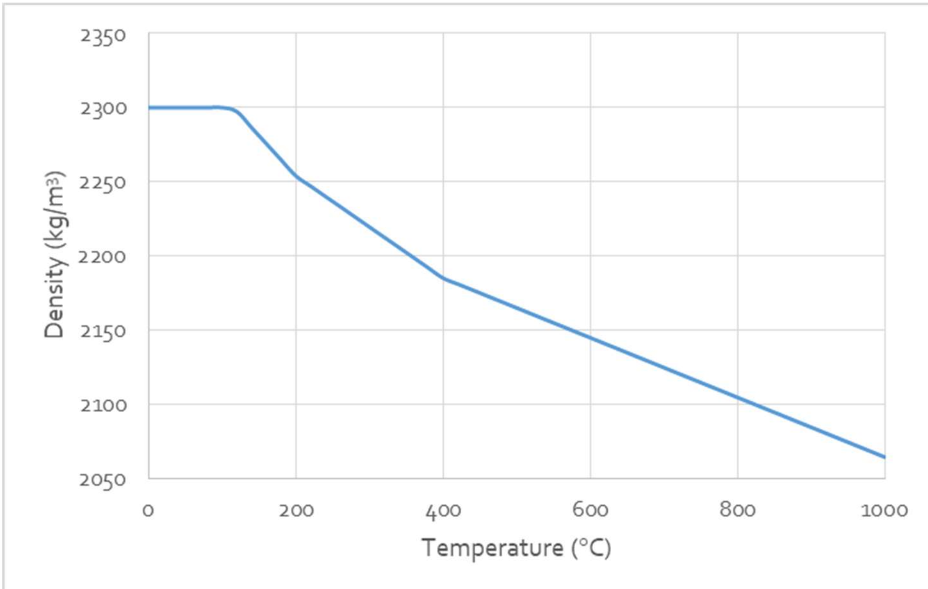

FIGURE 5.7: Modeled temperature dependent density of concrete.

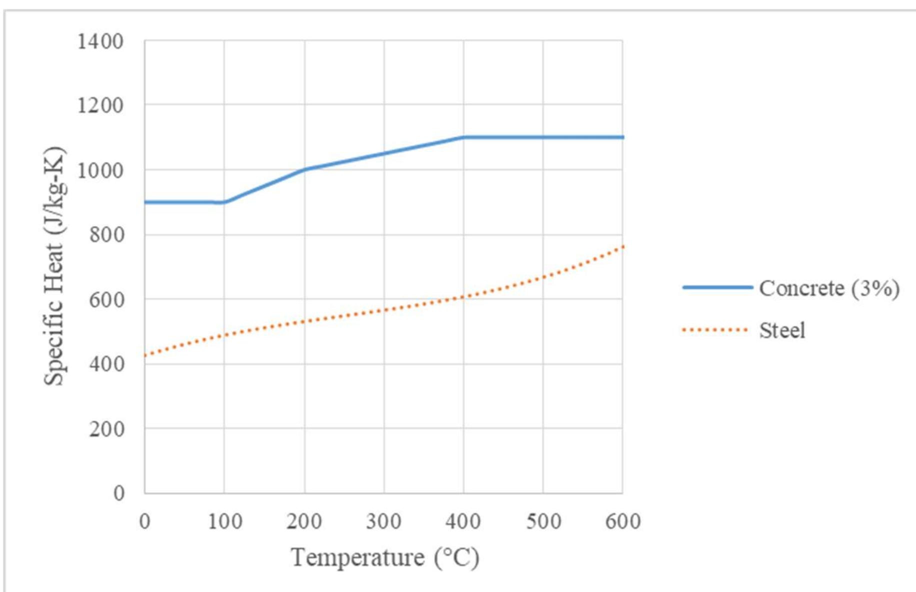

FIGURE 5.8: Modeled temperature dependent specific heat of concrete and steel.

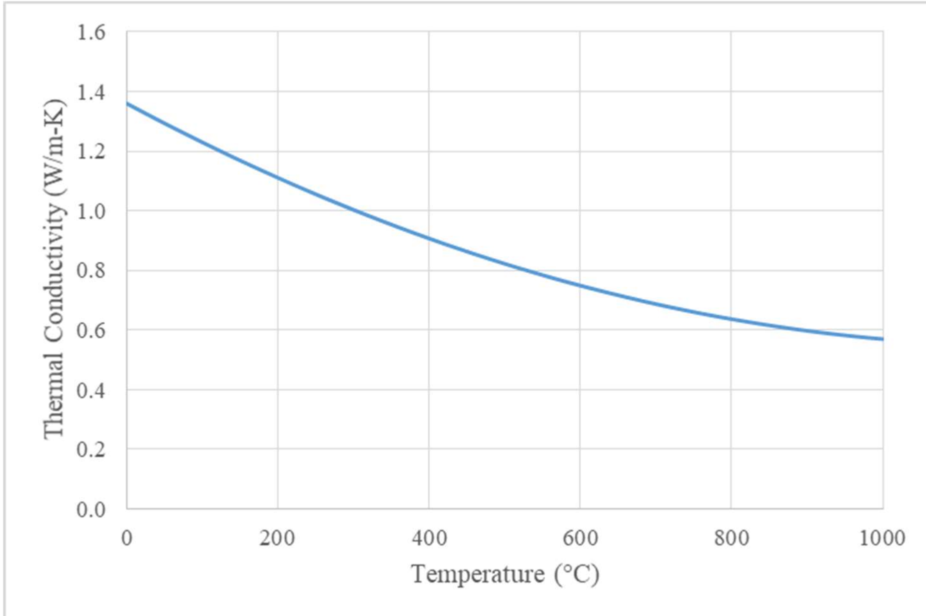

FIGURE 5.9: Modeled temperature dependent thermal conductivity of concrete.

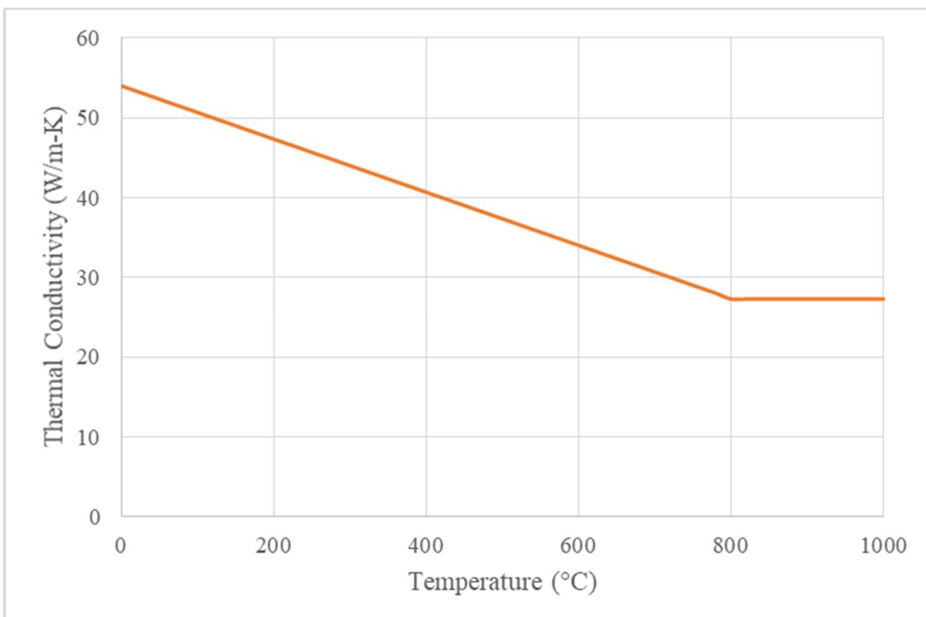

FIGURE 5.10: Modeled temperature dependent thermal conductivity of steel.

5.2.3 Interactions and Boundary Conditions

The interaction module is used to define constraints between solid parts as well as surface conditions related to thermal boundaries. The experimental specimen features plates and rebar embedded in concrete. Appropriate degrees of freedom, in this case the nodal temperatures, must be transferred between the concrete and embedded plates and rebar in the finite element model. This is done by creating tie constraints between a master and slave surface to transfer nodal temperatures between contacting faces of the parts. Close surfaces are identified through an Abaqus built-in function to find contact pairs within a small tolerance.

The interaction module also controls the thermal boundary conditions of the exterior surfaces. Thermal loads were applied to the model by specifying temperature boundary conditions on the appropriate heated surfaces based on the surface temperatures recorded during the experimental tests. Figures 5.11 shows the heated surfaces for the front face heating models. Figure 5.12 shows the heated surface in the rear face heating models. In addition, Figure 5.13 shows the applied loading of the wall and corbel surface temperatures compared to the panel temperature. Since two rear surfaces were measured, N3 and N5, the average of these two tests was applied in the model. The surface temperatures for the edge of the corbel were not applied due to the limited number of front face heating tests performed in Chapter 4 and are discussed further in Section 5.5.

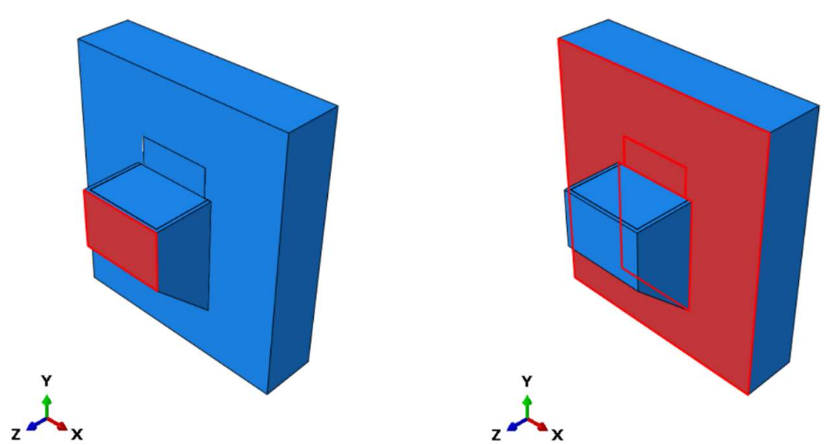

FIGURE 5.11: Heated surfaces during front face heating: (a) Corbel. (b) Wall.

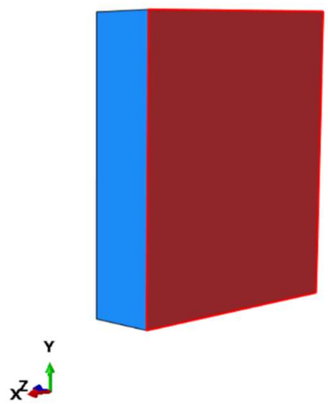

FIGURE 5.12: Rear wall surface temperatures.

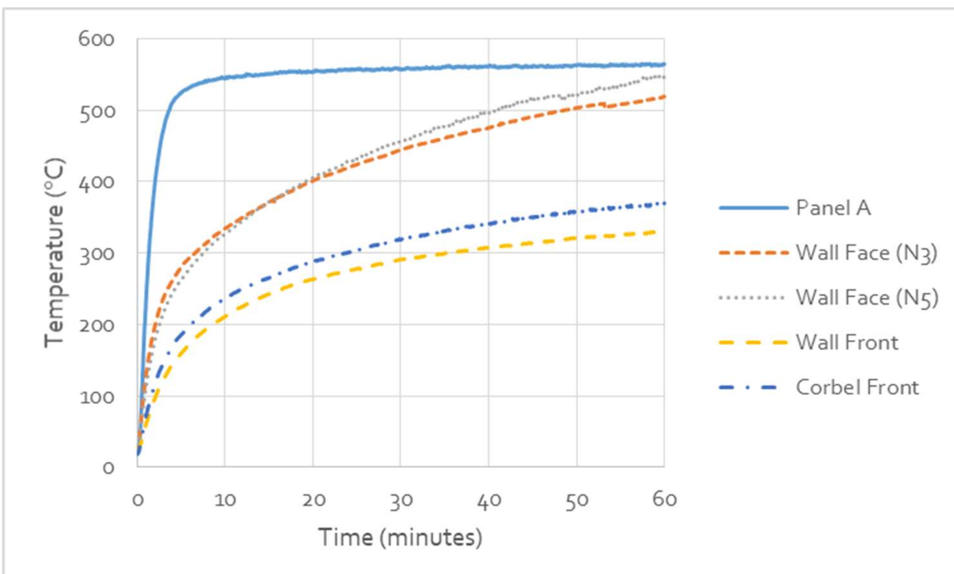

FIGURE 5.13: Applied surface load comparison.

Convection boundaries were defined on the surfaces of the wall that were not directly exposed to heat. Figures 5.14 and 5.15 show the convection boundaries applied to the unexposed surfaces of the model. For rear face heating the front face and sides of the wall and the front face and sides of the corbel were subjected to convection to ambient temperatures. For front face heating the rear face and sides of the wall were subject to convection to ambient temperatures. The film coefficient applied in Abaqus represents the convective heat transfer coefficient for the process of convection. The convection coefficient applied to the unexposed surfaces of the wall was based on Eurocode recommendations and specified as 9 W/m^2-K with ambient sink temperature of 293 K (20 °C).

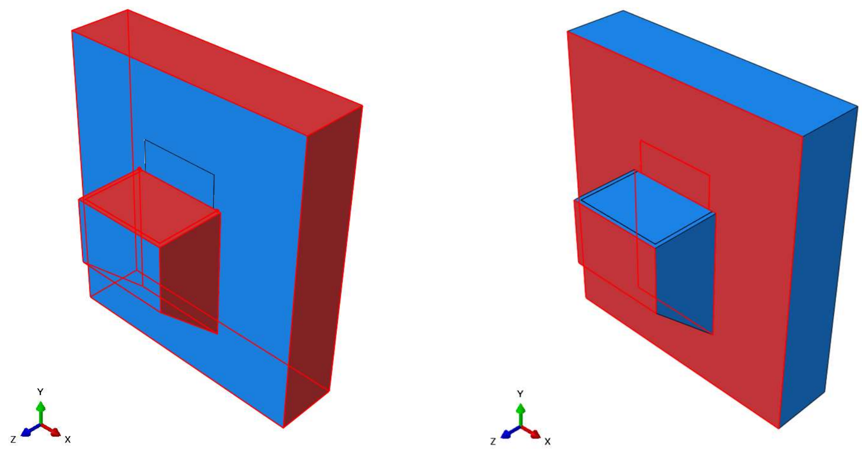

FIGURE 5.14: Rear face heating (a) Convection on unexposed side surfaces of the wall and corbel. (b) Convection on unexposed faces of the wall and corbel.

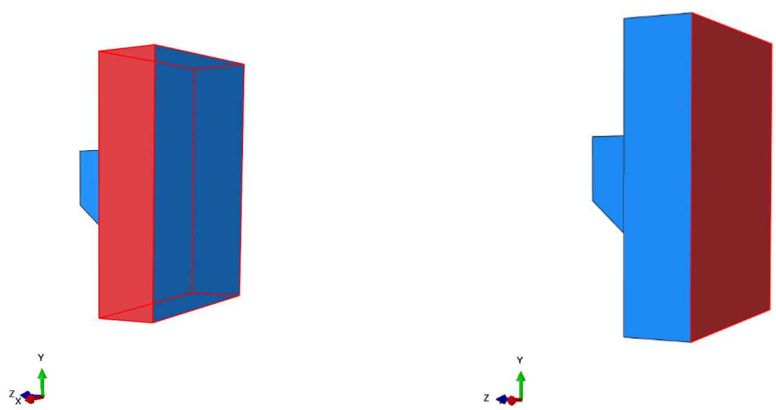

FIGURE 5.15: Front face heating (a) Convection on unexposed side surface of the wall. (b) Convection on unexposed face of the rear wall.

During front face heating, the sides and top of the corbel were not directly exposed to the heat panel as they were perpendicular to the heat source. Additionally, regrettably the surface temperatures were not recorded on the sides and top of the corbel during the front face heating test. As such, an approximation was made for these surfaces by applying convection to these surfaces to an air temperature equal to the average of the front of the corbel and the front of the wall surfaces with a convection coefficient of 9 W/m^2-K. Eurocode typically recommends a convection coefficient of 25-50 m^2-K for fire-exposed surfaces. However, fire conditions are assumed to be turbulent, and there was very little air flow during the experimental testing. Therefore the convection coefficient was held constant at 9 W/m^2-K for these surfaces as well, only varying the specified air temperature.

5.2.4 Analysis Procedure

The step module was used to simulate the fire event within Abaqus, following the 1-hour experimental test completed. In Abaqus there are two options for a heat transfer step: steady state and transient. A transient heat transfer step was selected as the heat source for the experiments exhibited varied over time with a ramping phase before it reached maximum operating temperature and the desired output was the temperature gradient over time. The increments used for each model were fixed at a step size of 360 seconds.

5.2.5 Mesh Generation

Four node, tetrahedral, linear heat transfer elements (DC3D4) were used throughout the model. Even though hexagonal element shapes are typically more accurate, the complex geometry and nature of the model design prevented the use of hexagonal elements. The model had about 87,000 total elements – 83,000 in the concrete wall and corbel and 4,000 in the embedded steel elements. This mesh was chosen based on convergence studies presented in Section 5.4, providing accurate temperatures while conserving computational effort.

5.3 Results

Results are presented for the NW concrete models depicting four different configurations of the experimental tests discussed in Chapter 4. NW specimens featured both front and rear face heating and either bent or headed rebar for each test. Since the LW specimens experienced significant spalling and were only tested for about 10 minutes each, a full LW specimen model is presented in the parametric study under Chapter 6.

Internal temperatures of the bars and mesh within the corbel were compared for model validation.

Rear Face Heating

Figure 5.16 compares the rear reinforcing mesh temperatures over the duration of the experiment with the Abaqus results for rear face heating. The experimental and Abaqus results follow a similar curvature and provide resulting maximum temperatures that are within 13 °C. However, the experimental results display an inflection point in the curve around 100 °C where the Abaqus results do not feature a change in slope.

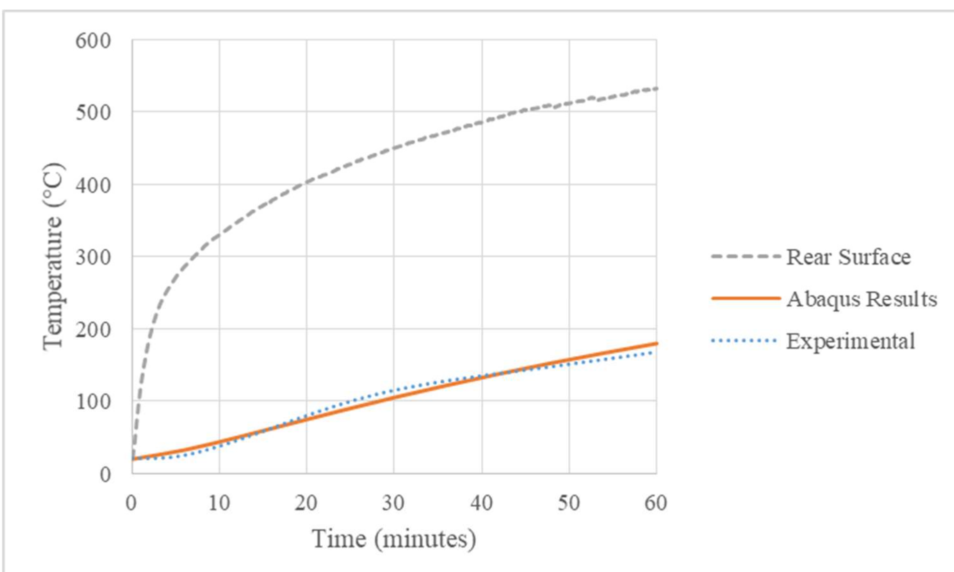

FIGURE 5.16: Rear mesh average temperature comparison.

Figure 5.17 compares the temperatures in the headed bars over the duration of the experiment with the Abaqus results of rear face heating. The rear surface temperatures of the wall are added for comparison. The Abaqus results are consistently about 50 °C higher than the experimental results obtained from Chapter 4. The Abaqus results show an inflection point around 100 °C whereas the experimental results do not feature this change in slope.

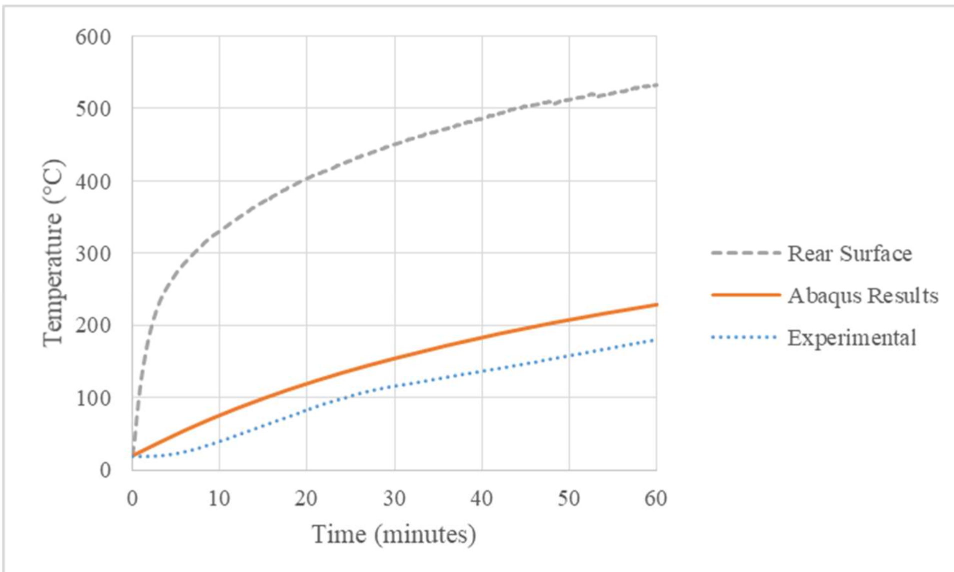

FIGURE 5.17: Headed bar average temperature comparison.

Figure 5.18 compares temperatures in the bent bars over the duration of the experiment with the Abaqus results for rear face heating. Contrary to the headed bars, the Abaqus results for the bent bars were 27 °C cooler than the experimental results over most of the duration of the test. The rear surface wall temperatures are added for comparison. The Abaqus results also feature a change in slope around 100 °C.

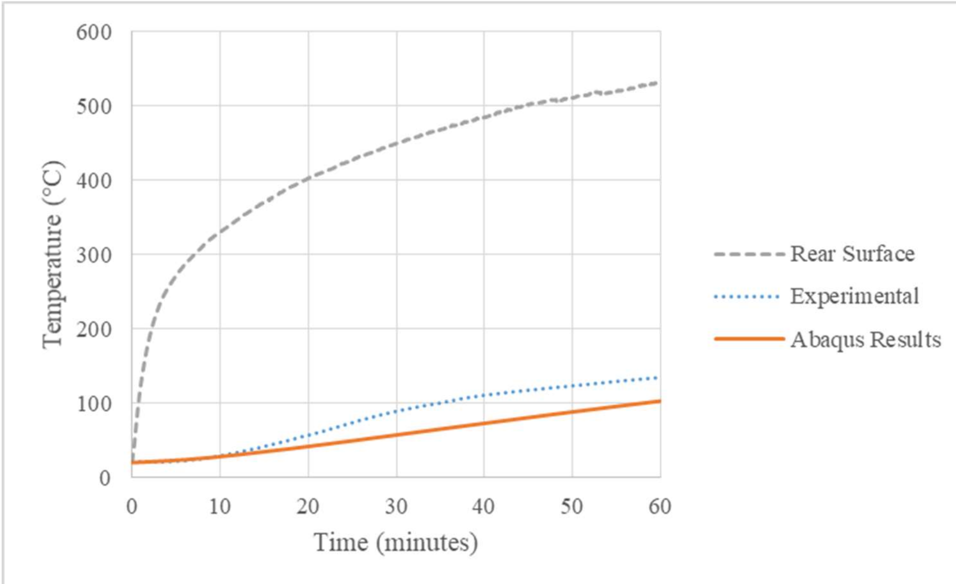

FIGURE 5.18: Bent bar average temperature comparison.

Figures 5.19, 5.20, and 5.21 show the temperature distribution for the headed bars, bent bars, and the rear mesh results. The ends of the headed bars are 1” (0.0254 m) closer to the face of the concrete than the bend of the bars. This explains the difference in maximum temperature between the two interior parts. The rear mesh results shown have 2” (0.0508 m) of concrete cover. The mesh temperatures were taken as the concrete temperatures at the corresponding node within the model. Therefore, a 3D slice of the model is shown at the embedment depth for the reinforcing mesh.

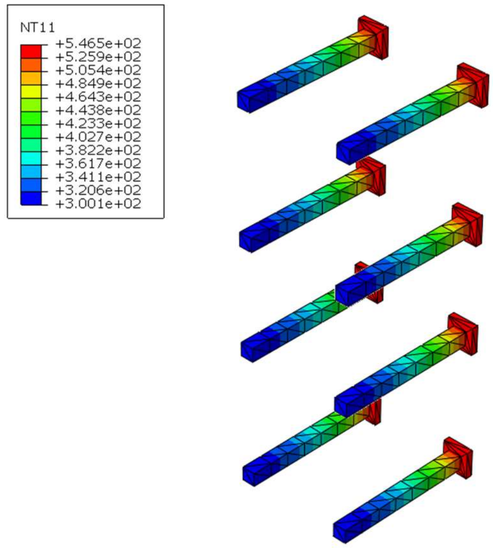

FIGURE 5.19: Interior headed bar temperatures at 1 hour (K).

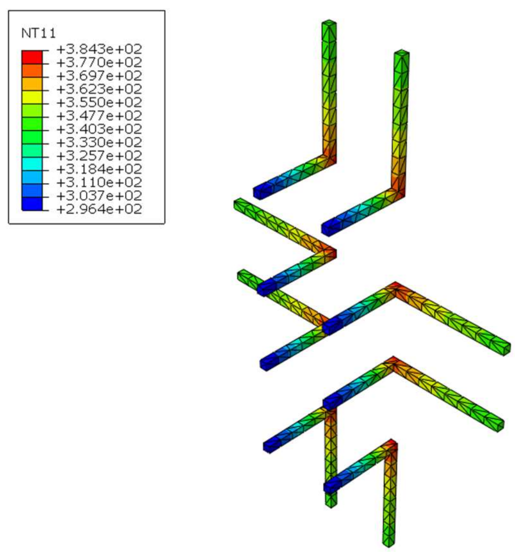

FIGURE 5.20: Interior bent bar temperatures at 1 hour (K).

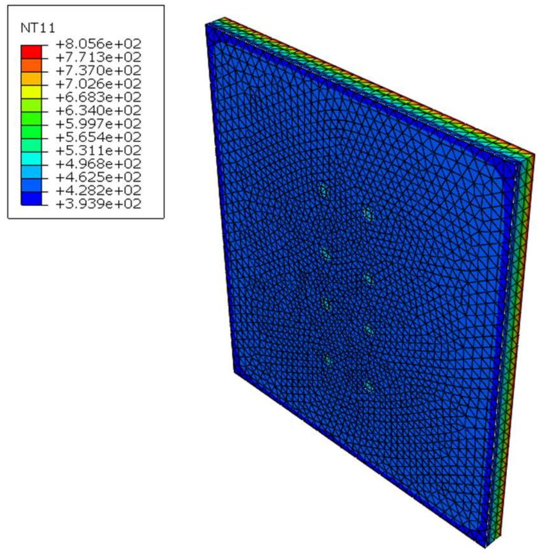

FIGURE 5.21: Rear reinforcing mesh temperatures at 1 hour (K).

Front Face Heating

Figure 5.22 shows the Abaqus results for the front reinforcing mesh temperatures compared to the experimental temperatures obtained in Chapter 4 and the front wall surface temperatures. Both curves follow a similar curvature throughout the duration of the test but the Abaqus results are about 43 °C higher than the experimental results.

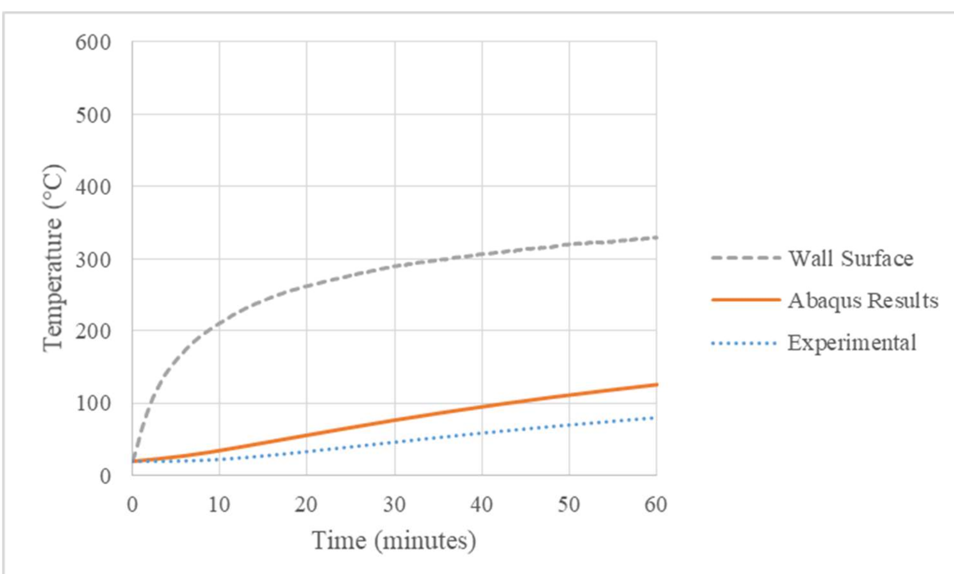

FIGURE 5.22: Front mesh average temperature comparisons.

Refer to Figures 5.23 and 5.24 for the front interior temperatures for the corbel reinforcement temperatures for front face heating. The Abaqus results for interior corbel locations 4 and 5, the headed bars, were about 58 °C less than the experimental results. The temperatures of corbel locations 6 and 7 from Abaqus closely followed the curvature of the experimental results and the resulting difference in maximum temperature was less than 10 °C.

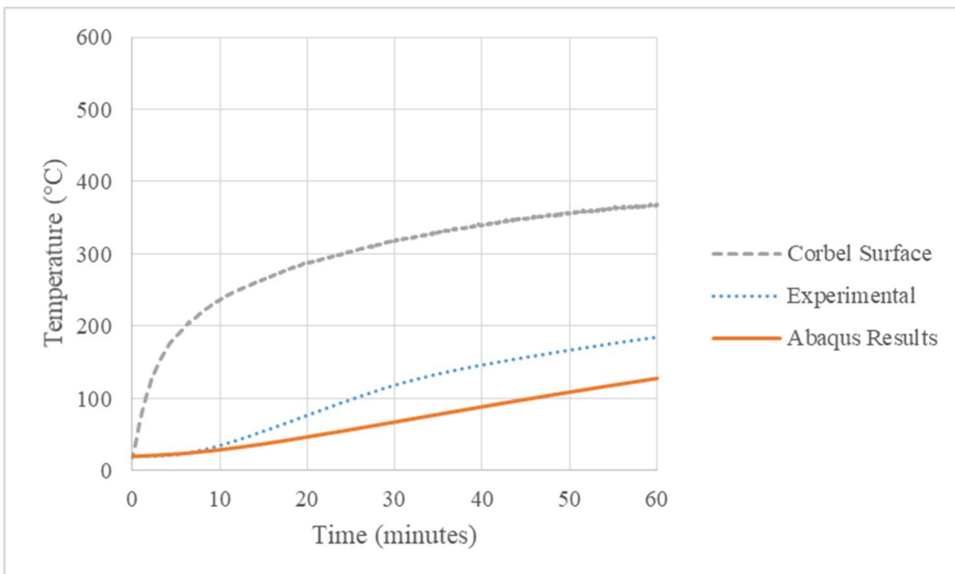

FIGURE 5.23: Corbel interior average temperature comparison, locations 4 and 5.

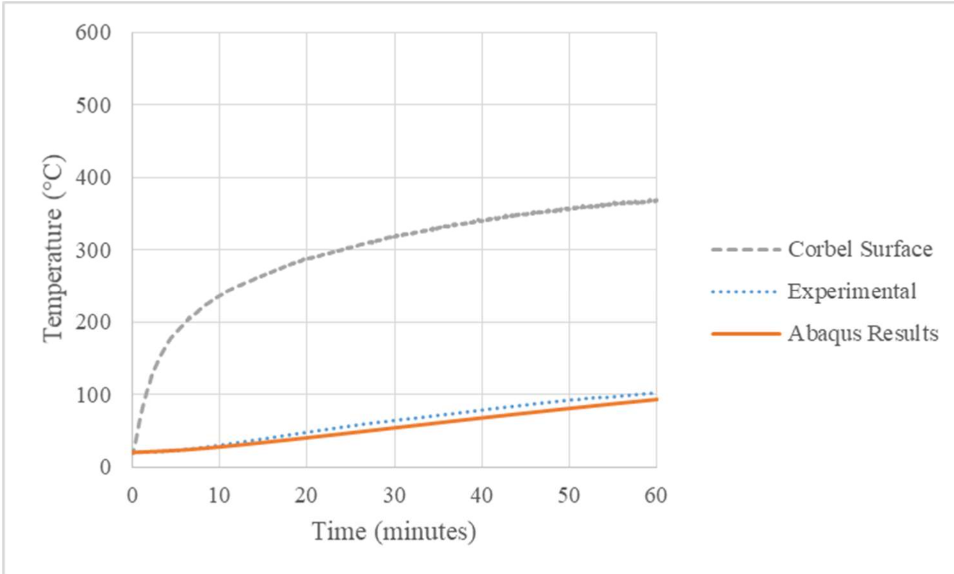

FIGURE 5.24: Corbel interior average temperature comparison, locations 6 & 7.

Finally, refer to Figures 5.25, 5.26, and 5.27 for resulting temperature distributions of the interior corbel reinforcement and front reinforcing mesh within the wall. The headed bars within the corbel feature a steep distribution from the base of the headed bars towards the top of the corbel. However, the angled plates within the corbel feature a temperature distribution with higher temperatures near the top of the angled plates and the corbel.

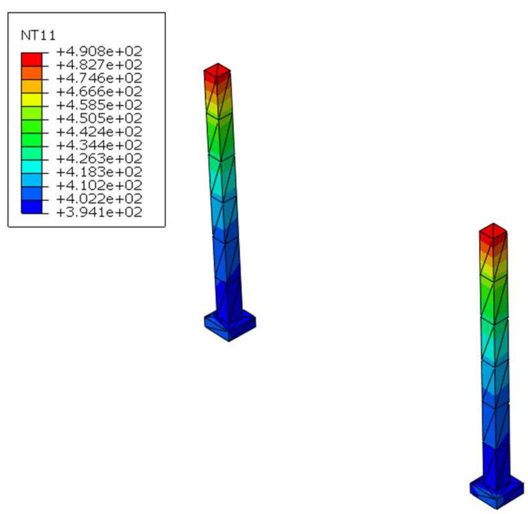

FIGURE 5.25: Interior headed bar temperatures at 1 hour (K).

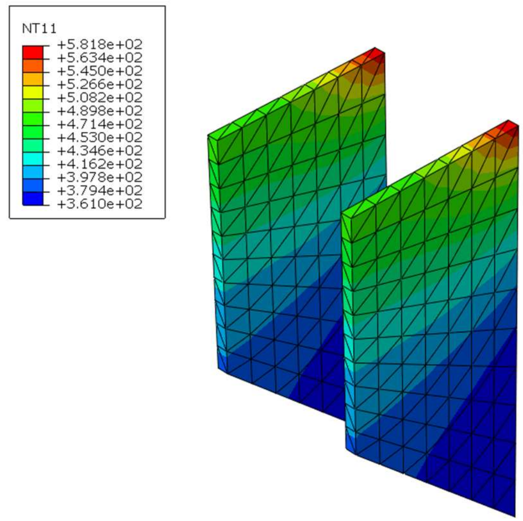

FIGURE 5.26: Interior angled plate temperatures at 1 hour (K).

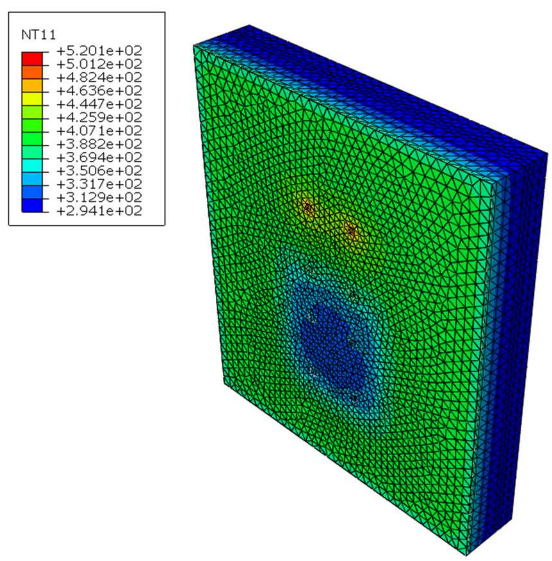

FIGURE 5.27: Front reinforcing mesh temperatures at 1 hour (K).

5.4 Convergence Study and Sensitivity Analysis

A convergence study was completed for a rear facing test, with headed rebar in the concrete wall, to determine the appropriate mesh sizes for the headed rebar and other embedded elements. Approximate mesh sizes of 6”, 5”, 4”, 3”, 2”, 1.5”, 1”, 0.75”, and 0.5” were used for the headed bars, see Figures 5.28 and 5.29.

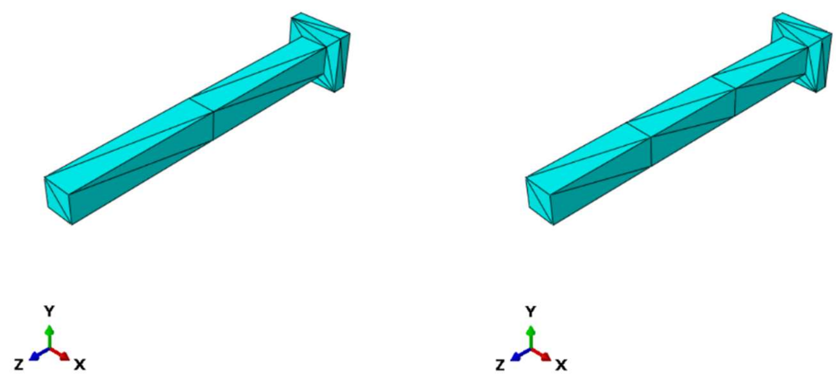

FIGURE 5.28: (a) 4” headed bar mesh size. (b) 2” headed bar mesh size.

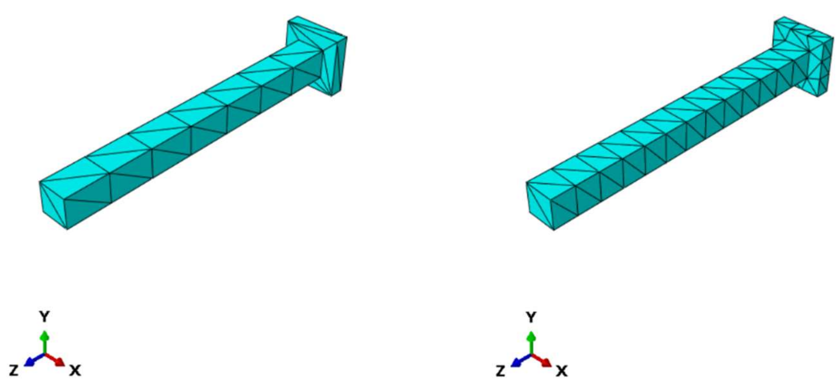

FIGURE 5.29: (a) 1” headed bar mesh size. (b) 0.5” headed bar mesh size.

Figure 5.30 shows the results for the headed bar convergence study.

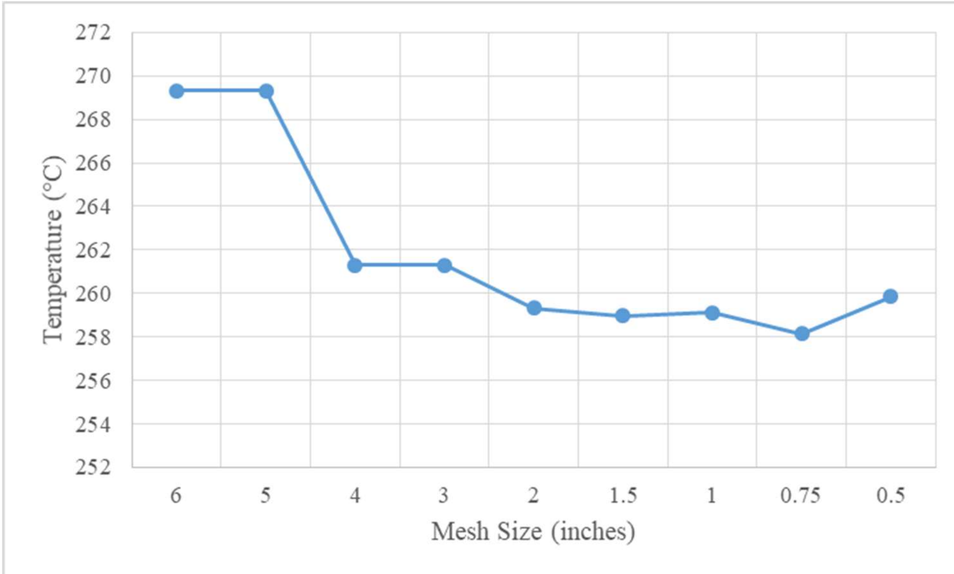

FIGURE 5.30: Headed Bar convergence study results.

The results of the convergence study for the headed bars, Figure 5.30, show that the resulting maximum temperatures begin to converge near a 2” (0.0508 m) global mesh size. For simplicity and due to limitations in the maximum number of allowable elements in Abaqus, it was determined to use an overall mesh size of 1” (0.0254 m) for the main components of the wall, the corbel, and wall solid parts. It can be observed from Figure 5.30 that mesh sizes greater than 4” (0.1016 m) for the headed bars provided inaccurate results. Therefore, the mesh size used for each embedded element within the concrete was 1” (0.0254 m).

Through the initial modeling process, a sensitivity analysis was performed to determine the effect that each property had on the analysis results. The static, non-temperature dependent, properties were either drastically lowered or raised from their simplified values. In general, changes to the material density had the least effect on the overall maximum temperatures of the model, thermal conductivity had a reasonably small effect, and specific heat had the most significant effect. From this, it was observed that specific heat was the most sensitive material property with respect to the increase in temperature.

Using a static concrete density of 1500 and 3000 kg/m^3 the overall temperatures changed by about 1 and 3%, respectively when compared to the typical density of 2300 kg/m^3. Similarly, a thermal conductivity for concrete of 0.5 and 2.0 W/m-K resulted in about 2 and 7% changes in the final maximum temperature, respectively, when compared to a typical conductivity of 0.8 to 1.4 W/m-K. Finally, specific heat values for concrete of 500 and 1500 J/kg-K provided maximum temperature changes of about 2 and 8% respectively, when compared to typical specific heat of 880 J/kg-K.

Since the properties used for the sensitivity analysis were well beyond the typical values for these thermal properties, even considering temperature dependent properties, the resulting percentage changes in the overall maximum temperatures were not significant. Therefore, the model was completed using standard temperature dependent material properties as provided by Eurocode 2 and 3 and detailed in Subsections 3.5.1 through 3.5.3.

5.5 Discussion

This section will discuss the results obtained and identify concerns inherent to the modeling process. It is clear from the results provided above that more analysis and progression of the model is required to obtain more comparable resulting temperatures.

The primary concern with the model verification process and the results obtained was the amount of moisture within the specimens. The evidence of excess moisture was observed in Chapter 4 and an example is represented again in Figure 5.31. From Table 4.2, the moisture content of the specimens during experimental testing was 85%. This is a concern because typical ASTM standards recommend 75% moisture content or less for experimental fire testing.

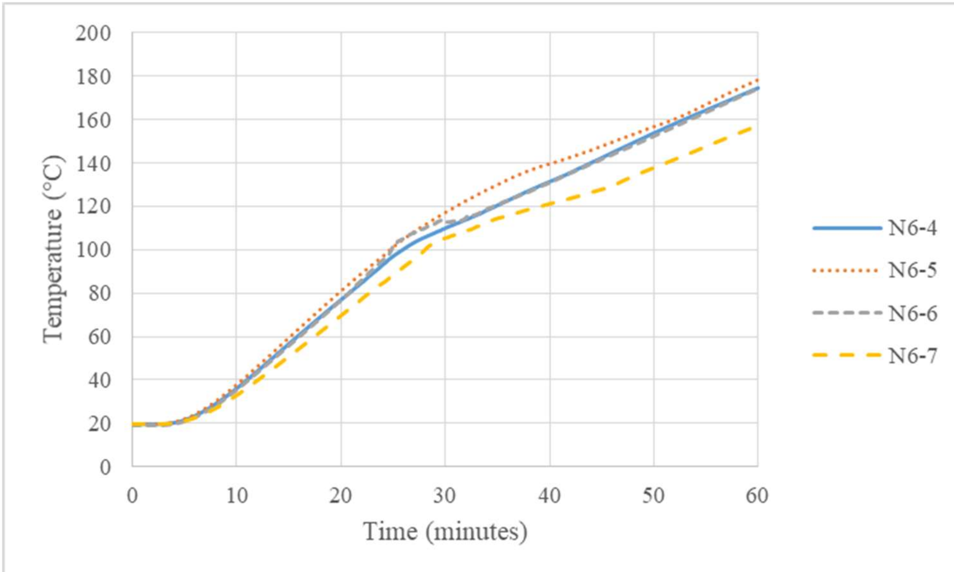

FIGURE 5.31: Headed temperature plot with inflection point around 100 °C.

Figure 5.31 shows an inflection point around 100 °C. This is likely attributed to thermal energy being absorbed by the excess moisture in the concrete to change the water from the liquid to gaseous phase at its boiling point instead of the energy being absorbed to increase the temperature of the material. The Abaqus results for the front reinforcing mesh and the headed bars within the rear of the wall were higher than the experimental results obtained from Chapter 4. The headed bars were 50 °C warmer and the front reinforcing mesh was 43 °C warmer. It is reasonable to conclude that these temperatures were increased by about 50 °C within Abaqus since the excessive moisture content could not be taken into consideration within the model. In order to effectively model this phenomenon, more correlation is required between the true amount of moisture present in the specimen and the specific heat necessary to increase the temperature of the concrete.

There are concerns with the process used to obtain the front surface temperatures. Due to the limited amount of front facing experimental tests, only the corbel and wall front surface temperatures were obtained for model validation purposes. The temperatures of the left, right, inclined, and top sides of the corbel were not measured but are critical components for a complete heat transfer analysis. In addition to these surfaces, the partitioned vertical surface above the corbel shown in Figure 5.3, representing the surface steel plate, is a critical component to understanding the appropriate heat transfer to the corbel and through the wall. However, none of these surface temperatures were able to be obtained due to the limited number of experimental tests and equipment. It is reasonable to conclude that additional thermal loading is required on these surfaces as evidenced by the lower temperatures of the interior headed bars and angled plates within the corbel. The headed bars are closest to the heating panel and were 58 °C cooler than the experimental results. However, the angled plates are closer to the body of the wall and were less than 10 °C cooler than the experimental results. This gradient shows the difference in temperatures required across the depth of the corbel to consider the full of effects of the heat transfer experienced on the front surfaces.

Additional concerns inherent to the model were related to the embedded elements. Since, Abaqus does not recognize embedded elements for heat transfer analysis, individual holes had to be extruded from the main wall and corbel parts in order for the headed and bent bar reinforcing parts to be embedded. Due to the complex nature of the geometry it was not possible to partition and extrude the area for the angled plate within the corbel, see Figure 5.32.

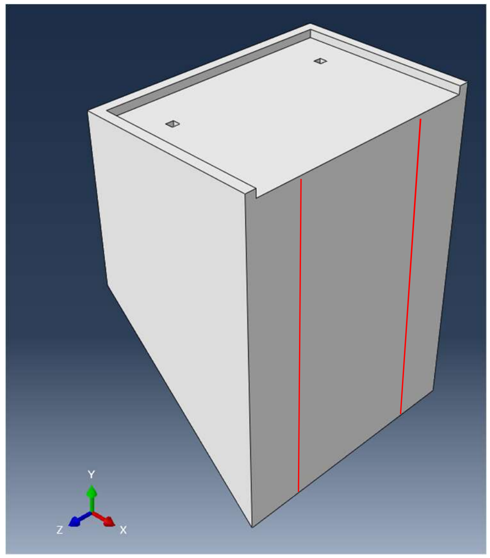

FIGURE 5.32: Corbel part lacking extruded section for angled plates.

Similarly, the portion of the bent bars after the bend could not be extruded as it caused distorted elements that prevented analysis within the model, represented in Figure 5.33.

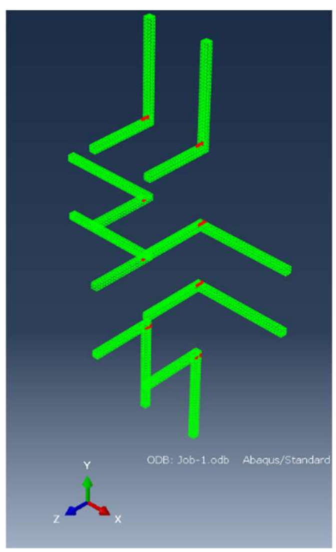

FIGURE 5.33: Distorted elements located at the bend of the bent bars.

Both of these examples caused there to be an overlap of elements within the heat transfer analysis. Figure 5.33 displays how the resulting maximum temperatures of the bent bars obtained from Abaqus could be cooler than the experimental results obtained from Chapter 4. Since there is an overlap of elements around the area of maximum temperature a heat sink effect will reduce the temperatures provided.

CHAPTER 6: PARAMETRIC STUDY

6.1 Introduction

This chapter discusses the parametric study completed for this research. The objective of the parametric study is to extrapolate the model used in the experimental tests and the validation process to encompass varying design features. Since the number of experimental tests, and therefore different configurations, were limited in the scope of this project, this parametric study was crucial to understanding the complete thermal performance of the connection. This chapter will first detail the test matrix used for the parametric study, then provide the results of each varying parameter, and conclude with a discussion.

6.2 Test Parameters

Table 6.1 shows the parametric test matrix for the finite element modeling. Parameters include concrete type (NW and LW), wall thickness, and mesh reinforcement embedment depth while maintaining continuity in the corbel design and necessary reinforcement. Since more experimental tests are required in order to effectively determine the heat transfer on the front surfaces of the specimen, the parametric study focused on rear face heating. Since the bent bars experienced element discretization errors, headed bars were used in the parametric study. For consistency, each model used in the parametric study maintained the same overall geometry, thermal boundary conditions, thermal loading, and mesh sizes determined in the validation study. In addition to the parametric study matrix, the fire event simulated in Abaqus was extrapolated to test the complete response of the specimen to a two hour fire duration.

TABLE 6.1: Parametric study test matrix.

Concrete Type	Test Direction	Wall Thickness (in)	Wall Reinforcement	Mesh Depth (in)
Original Study				
NW	Rear	8	Headed	2
NW	Rear	8	Bent	2
NW	Front	8	Headed	2
NW	Font	8	Bent	2
Parametric Study				
LW	Rear	8	Headed	2
NW	Rear	8	Headed	1
NW	Rear	10	Headed	2
NW	Rear	12	Headed	2

6.2.1 Concrete Type

The parametric study included both NW and LW concrete. As mentioned in Section 5.3, since the LW specimens experienced significant damage during the experimental testing that prevented completion of the test, a LW specimen was modeled in the parametric study through the variation of thermal properties. Figures 6.1 through 6.3 show a comparison of the NW and LW temperature dependent properties used in the model based on Eurocode 2 and 3 and described in Sections 3.5.1, 3.5.2, and 3.5.3.

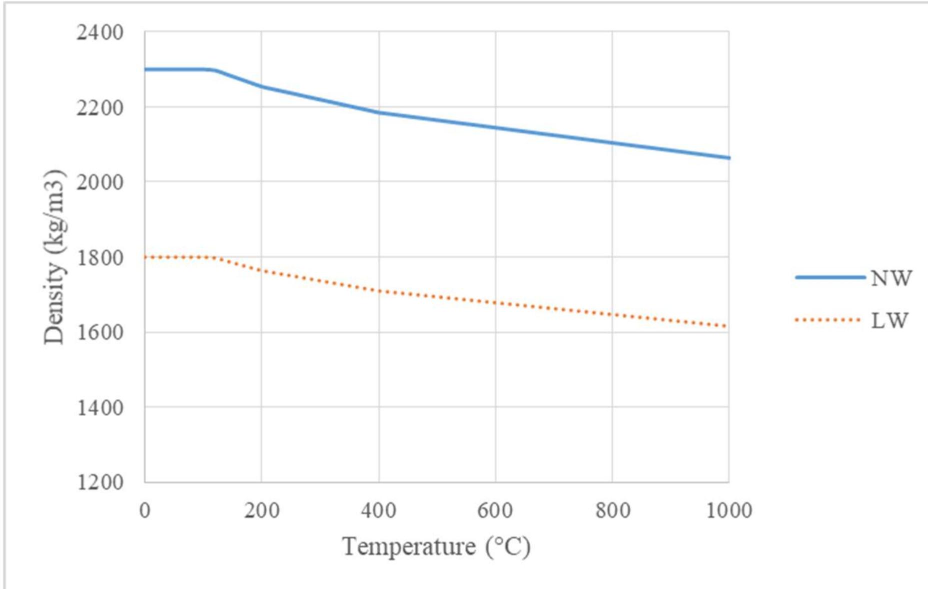

FIGURE 6.1: NW and LW temperature dependent density.

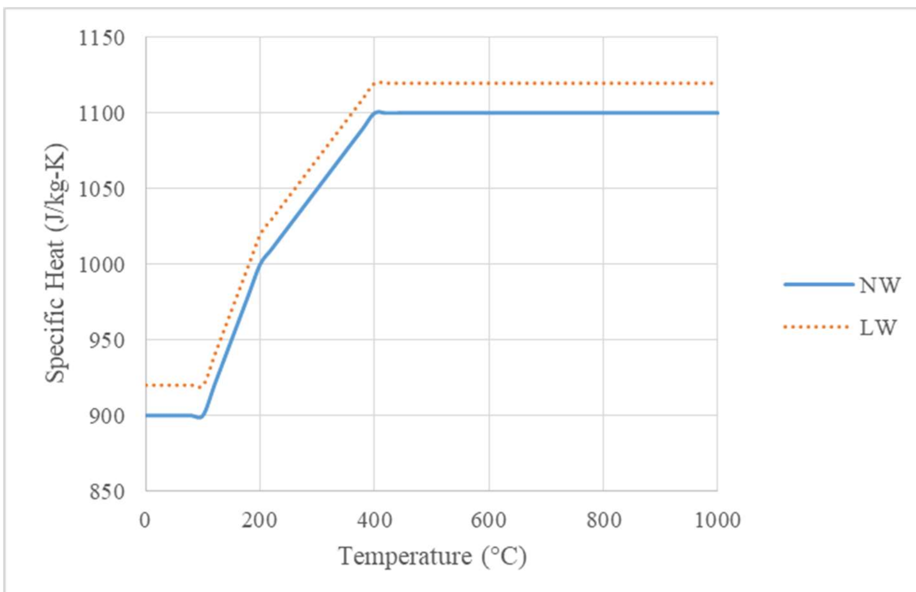

FIGURE 6.2: NW and LW temperature dependent specific heat.

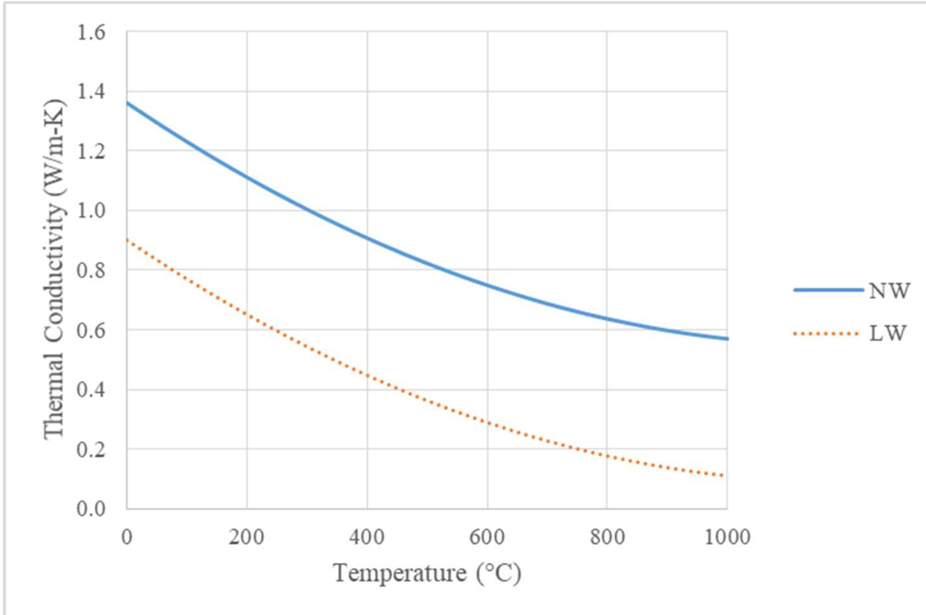

FIGURE 6.3: NW and LW temperature dependent thermal conductivity.

Figure 6.4 shows the average headed bar temperatures for the LW model compared to the NW temperatures obtained in Section 5.3.2. The temperatures applied to the rear surface are included in Figure 6.4 for comparison. Since the thermal conductivity for the LW concrete is lower and the specific heat of the LW concrete is higher than the NW concrete, it requires more energy to increase the temperatures of the specimen. The resulting maximum headed bar temperatures for the LW model were 45 °C cooler than the NW models. However, both curves followed similar profiles throughout the test.

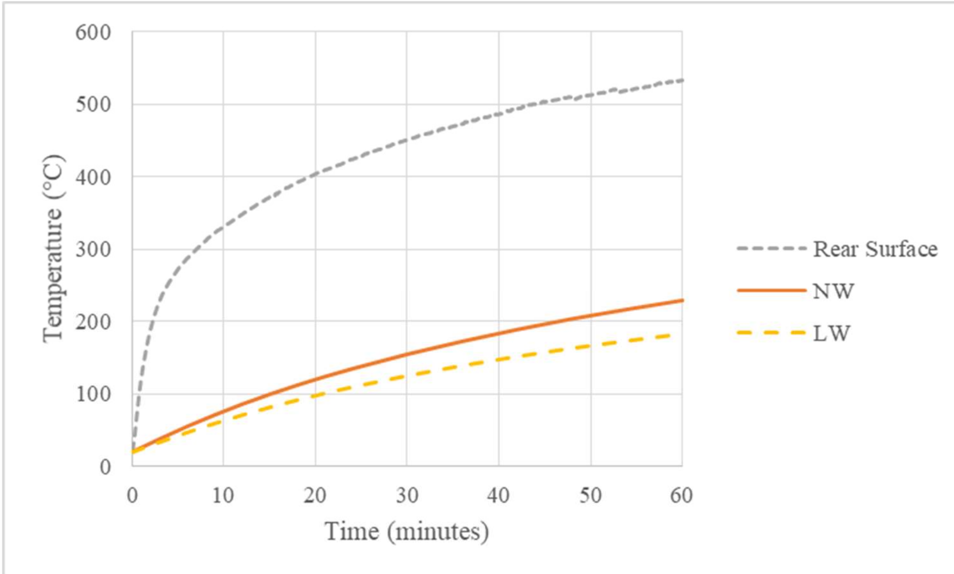

FIGURE 6.4: Headed bar average temperature comparison.

Figure 6.5 compares the average rear reinforcing mesh temperatures obtained for the LW and NW concrete models. Following similar trends to the headed bars, the resulting maximum temperatures of the mesh were about 33 °C cooler in the LW concrete model than the NW concrete model temperatures obtained in Section 5.3.2.

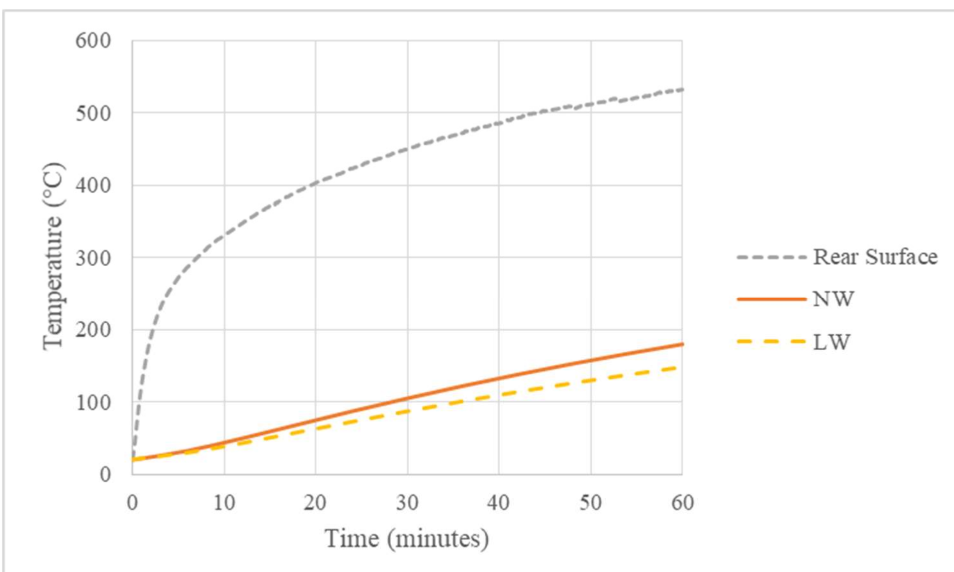

FIGURE 6.5: Rear mesh average temperature comparison.

6.2.2 Wall Thickness

The parametric study included 8”, 10”, and 12” walls for rear face heating to determine the temperatures of the headed bars and rear mesh with varying wall thicknesses. Figures 6.6 and 6.7 summarize the results obtained for the average headed bar temperatures and rear reinforcing mesh with each wall thickness. By increasing the wall thickness to 10” the maximum temperatures of the headed bars were reduced by 153 °C. The results for the 10” and 12” curves follow a similar curvature. However, by increasing the wall thickness to 12” the headed bar temperatures were reduced by an additional 43 °C. Increasing the wall thickness did not affect the maximum temperature or profile of the rear reinforcing mesh temperatures, observed by the three overlapped 8”, 10”, and 12” curves in Figure 6.7.

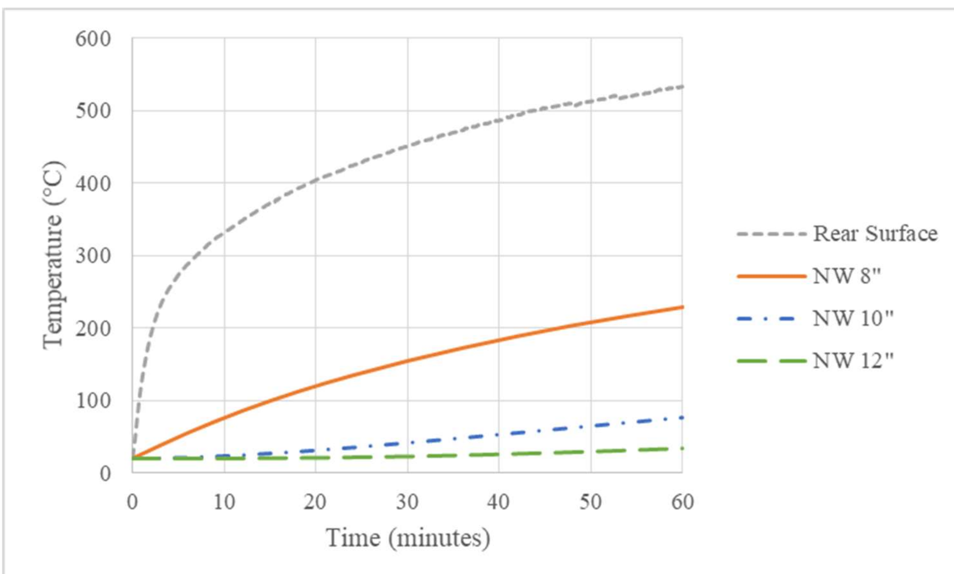

FIGURE 6.6: Headed bar average temperature comparison, varying wall thickness.

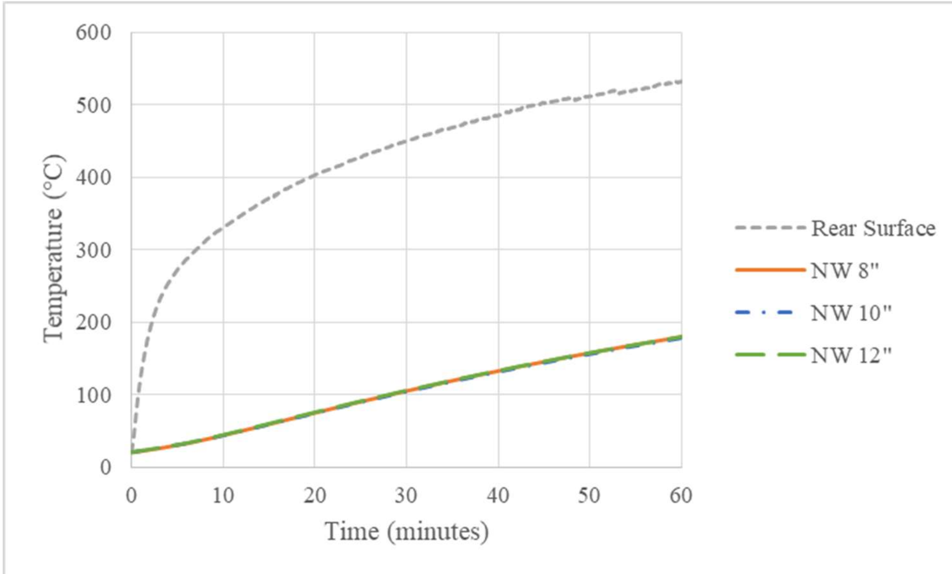

FIGURE 6.7: Rear mesh average temperature comparison, varying wall thickness.

6.2.3 Rear Mesh Embedment Depth

The parametric study also included varying reinforcement within the wall for the NW models. Figure 6.8 shows the resulting rear mesh temperatures with varying embedment depths of 1” and 2”. By decreasing the embedment depth to 1” the maximum temperatures of the rear reinforcing mesh increased by about 133 °C.

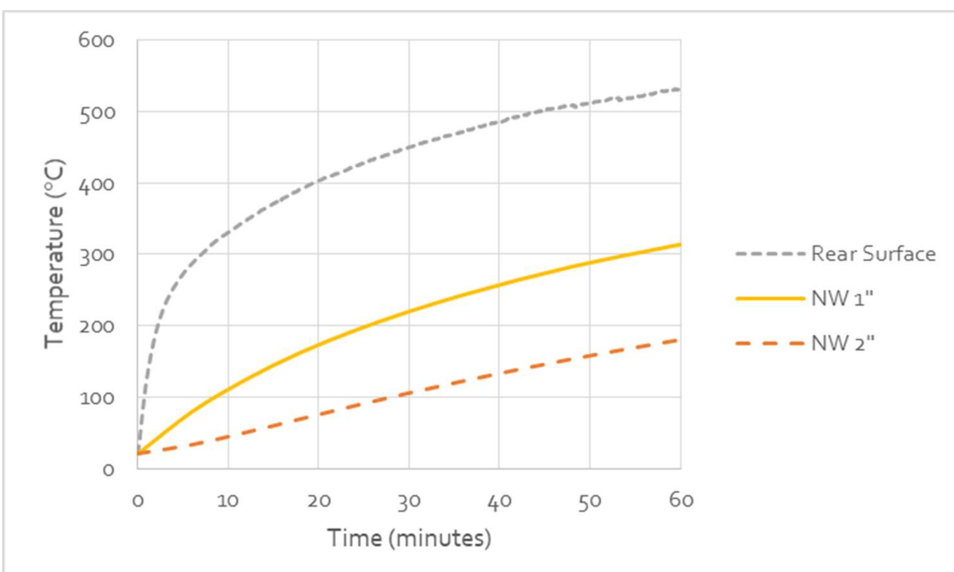

FIGURE 6.8: Rear reinforcing mesh average temperature comparison, 1” & 2” depth.

6.2.4 Test Duration

Since the temperatures reached in both Chapters 4 and 5 were relatively low with respect to realistic fire loads and temperatures expected to cause reduction in strength of the materials, the model was extrapolated to test two hours of heating from the radiant panel. The maximum panel temperature reached at 60 minutes was 532 °C. However, the manufacturer details that the maximum operating temperature of the panel is 593 °C, refer to Section 4.4. Since the panels were continuing to slowly increase during the first 60 minute testing period, the temperatures were increased linearly from 532 °C to 593 °C over an additional 60 minutes. This method provided a resulting maximum operating temperature of 593 °C at two hours. The extrapolated surface temperatures were applied as a boundary condition following similar methods as discussed in Section 5.2.3. In addition, the same convection boundaries were applied typical for rear face heating. Figures 6.9 shows the resulting temperatures for the headed bars and the rear reinforcing mesh within the wall for two hours of heating. The headed bars increased in maximum temperature by 79 °C and the rear reinforcing mesh increased by 94 °C. The rear reinforcing mesh experienced a greater increase due to its closer proximity to the heating panels. In addition, even though the maximum temperature of the panels only increased by 61 °C both the headed bars and rear reinforcing mesh experience larger temperature increases due to the increased length of exposure.

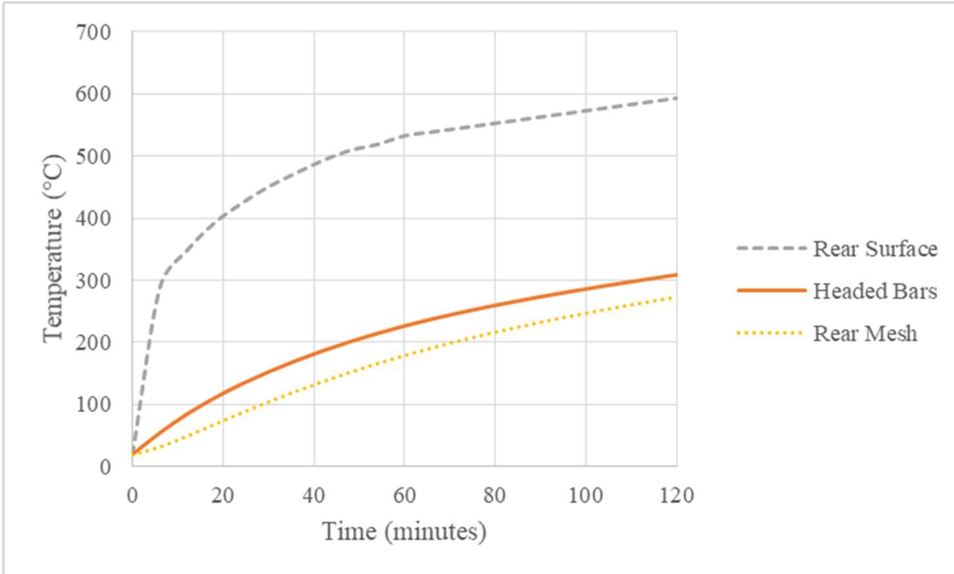

FIGURE 6.9: Headed bar and rear reinforcing mesh average temperature comparison, two hour heating.

6.3 Discussion

Considering the headed bars and rear reinforcing mesh temperatures, the parametric study showed that LW concrete has a significant impact on the interior components of the specimen, changing the temperature by at most 45 °C when exposed to 1 hour of panel heating. This is reasonable since the material properties of LW concrete require more energy to increase the temperature of the material. Other important observations and results obtained from the parametric study are with respect to increasing the thickness of the wall and changing the embedment depth of the reinforcing mesh. Figure 6.6 shows the resulting temperatures of headed bars decreasing with increasing wall thickness. The temperatures of the headed bars were reduced by 77 °C per inch for the first two inches of increasing wall thickness for the NW models. The temperatures continued to decrease by approximately 22 °C per inch for the subsequent two inch increase in thickness. The resulting temperature reductions with thickness are summarized in Table 6.2.

TABLE 6.2: Headed bar temperature reductions with increasing thickness.

Headed Bar Temperature Reductions		
Thickness (inches)	NW	°C/inch
8	229	/
10	76	77
12	33	22

Finally, the most important variation within the parametric study is with respect to the results obtained by increasing the testing duration. For reference, the headed bars increased in maximum temperature by 79 °C and the rear reinforcing mesh increased by 94 °C. The resulting maximum temperature obtained for the headed bars and rear reinforcing mesh were 308 °C and 274 °C, respectively. These maximum temperatures receive no reductions for the yield strength of steel according to Table 2.1. However, concrete at temperatures higher than 300 °C experiences a reduction to its compressive strength of 0.85 according to Table 2.2. There is greater concern when considering the actual maximum temperature of a typical fully burning fire that is past the point of flashover. The temperatures applied to the specimens in the modeling process were relatively close to flashover temperatures. However, a fully burning fire can quickly reach temperatures higher than 1000 °C. Considering that the applied loads in the model were near flashover temperatures, 600 °C, the maximum steel temperatures obtained were around 300 °C, and reductions for the yield strength of steel begin at 500 °C, there is great concern for structural strength of steel, and concrete, when left unprotected and exposed to severe fires and high temperatures.

CHAPTER 7: CONCLUSIONS AND FUTURE WORK

7.1 Conclusions

The work completed through this research includes a preliminary investigation into the effects of heat transfer for precast concrete connections during fire. This thesis provides the observations and results regarding the performance of the specimens based on the experimental testing completed and finite element analysis performed. The conclusions are as follows.

- Specimens exposed to rear facing heating, analogous to fire from an adjacent structure, experienced higher temperatures for the headed bars and reinforcing mesh of 50 °C and 13 °C, respectively; displaying the resulting gradient over the thickness of the concrete. Bent bars experienced lower temperatures by 27 °C.
- Excess moisture content significantly affected the performance of the specimens with respect to temperature increase, cracking, and moisture leakage. This performance was reflected in the inflection points of the resulting experimental internal temperature plots and the varying temperatures obtained through the model verification process.
- The exposure to heat on the rear face pushed the moisture towards the non-heated side, either the front surface or the sides of the specimen. This resulted in tiered cracking at consistent 6" vertical spacing along the sides of the specimens.
- The LW specimens contained more moisture content than the NW specimens and resulted in spalling as early as 5 minutes with explosive spalling occurring within 10 minutes.
- Decreasing the reinforcement mesh depth by 1" from 2" is projected to increase the corresponding rear mesh temperatures by 133 °C for the NW specimens. Increasing the wall thickness is projected to have no effect on the temperatures of the rear reinforcing mesh based on the results of the finite element analysis.

- Extended finite element analysis suggests that increasing the wall thickness to 10” provides headed bar reductions of 77 °C and 22 °C per inch for the NW specimens compared to a mesh depth of 2” likewise. Increasing the wall thickness to 12” provides about an additional 22 °C per inch further reduction for the headed bars.

7.2 Future Work

This thesis addresses relatively new topics that are currently under investigation and are being advanced within the field of structures in fire. As evidenced by the discussion and results provided, there is more research required in several areas pertaining to this thesis. The work presented in this thesis was not intended to provide a complete understanding of the nature of experimental fire testing of precast concrete connections. The results and conclusions provided by this thesis are intended to aid in the advancement, recognition, and implementation of performance based design for fire, for concrete connections. However, there are several directions that are suggested as evidenced by the results and content of this thesis. The recommended additional research to be completed related to this thesis is as follows:

- Further understanding is required of the relationship between relative humidity and actual moisture content. This would aid in the prediction and effective modeling of moisture content within the specimens.
- The experimental process completed in this thesis should be replicated with specimens that have a significantly increased curing times. This would result in adequate levels of moisture content. Those results should be compared to the results provided in this thesis to correlate the effects of increased moisture content. Furthermore, full scale tests should be replicated on LW specimens that do not have excessive moisture content to cause explosive spalling.
- More research is required in order to determine the appropriate boundary conditions occurring in the experimental and model verification sections of this thesis.

- It would be ideal to obtain the actual physical and thermal properties of the specimens before experimentally testing and attempting model validation; density, moisture content, thermal conductivity, and specific heat. Accurate initial properties at ambient temperatures can be used with the temperature dependent equations provided in this thesis to increase the accuracy of the model.
- More experimental testing of front face heating would provide the critical side and top surfaces of the corbel required to effectively account for the total heat flux applied to the corbel.
- Further modeling could incorporate this transient heat transfer model into a sequential heat transfer-stress analysis to perform a structural analysis at elevated temperatures.

REFERENCES

Ali, F. A., Nadjai, A., Talamona, D. and Rafi, M. M. (2007). "Fracture and Explosive Spalling of Concrete Slabs Subjected to Severe Fire." Available at: https://www.researchgate.net.

American Institute of Steel Construction, Manual of Steel Construction, 15th Edition. Chicago: AISC, 2015.

American Society of Civil Engineers – (7-16). (2016). "Minimum Design Loads and Associated Criteria for Buildings and Other Structures." Reston: ASCE, 2016.

ASTM Standard E119. (2018). "Standard Test Methods for Fire Tests of Building Construction and Materials." ASTM International, West Conshohocken, PA, 2003. DOI: 10.1520/E0119-18CE01. Available at: https://www.astm.org/.

ASTM Standard E1529. (2016). "Standard Test Methods for Determining Effects of Large Hydrocarbon Pool Fires on Structural Members and Assemblies." ASTM International, West Conshohocken, PA, 2003. DOI: 10.1520/E1529-16E01. Available at: https://www.astm.org/.

Bayreuther, Jonathan L. and Pessiki, Stephen P. (2006). "Analytical Investigation of Fire Loads for Precast Concrete Parking Structures." Available at: https://preserve.lehigh.edu.

Buchanan, Andrew H. and Abu, Anthony K. (2006). "Structural Design for Fire Safety." John Wiley & Sons, Ltd.

Emmons, H.W. (2007). "The Further History of Fire Science." Available at: https://www.tandfonline.com.

Eurocode 1 – (EN 1991-1-1). (2002). "Actions on Structures." European Committee for Standardization. London: British Standard Institution, 2002.

Eurocode 2 – (EN 1992-1-2). (2004). "Design of Concrete Structures." European Committee for Standardizations. London: British Standard Institution, 2004.

Eurocode 3 – (EN 1993-1-2). (2005). "Design of Steel Structures.". European Committee for Standardization. London: British Standard Institution, 2005.

International Building Code (2018). "2018 – International Building Code." International Code Council. Available at: https://codes.iccsafe.org.

ISO 834-11. (2014). "Fire Resistance tests – Elements of Building Construction." International Organization for Standardization. Available at: https://www.iso.org.

PCI Design Handbook, 7th Edition – (MNL-120-10). (2004). "PCI Design Handbook Precast and Prestressed Concrete." Available at: https://www.pci.org.

Qunitiere, J. G. and Veloo, P. S. (2011). "Convective Heat Transfer Coefficient in Compartment Fires." Available at: https://journals.sagepub.com.

Sadiq, H, Wong, M. B., Tashan, J., Al-Mahaidi, R., and Zhao, X. L. (2013). "Determination of Steel Emissivity for the Temperature Prediction of Structural Steel Members in Fire." Journal of Materials in Civil Engineering. Available at: https://researchbank.swinburne.edu.au.

Watlow. (1997). "Radiant Heating with Infrared – A Technical Guide to Understanding and Applying Infrared Heaters." Watlow Electric Manufacturing Company.

Wtvd, (2017). "Monstrous Fire Destroys Apartment Building in Downtown Raleigh." ABC11 Raleigh-Durham, 17 Mar. 2017. Available at: abc11.com/monstrous-fire-destroys-building-in-downtown-raleigh/1804792/.

Zhang, Chao and Usmani, Asif. (2016). "Heat Transfer Principles in Thermal Calculations of Structures in Fire." Available at: https://www.ncbi.nlm.nih.gov.

APPENDIX: STRUCTURAL DESIGN OF SPECIMENS

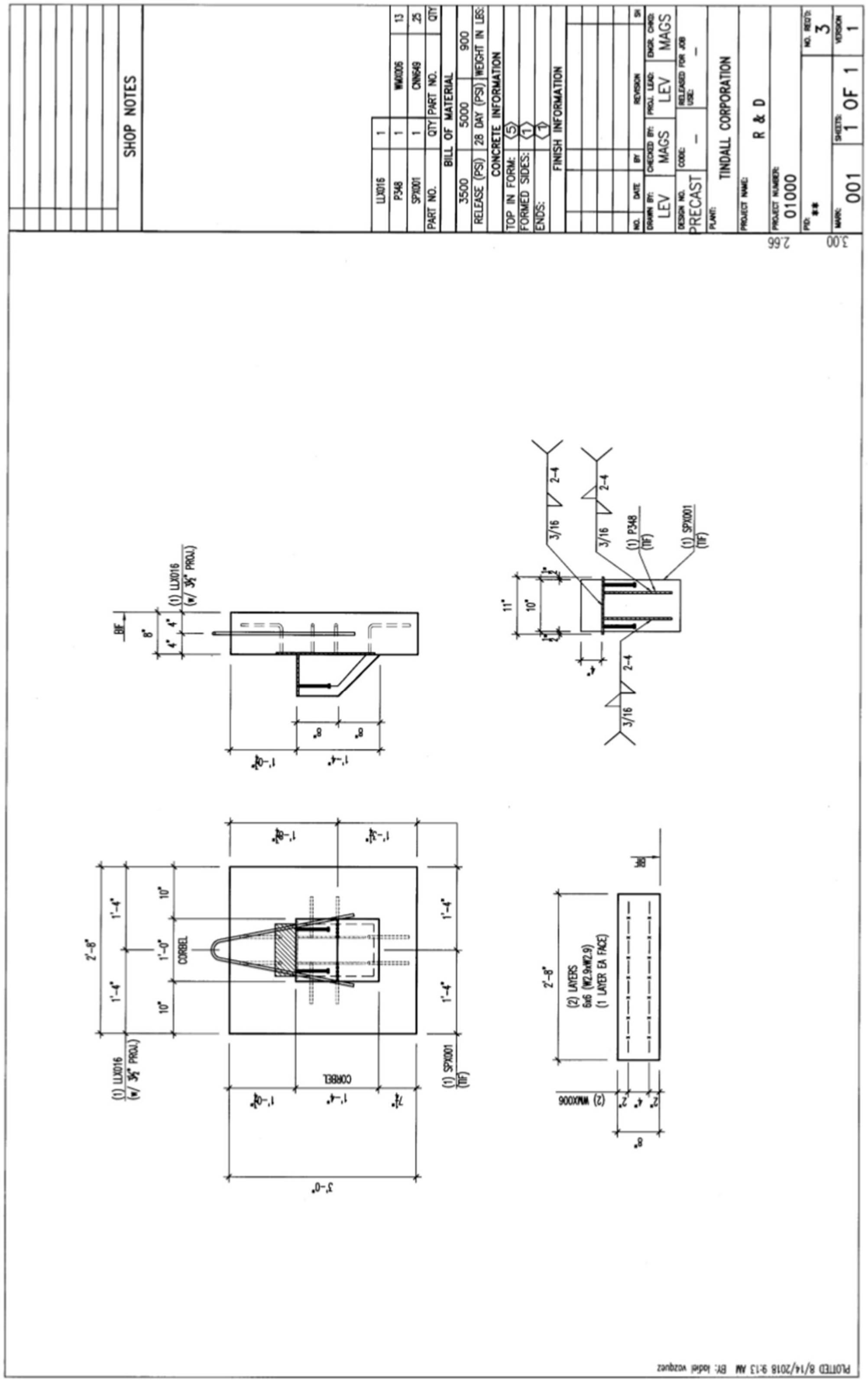

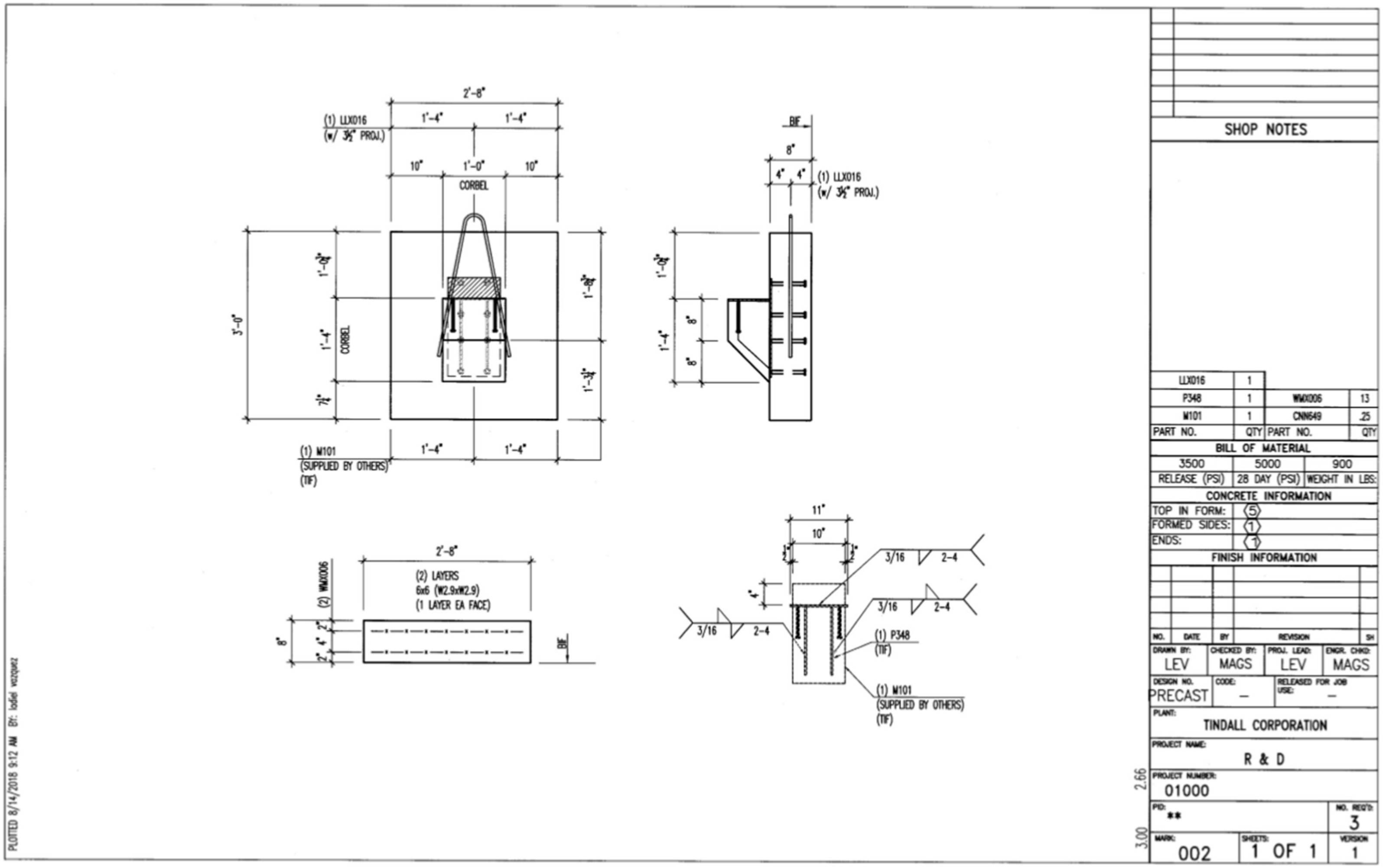
SHOP NOTES
LLX016 1
P348 1
M101 1
WWX006 13
CNN649 .25
PART NO. QTY PART NO. QTY
BILL OF MATERIAL
3500 5000 900
RELEASE (PSI) 28 DAY (PSI) WEIGHT IN LBS:
CONCRETE INFORMATION
TOP IN FORM: 5
FORMED SIDES: 1
ENDS: 1
FINISH INFORMATION
NO. DATE BY REVISION SH
DRAWN BY: LEV
CHECKED BY: MAGS
PROJ. LEAD: LEV
ENGR. CHKD: MAGS
DESIGN NO. PRECAST
CODE: –
RELEASED FOR JOB USE: –
PLANT: TINDALL CORPORATION
PROJECT NAME: R & D
PROJECT NUMBER: 01000
PID: **
NO. REQ'D: 3
MARK: 002
SHEETS: 1 OF 1
VERSION 1
2.66
3.00
(1) LLX016 (w/ 3½" PROJ.)
(1) M101 (SUPPLIED BY OTHERS) (TIF)
(1) P348 (TIF)
CORBEL
(2) LAYERS 6x6 (W2.9xW2.9) (1 LAYER EA FACE)
(2) WWX006
BIF
3/16 2-4
2'-8"
1'-4"
1'-0"
10"
3'-0"
11"
8"
4"
2"
PLOTTED 8/14/2018 9:12 AM BY: Isdiel vazquez

METROMONT	2802 WHITE HORSE ROAD GREENVILLE, SOUTH CAROLINA 29611 (864) 605-5000	PROJECT				JOB NO.
		DATE	DWN. BY	DATE	CHK. BY	SHEET

24" DEEP CORBEL ADD-ON EMBED

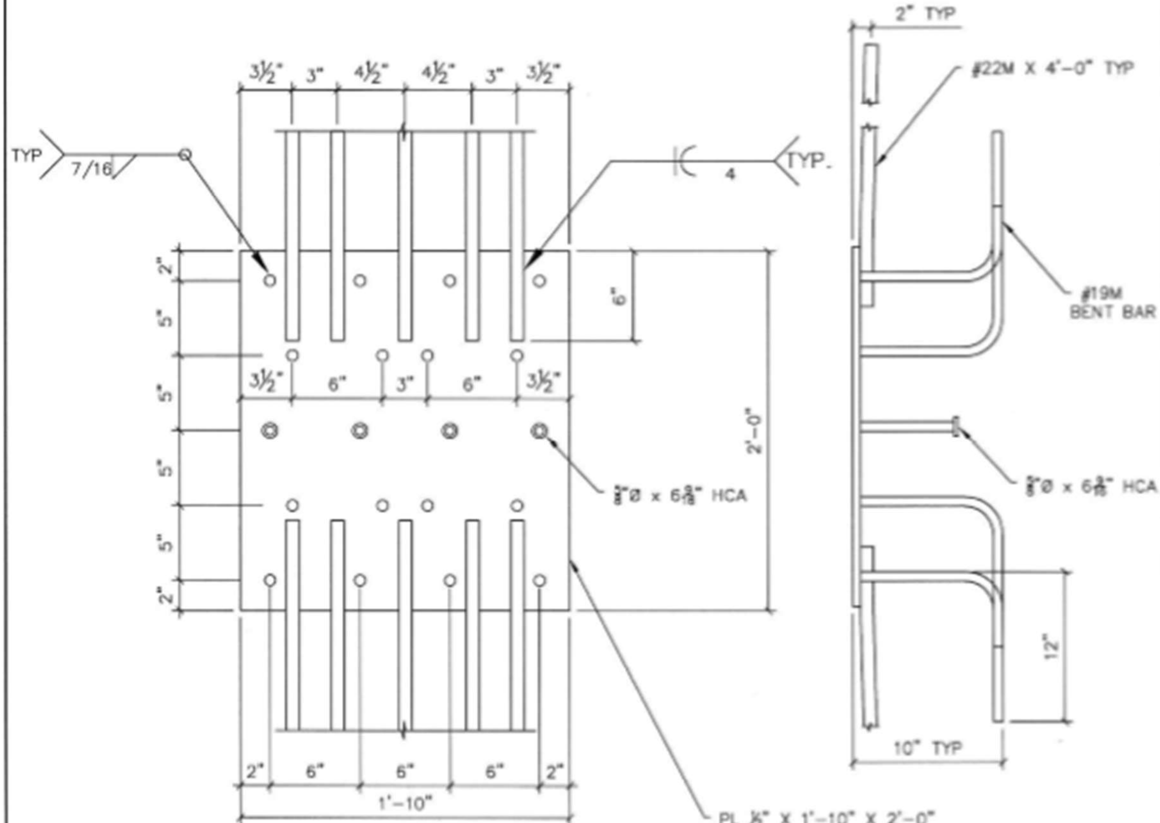

METROMONT™	PROJECT				JOB NO.
	DATE	DWN. BY	DATE	CHK. BY	SHEET

SW DESIGN

ADD-ON CORBEL DESIGN

WORST CASE SW @ B/4

DT DL = (75psf + 5psf)(60.33ft)(48.5ft/2) = 117.04^{k}

TG DL = .883^{k}/ft (48ft/2) = 21.2^{k}

LL = 40psf (60.33ft)(48.5ft/2) = 58.52^{k}

SN = 13.4psf (60.33ft)(48.5ft/2) = 19.6^{k}

V_u = 1.2(117.04^{k} + 21.2^{k}) + 1.6(58.52^{k}) + .5(19.6^{k}) = 269.32^{k}

N_u = .2(1.2(117.04^{k} + 21.2^{k})) + 269.32^{k}(6in)/18in = 122.95^{k}

CHECK EMBED PLATE

ASSUME TAIL BARS + BOT. (8) #19M TAKE FULL V_u

ϕV_n = .9(60ksi)(5 × .6in^2) + .75(60ksi)(8 × .44in^2)(.7) = 272.88^{k}

∴ TOP (8) #19M TAKE T_u + INTERACTION NOT REQD

ϕT_n = .9(60ksi)(8 × .44in^2) = 190.08^{k}

CHECK GUSSETS

USE (4) 1" THK GUSSETS

ϕV_n = .75(1.8)(36ksi)/[(1/(4in)(6in)) + ((6in − 3in)(3in)/(4in(6in)^3/12))]

ϕV_n = 48.6/(.04167 + 9/72)

ϕV_n = 291.5^{k}

CHECK WELD

SINCE GUSSETS/BRG PL SYMMETRICAL, CHECK

FOR 1/2 THE WELD ∴ 1/2 THE LOAD

SINCE SPREAD SHEET ACCOUNTS FOR ECC LOADING,

USE N_u = .2DL = .2(1.2(117.04^{k} + 21.2^{k})) = 33.18^{k}/2 = 16.59^{k}

USE 5/8" WELD ✓

WELD GROUP ANALYSIS

Using the Elastic Method for up to 24 Total Welds

Job Name:		Subject:	Bearing Seat Weld
Job Number:		Originator:	Checker:

Input Data:

Number of Welds, Nw = 18

Weld Coordinates:

	Start X1 (in.)	Start Y1 (in.)	End X2 (in.)	End Y2 (in.)
Weld #1	1.000	20.000	5.000	20.000
Weld #2	7.000	20.000	11.000	20.000
Weld #3	3.500	2.000	3.500	4.000
Weld #4	3.500	6.000	3.500	8.000
Weld #5	3.500	10.000	3.500	12.000
Weld #6	3.500	14.000	3.500	16.000
Weld #7	4.500	4.000	4.500	6.000
Weld #8	4.500	8.000	4.500	10.000
Weld #9	4.500	12.000	4.500	14.000
Weld #10	4.500	16.000	4.500	18.000
Weld #11	8.500	2.000	8.500	4.000
Weld #12	8.500	6.000	8.500	8.000
Weld #13	8.500	10.000	8.500	12.000
Weld #14	8.500	14.000	8.500	16.000
Weld #15	9.500	4.000	9.500	6.000
Weld #16	9.500	8.000	9.500	10.000
Weld #17	9.500	12.000	9.500	14.000
Weld #18	9.500	16.000	9.500	18.000

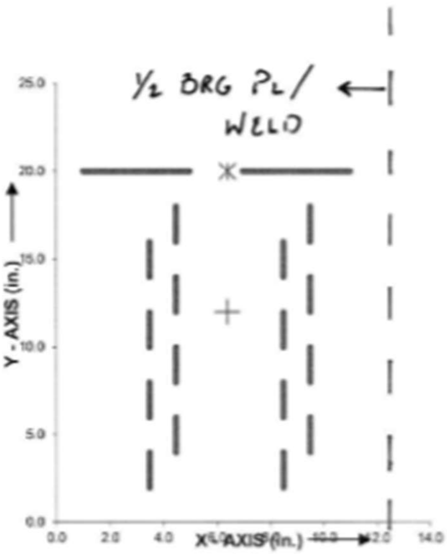

WELD GROUP PLOT

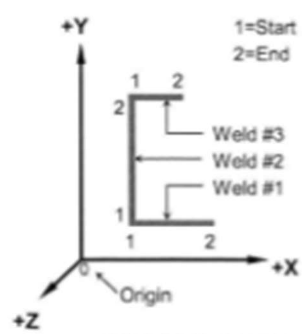

NOMENCLATURE

No. of Load Points = 1

Load Point Data:

	Point #1			
X-Coordinate (in.) =	6.421			
Y-Coordinate (in.) =	20.000			
Z-Coordinate (in.) =	6.000			
Axial Load, Pz (k) =	16.59	1/2 LOAD		
Shear Load, Px (k) =	0.00			
Shear Load, Py (k) =	-134.66			
Moment, Mx (in-k) =	0.00			
Moment, My (in-k) =	0.00			
Moment, Mz (in-k) =	0.00			

(continued)

Results:

Weld Group Properties:

Lw =	40.000	in.
Xc =	6.400	in.
Yc =	12.000	in.
Ix =	1322.67	in^3
Iy =	292.27	in^3
J =	1614.93	in^3

Σ Loads @ C.G. of Weld Group:

Σ Pz =	16.59	kips
Σ Px =	0.00	kips
Σ Py =	-134.66	kips
Σ Mx =	940.68	in-k
Σ My =	-0.35	in-k
Σ Mz =	-2.83	in-k

	Weld Forces (k/in.)	
	Fw(1)	Fw(2)
Weld #1	6.961	6.968
Weld #2	6.972	6.980
Weld #3	7.497	6.258
Weld #4	5.115	4.150
Weld #5	3.510	3.386
Weld #6	3.829	4.680
Weld #7	6.258	5.116
Weld #8	4.151	3.512
Weld #9	3.388	3.831
Weld #10	4.682	5.763
Weld #11	7.495	6.257
Weld #12	5.117	4.153
Weld #13	3.517	3.396
Weld #14	3.840	4.690
Weld #15	6.257	5.117
Weld #16	4.154	3.518
Weld #17	3.398	3.842
Weld #18	4.692	5.773

Required E70XX Weld Size:

Fw(max) =	7.497	kips/in.
Fillet (leg) =	0.337	in.

∴ Use 3/8"